

2015

A bypass transition model based on the intermittency function

Xuan Ge
Iowa State University

Follow this and additional works at: <https://lib.dr.iastate.edu/etd>

 Part of the [Aerospace Engineering Commons](#)

Recommended Citation

Ge, Xuan, "A bypass transition model based on the intermittency function" (2015). *Graduate Theses and Dissertations*. 14839.
<https://lib.dr.iastate.edu/etd/14839>

This Dissertation is brought to you for free and open access by the Iowa State University Capstones, Theses and Dissertations at Iowa State University Digital Repository. It has been accepted for inclusion in Graduate Theses and Dissertations by an authorized administrator of Iowa State University Digital Repository. For more information, please contact digirep@iastate.edu.

A bypass transition model based on the intermittency function

by

Xuan Ge

A dissertation submitted to the graduate faculty
in partial fulfillment of the requirements for the degree of
DOCTOR OF PHILOSOPHY

Major: Aerospace Engineering

Program of Study Committee:

Paul Durbin, Major Professor

Alric Rothmayer

Anupam Sharma

Wei Hong

Shankar Subramaniam

Iowa State University

Ames, Iowa

2015

Copyright © Xuan Ge, 2015. All rights reserved.

DEDICATION

I would like to dedicate this thesis to my wife Xue and to my parents without whose support I would not have been able to complete this work. I would also like to thank my friends and family for their loving guidance and assistance during the writing of this work.

TABLE OF CONTENTS

LIST OF TABLES	vi
LIST OF FIGURES	vii
ACKNOWLEDGEMENTS	xiii
ABSTRACT	xiv
CHAPTER 1. OVERVIEW	1
1.1 Motivation of the Work	1
1.2 Introduction of the Work	2
CHAPTER 2. REVIEW OF LITERATURE	3
2.1 Introduction	3
2.2 Modes of Transition	3
2.2.1 Orderly Transition	3
2.2.2 Bypass Transition	5
2.2.3 Separation Induced Transition	7
2.2.4 Wake Induced Transition	9
2.2.5 Roughness Induced Transition	12
2.3 Transition Modeling	13
2.3.1 Turbulence Models	14
2.3.2 Data Correlation Based Models	14
2.3.3 Transport Equation Based Models	16
2.3.4 Transition Modeling for Rough Wall Cases	21

CHAPTER 3. DEVELOPMENT OF THE MODEL	24
3.1 Introduction	24
3.2 Rational of the Current Model	24
3.3 Modeling for Smooth Wall Cases	25
3.3.1 Diffusion Term	26
3.3.2 Source Term	28
3.3.3 Sink Term	32
3.3.4 Separation Modification	34
3.3.5 Revision of the $k - \omega$ Model	39
3.4 Modeling for Rough Wall Cases	40
3.4.1 Prediction for Fully Turbulent Boundary Layers on Rough Walls	40
3.4.2 Modification on the Effective Wall Origin	44
3.4.3 Modification for Strong Acceleration Flows	49
CHAPTER 4. COMPUTATION	53
4.1 Introduction	53
4.2 Smooth Wall Cases	53
4.2.1 Flat Plate Cases	53
4.2.2 A Flat Plate Separated Flow	63
4.2.3 A Compressor Blade Cascade	67
4.2.4 Periodic Wakes Impinging on a Flat Plate	72
4.3 Rough Wall Cases	79
4.3.1 Flat Plate Cases	79
4.3.2 A High Pressure Turbine Blade Cascade	85
4.3.3 A Low Pressure Turbine Blade Cascade	90
CHAPTER 5. SUMMARY	93
5.1 Conclusion	93
5.2 Suggestions for Future Work	94

APPENDIX . FULL MODEL FORMULATION	95
1 Model for Smooth Walls	95
2 Model for Rough Walls	97
BIBLIOGRAPHY	98

LIST OF TABLES

Table 4.2.1	Summary of inlet conditions for flat plate cases.	55
Table 4.2.2	Summary of inlet conditions for the flat plate separated flow case.	64
Table 4.2.3	Summary of inlet conditions for the compressor blade cascade case.	67
Table 4.3.1	Summary of roughness heights and transition locations (T3A: $Tu_{in} = 1.5\%$).	85
Table 4.3.2	Summary of inlet conditions for the Stripf's HPT blade case.	86
Table 4.3.3	Summary of roughness heights for the Stripf's HPT blade, TC2.	89
Table 4.3.4	Summary of roughness heights for the Stripf's HPT blade, TC4.	89
Table 4.3.5	Summary of inlet conditions for the Stripf's LPT blade case.	91
Table 4.3.6	Summary of roughness heights for the Stripf's LPT blade, TC6.	91

LIST OF FIGURES

Figure 2.2.1 Schematic of spatial evolution of the natural transition. From Schlichting (1979)	4
Figure 2.2.2 Schematic of the Klebanoff modes.	6
Figure 2.2.3 Schematic of a separation bubble. From Malkiel and Mayle (1996) . . .	8
Figure 2.2.4 Schematic of rotor-stator wake interaction. From Wu et al. (1999) . <i>U_{rotor}</i> : rotor velocity in the stator reference frame; <i>U_{out}</i> : rotor exit flow velocity in the rotor reference frame; <i>U_{ref}</i> : stator inflow velocity in the stator reference frame.	10
Figure 2.2.5 Fluctuation velocity field, with successive instants from top to bottom. This figure shows the development of a backward jet in the relative velocity field and its breakdown to turbulence. From Durbin et al. (2002)	11
Figure 2.2.6 Experimental data for heat transfer coefficients versus the surface dis- tance. Figure reproduced from Boyle and Stripf (2009) , and data origi- nally from the test of Stripf et al. (2005)	13
Figure 3.3.1 Sensitivity of σ_γ to the transition location. $\sigma_\gamma = 0.2$ (solid), $\sigma_\gamma = 0.02$ (dash), $\sigma_\gamma = 0.1$ (dash-dot), $\sigma_\gamma = 0.4$ (dash-dotdot), $\sigma_\gamma = 0.8$ (long- dash).	27
Figure 3.3.2 Sensitivity of σ_l to the transition location. $\sigma_l = 5.0$ (solid), $\sigma_l = 10.0$ (dash), $\sigma_l = 2.5$ (dash-dot).	27
Figure 3.3.3 Contours of γ for the T3A case, with different values of ν and ν_T in the diffusion term. The black lines represent the profiles of the δ_{99} boundary layers.	28

Figure 3.3.4	Contours of the source term for the T3A case. The black line represents the profile of the δ_{99} boundary layer.	29
Figure 3.3.5	$R_{\nu bound}$ is equal to 100/0.5 (dash); 100/0.7 (solid); 100/0.9 (dash-dot).	31
Figure 3.3.6	Skin friction coefficient vs. Re_x in a flat plate test case (T3A); the solid curve represents the result based on the model without sink term. The other three represent the experimental data (square), theoretical laminar (dash) solution, and semi-empirical turbulent solution (dash-dot) respectively.	32
Figure 3.3.7	Contours of the sink term for the T3A case. The black line represents the profile of the δ_{99} boundary layer.	33
Figure 3.3.8	$R_{\nu bound}$ is equal to 18 (solid); 22 (dash); 26 (dash-dot). From 18 to 22, the difference is tiny; but from 22 to 26, C_f curve suddenly becomes fully turbulent.	34
Figure 3.3.9	The blue curve evaluates yU''/U' for Falkner-Skan boundary layer profiles. The pressure gradient parameter $\beta=-0.1988$ is just before separation. x-axis: vertical coordinate to the wall; y-axis: velocity and functions of its derivative.	36
Figure 3.3.10	Comparison of a velocity profile in a separated region and related derivatives. U , U' and $ U' $, U'' , and $ U'' $ are plotted from left to right. The velocity profile was extracted within the separated region from LES data by Lardeau et al. (2012) . $ U'' $ (i.e. $\nabla S $), rather than U'' is actually used to define the parameter R_s in Equation (3.3.10).	36
Figure 3.3.11	Linear ramps for F_{R_ν} . $R_{\nu bound} = 200$ (solid); $R_{\nu bound} = 100$ (dash) and too early reattachment is seen; $R_{\nu bound} = 300$ (dash-dot) and no reattachment is seen.	37
Figure 3.3.12	Linear ramps for F_{R_s} . $R_{sl bound} = -2$ (solid); $R_{sl bound} = -4$ (dash) and too early reattachment is seen; $R_{sl bound} = 0$ (dash-dot) and no reattachment is seen.	38

Figure 3.3.13	Distribution of γ_{eff} and line contours of U_x around the separation bubble for the flat plate separation test case.	38
Figure 3.4.1	Validation for the implementation of the Knopp's rough wall boundary conditions applied to the standard $k - \omega$ turbulence model. The near wall grid resolution is $y^+(1) \approx 0.3$. Test case by Ligrani and Moffat (1986)	45
Figure 3.4.2	Effects of C_r . This test case is a flat plate case with inflow turbulence intensity $Tu = 1.5\%$. The roughness height $r = 10 \times 10^{-4}m$ is set unchanged for different C_r s.	46
Figure 3.4.3	The effect of R_{c2} . This test case is the same as Figure 3.4.2.	47
Figure 3.4.4	The effects of coefficients in R_{c2} . This test case is the same as Figure 3.4.2.	48
Figure 3.4.5	The effect of the modified F_{turb} . This test case uses the Stripf's turbine, with inflow chord Reynolds number $Re_c = 1.4 \times 10^5$, turbulence intensity at the mid-pitch of the leading edge location $Tu_{l.e.} = 2.7\%$, and roughness height $r = 1.47 \times 10^{-4}m$	50
Figure 3.4.6	Contours of quantity $F_Q^{1.5}/350$. This test case is the same as Figure 3.4.5.	51
Figure 3.4.7	Effects of the multiplicative coefficient in R_{c3} . This test case uses the Stripf's turbine, with inflow chord Reynolds number $Re_c = 2.5 \times 10^5$, turbulence intensity at the mid-pitch of the leading edge location $Tu_{l.e.} = 1.6\%$, and roughness height $r = 0.73 \times 10^{-4}m$	52
Figure 4.2.1	Mesh used to compute T3A and T3B cases showing every other line in x and y.	54
Figure 4.2.2	Mesh used to compute T3C series cases showing every other line in x and y.	55
Figure 4.2.3	Free-stream velocity and turbulence intensity in T3A and T3B cases. Experiment data (symbols), simulation results (lines).	56

Figure 4.2.4	Normalized free-stream velocity in T3C cases. Experiment data (symbols), simulation results (lines). The circle symbol and long-dash line refer to case T3C4, and the other T3C cases collapse together.	56
Figure 4.2.5	Free-stream turbulence intensity in T3C cases. Experiment data (symbols), simulation results (lines).	57
Figure 4.2.6	Sensitivity to inlet k and ω (test case: T3A).	59
Figure 4.2.7	Contours of intermittency function and turbulence intensity for T3A and T3B.	60
Figure 4.2.8	Skin friction for T3A and T3B. Experimental (symbols), laminar (dash), turbulent (dash-dot), simulation (solid).	61
Figure 4.2.9	Skin friction for T3C cases. Experiment data (symbols), simulation results (lines).	62
Figure 4.2.10	Mesh for flat plate separated flow case showing every other line in x and y.	63
Figure 4.2.11	Distributions of free-stream turbulence intensity for the flat plate separated flow case. “Simulation 1” (\square), “Simulation 2” (+); current model (solid), LES by Lardeau et al. (2012) (dash).	64
Figure 4.2.12	Plots for Simulation 1. Current model (solid), LES by Lardeau et al. (2012) (dash), $k - \omega$ model (dash-dot).	65
Figure 4.2.13	Contours of stream-wise velocity around the separation bubble for Simulation 1.	65
Figure 4.2.14	Skin friction for Simulation 2. Current model (solid), LES by Lardeau et al. (2012) (dash).	66
Figure 4.2.15	Mesh for compressor blade cascade case showing every third line in x and y.	67
Figure 4.2.16	Contours of turbulence intensity for both simulations.	68
Figure 4.2.17	Pressure coefficient of the compressor blade case. Current model (solid), DNS (dash-dot for Simulation 1, dash-dot-dot for simulation 2).	69

Figure 4.2.18 Skin friction of the compressor blade case. Current model (solid), $k - \omega$ RANS model (dash), DNS (dash-dot for Simulation 1, dash-dot-dot for simulation 2).	70
Figure 4.2.19 Contours of γ and separation bubbles of the compressor blade cases.	71
Figure 4.2.20 The upper: schematic of the experiments of Liu and Rodi (1991) ; the lower: schematic of the simulation of Wu and Durbin (2000)	73
Figure 4.2.21 Dimensionless profiles of the wake at $x = -0.05$ (left column) and $x = 0.1$ (right column), where the wake halfwidth $b = 0.03$ and 0.1 , and deficit velocity $U_{def} = 0.48$ and 0.14 , respectively. The data from Wu and Durbin (2000) are denoted by dash lines and used for generation of their inlet profiles.	74
Figure 4.2.22 Comparison of contours of streamwise velocity between the DNS and present simulation.	76
Figure 4.2.23 Time-averaged mean C_f curves. Symbols: DNS of Wu et al. (1999) ; lines: present model.	77
Figure 4.2.24 Phase-averaged mean C_f curves. Symbols: DNS of Wu et al. (1999) ; lines: present model.	77
Figure 4.2.25 X-phase diagram of the phase-averaged mean C_f . The contour levels are from 0.0015 to 0.0065 with an increment of 0.0005	78
Figure 4.3.1 Contribution of the smooth Leading edge. The smooth wall case (solid), the case with the rough wall boundary conditions and uniform roughness (dash), and the case with the rough wall boundary conditions and a smooth leading edge (dash-dot).	80
Figure 4.3.2 Near wall distributions of R_ν and γ compared between smooth and rough walls.	81
Figure 4.3.3 Profiles of U^+ and R_ν at $x = 0.3, 0.7, 1.0$ and 1.45 . Transition onset is around $x = 0.7$ for the rough wall case, and $x = 1.0$ for the smooth wall case.	82

Figure 4.3.4	Skin friction for flat plate cases with different roughness heights and different inflow turbulence intensities.	84
Figure 4.3.5	Mesh used to the HPT blade case showing every other line in tangential and normal wall directions.	85
Figure 4.3.6	Pressure distribution on the blade surface for $Re_c = 2.5 \times 10^5$. The circles represent the experimental data of Stripf (2007) at the mid-span of the blade surface. The solid line represents the simulation result. . .	87
Figure 4.3.7	Results for the Stripf's HPT blade case. The solid lines are the predicted curves for the Nusselt number by the current model, and the dash lines are the predicted curves for the heat transfer coefficient by the correlation-based model in Boyle and Stripf (2009)	88
Figure 4.3.8	Skin friction coefficient for the Stripf's HPT blade: Case TC2 and TC4.	89
Figure 4.3.9	Mesh used to the LPT blade case showing every other line in tangential and normal wall directions.	90
Figure 4.3.10	Nusselt number for the Stripf's LPT blade case. The solid lines are the predicted curves for the Nusselt number by the current model, and the symbols present the experimental data.	91
Figure 4.3.11	Skin friction coefficient for the Stripf's LPT blade: Case TC5 and TC6.	92

ACKNOWLEDGEMENTS

I would like to take this opportunity to express my thanks to those who helped me with various aspects of conducting research and the writing of this thesis. First and foremost, Dr. Paul Durbin for his guidance, patience and support throughout this research and the writing of this thesis. His insights, erudition, innovation, rigour and passion have often inspired and encouraged me for completing my graduate education. I would also like to thank my committee members for their efforts and contributions to this work: Dr. Alric Roghmayer, Dr. Anupam Sharma, Dr. Wei Hong and Dr. Shanker Subramaniam. I would additionally like to thank Dr. Sunil Arolla for his guidance throughout the initial stage of my graduate life.

This work was funded by NSF grant #CBET-1228195.

ABSTRACT

An intermittency model that is formulated in local variables is proposed for representing bypass transition in Reynolds-Averaged Navier-Stokes (RANS) computations. No external data correlation is used to fix transition. Transition is initiated by diffusion, and a source term carries it to completion. A sink term is created to predict the laminar region before transition and vanishes in the turbulent region. Both the source and sink are functions of a wall-distance Reynolds number and turbulence scales. A modification is introduced to predict transition in separated boundary layers. The transition model is incorporated with the $k - \omega$ RANS model. The model is validated with several test cases. Decent agreement with the available data is observed in a range of flows.

An extended model for roughness-induced transition is proposed based on this intermittency model. To predict roughness effects in the fully turbulent boundary layer, published boundary conditions for k and ω are used. They depend on the equivalent sand grain roughness height, and account for the effective displacement of wall distance origin. Similarly in our approach, wall distance in the transition model for smooth surfaces is modified by an effective origin, which depends on equivalent sand grain roughness. Flat plate test cases are computed to show that the proposed model is able to predict transition onset in agreement with a data correlation of transition location versus roughness height, Reynolds number, and inlet turbulence intensity. Experimental data for turbine cascades are compared to the predicted results to validate the proposed model.

Nomenclature

$\langle \tilde{u} \rangle$	phase-averaged streamwise velocity
δ_*	displacement boundary layer thickness
γ	intermittency function
γ_{eff}	effective intermittency function for separated flow modification
λ_θ	local pressure gradient parameter
ν	molecular viscosity
ν_T	eddy viscosity
ω	turbulence specific dissipation rate
Ω_{ij}	rate of rotation tensor, $i, j=1, 2$ and 3
θ	momentum thickness
\tilde{u}	instantaneous streamwise velocity
b	halfwidth of the wake
d	wall-normal distance
d^+	dimensionless wall-normal distance
K	acceleration parameter
k	turbulence kinetic energy
k_L	energy of laminar fluctuations

r	roughness height, or equivalent sand grain roughness height
r^+	dimensionless roughness height
R_t	turbulence Reynolds number
R_ν	vorticity Reynolds number or wall distance Reynolds number
R_{rms}	root mean square roughness height
$Re_{\theta t}$	momentum thickness Reynolds number at the transition onset location
S_k	skewness of roughness
S_{ij}	rate of strain tensor, $i, j=1, 2, \text{ and } 3$
Tu	free-stream turbulence intensity
U	the component of mean velocity in x direction
u	the component of fluctuation velocity in x direction
u_*	friction velocity
U_∞	mean free-stream velocity
U_{def}	deficit velocity of the wake
U_{ref}	reference velocity
v	the component of fluctuation velocity in y direction
w	the component of fluctuation velocity in z direction
$y(1)$	wall distance of the grid point next to the wall

CHAPTER 1. OVERVIEW

1.1 Motivation of the Work

While RANS models for a wide range of fully turbulent flows are available in general CFD codes, models for laminar-to-turbulent transition are far more limited. One of the difficulties is that transition takes place through different mechanisms in various engineering flows.

When free-stream turbulence level ($\sqrt{2k/3}/U_{ref}$) is about 1% or more (Langtry, 2006), the boundary layers proceed from laminar to fully turbulent without the occurrence of linear instability of the base state (Tollmien-Schlichting waves). This mode of transition is referred to as bypass transition. Turbulence diffuses into the laminar boundary layer, and generates disturbances known as Klebanoff modes. These grow in amplitude, and transition to turbulence occurs. (Zaki and Durbin, 2005; Durbin and Wu, 2007)

In addition to a continuously turbulent free-stream, one very important instance of bypass transition arises in turbomachinery, in which the boundary layer is subject to periodically passing turbulent wakes. This is referred to as wake induced transition.

Moreover, separation induced transition is another common mechanism, in which a laminar boundary layer separates under the influence of an adverse pressure gradient and transition occurs within the separated shear layer due to the inflection point instability.

It is well known that surface roughness can trip a boundary layer. Bypass transition is triggered by free-stream disturbances penetrating into the boundary layer and/or by surface roughness. Nevertheless, there are few data correlations or prediction methods for roughness induced transition. They are needed for many applications. For instance, to increase the efficiency of turbomachinery performance, designers must account for effects of surface roughness on both heat transfer and aerodynamic loss.

It is challenging to develop a model which is valid for all different mechanisms. For general use in CFD, the model must be formulated in local variables, eschewing dependency on the boundary layer thickness or free-stream turbulence.

1.2 Introduction of the Work

The objective of the present work is to develop a model that invokes an intermittency function to represent bypass transition based on the $k - \omega$ RANS turbulence model. Only one transport equation for intermittency γ is used in this new model. The γ equation is formulated in local variables with no reference to data correlation and is tensorally invariant. The current model addresses bypass transition both in attached and separated flow. Although separation induced transition proceeds by a different mechanism from attached flow transition, some measure has been taken to locate the separation and trigger transition at the proper location.

This bypass transition model for smooth walls is then extended to account for the effects of wall roughness. An effective displacement depending on the equivalent sand grain roughness height is imposed on the wall distance in the γ equation. Modifications are designed to predict the transition location moving upstream appropriately due to surface roughness. To correctly simulate the roughness effects on the skin friction and heat transfer coefficients in the fully turbulent regime, formula proposed by [Knopp et al. \(2009\)](#) are chosen as the boundary conditions for k and ω on rough walls.

A wide range of test cases are performed to validate the model, including flat plate cases, a diffuser with a separation bubble, a compressor blade cascade, a high pressure and a low pressure turbine blade cascade. Various flow conditions are employed, such as different Reynolds numbers, pressure gradients, free-stream turbulence intensities, periodic passing turbulent wakes, and surface roughness.

CHAPTER 2. REVIEW OF LITERATURE

2.1 Introduction

This chapter will cover a brief introduction on the categories of laminar-to-turbulent transition and the researches in the past of transition modeling through a literature view.

2.2 Modes of Transition

2.2.1 Orderly Transition

In early research on linear inviscid stability theory, a famous and useful general result is that the occurrence of an inflection point in the basic velocity profile is a necessary condition for instability. Later on, solutions to viscous instability problem (Orr-Sommerfeld problem) for Blasius's boundary layer were first solved by Tollmien and Schlichting theoretically. [Schubauer and Skramstad \(1947\)](#), by introducing controlled oscillations with a vibrating ribbon of desired frequencies and amplitudes, experimentally confirmed the theoretical results about the "nose" of the marginal curves (critical Reynolds number and wavenumber for the marginally stable mode) quite convincingly. [Klebanoff et al. \(1962\)](#) refined and developed the experiments and found that at first two-dimensional Tollmien-Schlichting (T-S) waves grow in amplitude downstream. But when they reach a certain critical amplitude (1% of the free-stream velocity), they become perturbed three-dimensionally. Secondary instability theory introduced by [Herbert \(1983\)](#) attributes the growth of these three-dimensional disturbances to subharmonic resonance in the new basic flow, which is composed of the primary laminar flow and the small amplitude T-S waves. The 3-D disturbances develop into Λ vortices, which lift up away from the wall. This is where nonlinear development takes over and the turbulent spots born. Initially, they are very sparse. Subsequently downstream, they grow in size, increase

in frequency and merge to form the fully turbulent boundary layer. This type of transition is referred to as natural transition, or orderly transition. It will naturally happen with very small free-stream turbulence of less than 1% intensity. Kleiser and Zang (1991) provided a review about the early simulations to predict the complete transition process numerically. Since the growth rate is so slow, transition to turbulence might not complete until a stream-wise distance is as large as 20 times farther downstream from the leading edge than the initial starting point of linear instability (Durbin et al., 2002). The schematic illustration for spatial evolution of the natural transition is shown in Figure 2.2.1.

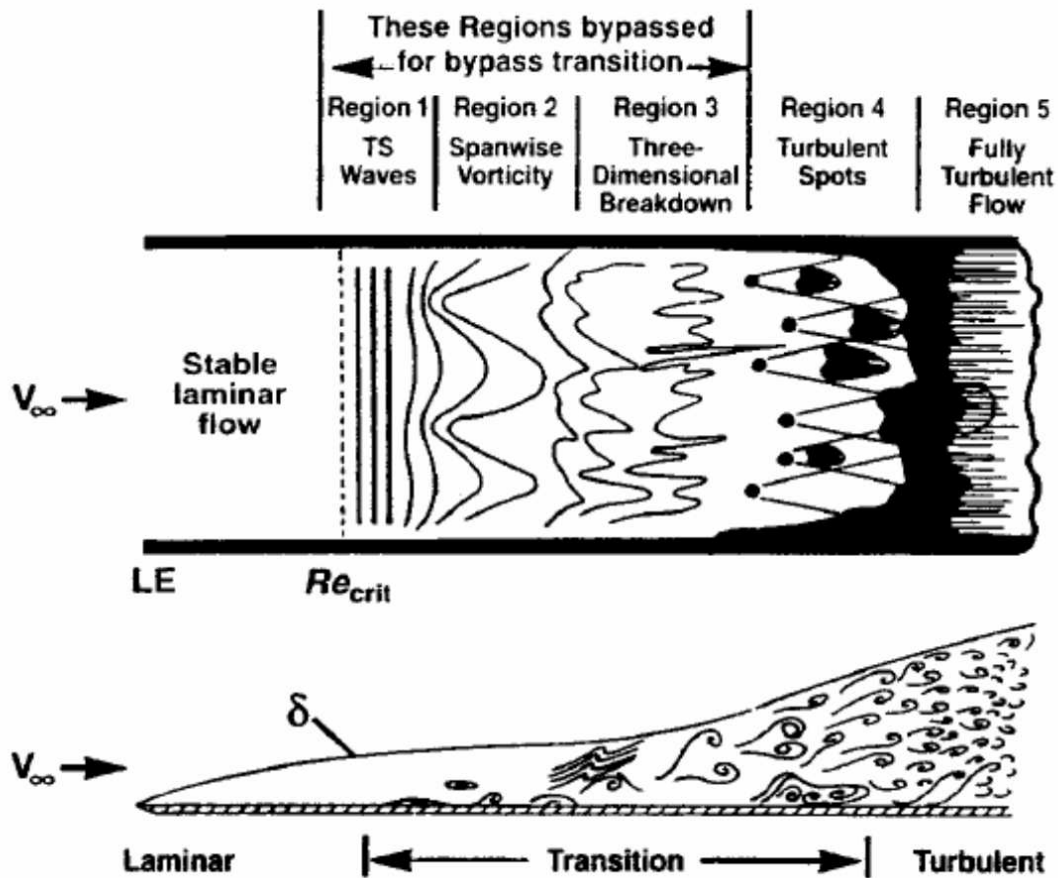
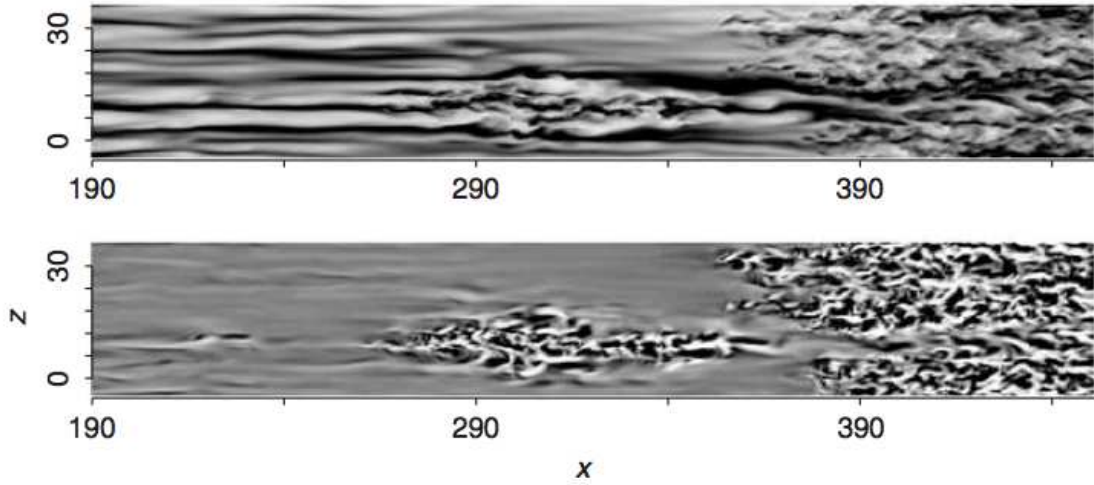


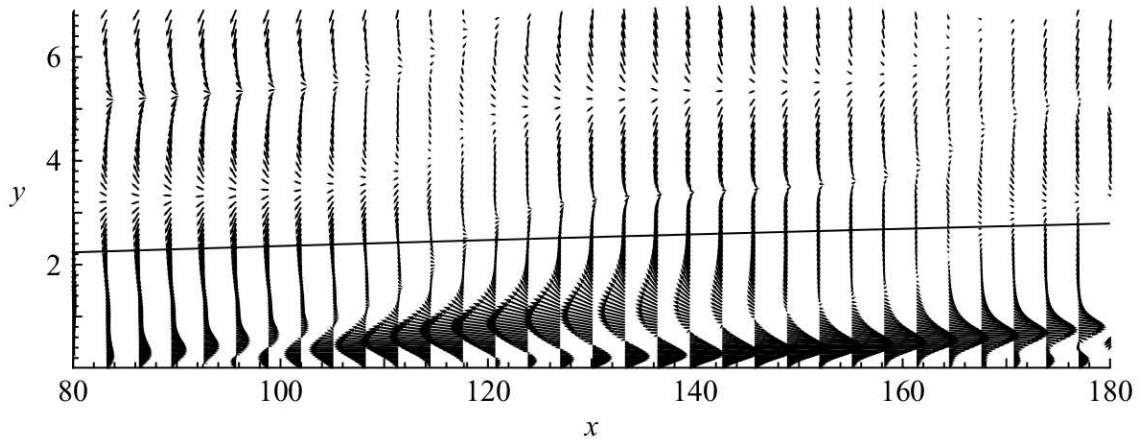
Figure 2.2.1 Schematic of spatial evolution of the natural transition. From Schlichting (1979).

2.2.2 Bypass Transition

Under realistic conditions, the processes of natural transition are either entirely absent or are difficult to identify within the transitional region of the flow. These instances of boundary layer breakdown have become broadly known as bypass transition. Under free-stream turbulence level of about 1.0% or more, boundary layers proceed from laminar to fully turbulent without the occurrence of 2-D T-S waves. Instead, transition is preceded by the formation of large-amplitude elongated disturbances, termed Klebanoff modes (Kendall, 1985). These elongated disturbances are created from isotropic free-stream turbulence. The dominant disturbances are the streamwise component u (10–20 % of the mean free-stream velocity) while the wall-normal and spanwise velocities of the perturbations remain the order of the free-stream turbulence intensity Tu (Liu et al., 2008). The perturbation is long in the sense that it takes the form of forward and backward jets, or streaks. Figure 2.2.2 is two plane views of the jets, with (a) observed in contours of the u (top) and v (bottom) component of perturbation velocity in $x - z$ plane and (b) depicted the disturbance vectors in $x - y$ plane. The direct numerical simulation (DNS) by Jacobs and Durbin (2001) captured the amplification of the streaks, their secondary instability due to high-frequency forcing from the turbulent free stream, and finally the inception of turbulent spots. Zaki and Durbin (2005) carried out DNS which found that the streaks appear owing to the penetration of only low frequency perturbation from the free stream into the boundary layer, and the transition is triggered by the high frequency non-penetrating disturbances interacting with the jet-like disturbances when they lift up to the upper bound of the shear layer. Therefore, the term bypass has become synonymous with transition due to free-stream vortical perturbations. Durbin and Wu (2007) provided a review for this type of transition including relevant concepts, theory and simulations.



(a) Contours of u (top) and v (bottom) in a plane near the wall under conditions of bypass transition. From [Durbin and Reif \(2011\)](#).



(b) Disturbance vectors in $x - y$ plane showing the jet-like modes. From [Liu et al. \(2008\)](#).

Figure 2.2.2 Schematic of the Klebanoff modes.

However, the term bypass does not preclude the presence of T-S waves entirely. When both boundary-layer streaks and T-S waves are present, their interaction can be stabilizing or destabilizing. For instance, both the secondary instability analysis and experiments ([Cossu and Brandt, 2004](#); [Fransson et al., 2005](#)) confirmed that steady streaks are stabilizing, reduce the growth rate of T-S waves and suppress transition, whereas some experiments

(Boiko et al., 1994) suggested that streaks enhance breakdown in natural transition. Liu et al. (2008) studied numerically the interaction between T-S waves and streaks, which shows that Λ vortices occur and breakdown, similar to the secondary instability of T-S waves. This intriguing result is explained as a competition between the reduction of growth rate of the primary T-S waves and the secondary instability of the T-S waves, both owing to the streaks. If the streaks prevent the T-S waves from increasing to the amplitude necessary to the secondary instability, transition will be suppressed, whereas if the T-S waves are sufficiently strong and overcome the negative effect of the streaks on their amplification, the streaks will enhance the breakdown via secondary instability.

Note that flow conditions, such as the mean pressure gradient (Abu-Ghannam and Shaw, 1980), the leading-edge shape (Kendall, 1991), etc. may cause different transition onset and length, even with seemingly the same free-stream turbulence level. Bypass transition can also happen due to surface roughness where the disturbances are activated from the perturbations at the wall instead of from the free-stream turbulence. This is also termed as roughness induced transition (discussed below in Section 2.2.5).

2.2.3 Separation Induced Transition

When a laminar boundary layer separates, transition may occur in the shear layer of the separated flow as a result of the inviscid instability mechanism. Due to the enhanced mixing caused by the turbulent flow, the shear layer may reattach. This reattachment forms a laminar-separation/turbulent-reattachment bubble on the surface. See Figure 2.2.3. The separation point is denoted as X_s . X_t and X_T represent the onset and ending points of transition respectively. X_R is the reattachment point.

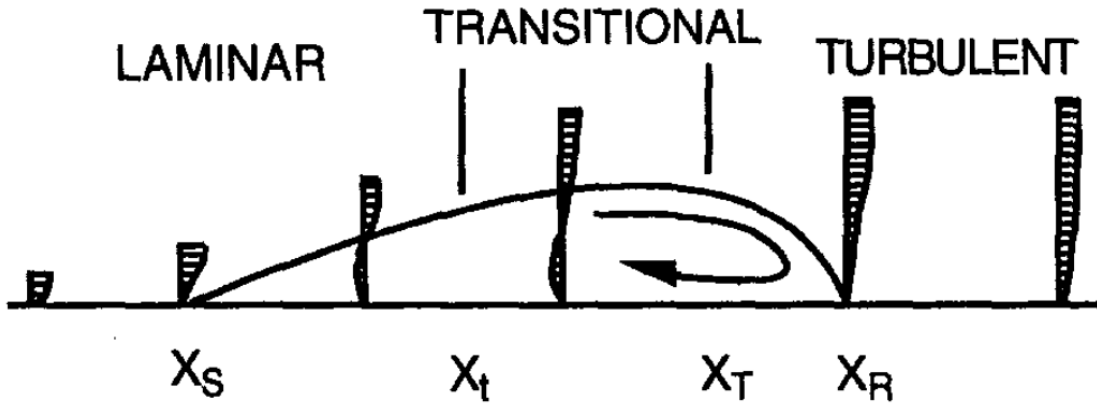


Figure 2.2.3 Schematic of a separation bubble. From [Malkiel and Mayle \(1996\)](#).

Separation bubbles have been classified as long or short based on their effect on the pressure distribution on an airfoil ([Mayle, 1991](#)). A small change in the Reynolds number or angle of attack can make a bubble change dramatically from short to long ([Mayle and Schulz, 1997](#)). If the bubble is very long and even fails to reattach, the separated flow will be so dominant that it will result in much more drag and a dramatic loss of lift and even cause the airfoil to stall. Since long bubbles produce large losses and large deviations in exit flow angles, they should be avoided. On the other hand, short bubbles are an effective way to force the flow turbulent and may be considered as a means to control performance. The present difficulty is in predicting whether the bubble will be long or short ([Mayle, 1991](#)).

In recent turbomachine designs, the suction side boundary layer over a blade is more subject to separation, particularly in the compressor stage ([Lardeau et al., 2012](#)). Understanding transition in separated region can therefore impact the design for improvement of the efficiency of the compressor performance. Experimental ([Lou and Hourmouziadis, 2000](#); [Volino and Hultgren, 2001](#)) and DNS ([Wissink and Rodi, 2006b](#); [Zaki and Durbin, 2006](#); [Zaki et al., 2010](#)) studies examined the response of transition and separation to the pressure gradient and free-stream turbulence intensity. Strong acceleration (i.e. favorable pressure gradient) prevents transition while adverse pressure gradient causes laminar separation and hence transition in the shear layers. With low free-stream turbulence, the dominant mechanism is associated with the inflection

point in the velocity profile in the early stage of separation, similar to the Kelvin-Helmholtz (K-H) instability in free-shear layers. In this case, transition occurs slowly, and the bubble is long and may involve all of the stages listed for orderly transition (Mayle, 1991). In other words, the T-S and K-H instability may coexist and interact with each other. With high free-stream turbulence, the jet-like streaks, or Klebanoff modes, may occur upstream of the separated flow. Fluctuations in streaks consequently give rise to a faster breakdown of the K-H spanwise oriented vortices downstream in the initial stage of the separated region. The energy carried by the Klebanoff modes increases with the free-stream turbulence intensity, and thus leads to a earlier transition and a greater reduction in the separation bubble length.

2.2.4 Wake Induced Transition

Upstream and downstream blade interactions in passages of multi-stage axial turbomachines result in a complex and inherently unsteady flow field. For instance, the boundary layer over a blade surface is subject to a substantial degree of unsteadiness that owes to impinging wakes of the upstream stator or rotor. The considerable effect of upstream wakes arises primarily because substantial regions of laminar and transitional flows exist on the suction surface of blades of intermediate stages. The impinging turbulent wake markedly alters the path to transition. Figure 2.2.4 illustrates this type of rotor-stator wake interaction. Rather than the bypass transition associated with continuous free-stream turbulence, this type of transition is referred to as wake induced transition.

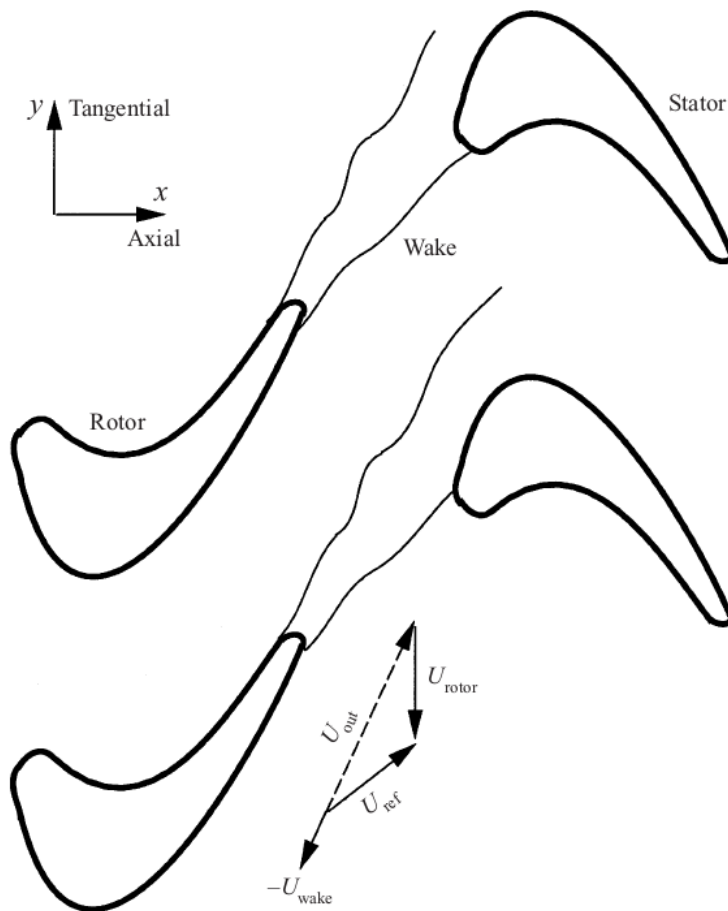


Figure 2.2.4 Schematic of rotor-stator wake interaction. From [Wu et al. \(1999\)](#). U_{rotor} : rotor velocity in the stator reference frame; U_{out} : rotor exit flow velocity in the rotor reference frame; U_{ref} : stator inflow velocity in the stator reference frame.

An idealized benchmark case to mimic wake induced transition in turbomachines would be flat plate boundary layer transition induced by periodically passing wakes, though the complexities of pressure gradients, surface curvature and leading edge are omitted. [Liu and Rodi \(1991\)](#) carried out this basic flat plate case experimentally, and DNS by [Wu et al. \(1999\)](#) following the experimental configuration obtained accurately statistical fields via averaging over samples both at constant phase and in the direction of homogeneity. Figure 2.2.5 depicts the relative velocity field gained by subtracting the phase averaged velocity from the instantaneous velocity. The three sections are three successive instants in time, with time increasing from top

to bottom and time interval of 0.1 of the wake passing period. A backward jet is regarded as the precursor to the turbulent spot (Durbin et al., 2002). In the top section, a certain free-stream eddy causes jetting motion near the wall. Then the K-H type instability that grows on the negative jet develops small-scale eddies that evolve into the turbulent spot. Wu and Durbin (2000) predicted the wake induced transition over flat plate by RANS method and achieved agreement with the DNS data in many crucial respects. DNSs of flow through passages of linear turbomachinery cascades are nowadays feasible at the range of transitional Reynolds numbers. Examples include Wissink and Rodi (2006a), Zaki et al. (2009) and Wissink et al. (2014).

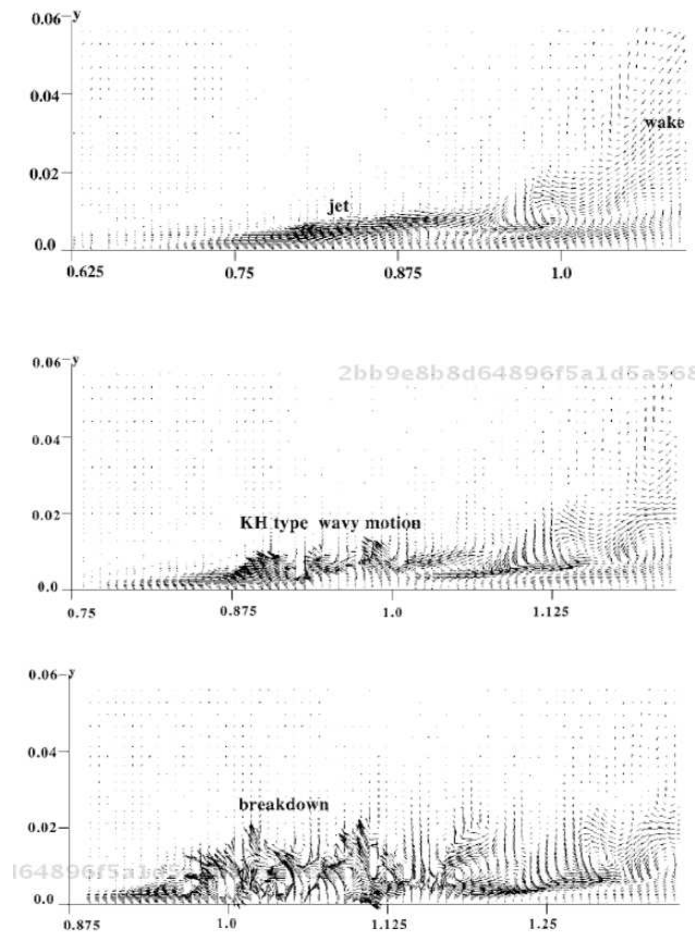


Figure 2.2.5 Fluctuation velocity field, with successive instants from top to bottom. This figure shows the development of a backward jet in the relative velocity field and its breakdown to turbulence. From Durbin et al. (2002).

2.2.5 Roughness Induced Transition

In reality, most of the blades in turbomachines quickly become roughened due to various damage mechanisms (Licari and Christensen, 2011), though they are initially hydrodynamically smooth. In general, surface roughness adversely affects turbomachinery performance by increasing external heat transfer and by increasing aerodynamic loss.

Arts et al. (1990) pointed out that a smooth vane can have transition occurring far downstream the leading edge on the suction side at moderate Reynolds numbers, even with high inflow turbulence intensities; but, as the roughness height increases, the transition onset gradually moves upstream to the leading edge. Figure 2.2.6 shows the measured heat transfer coefficients in the test of Stripf et al. (2005). Only at the highest roughness does the heat transfer appear to be fully turbulent over the entire surface. When the boundary layer becomes turbulent, heat transfer can increase by a factor of 10 (Stripf et al., 2009a). The change in blade surface heat transfer with transition is a very good indicator of transition onset and length. Arts (1995) showed that in the first turbine stage just the presence of film cooling holes on the blade surfaces causes transition to turbulence. Transition is typically not an issue for this stage due to film cooling. In later stages, where film cooling may not be used and Reynolds numbers are lower, heat transfer may remain a concern due to roughness induced transition if blades have only internal cooling. The optimization of cooling technologies requires the exact knowledge of the heat transfer distribution for rough surface transitional boundary layers.

Boyle and Stripf (2009) mentioned that surface roughness generally decreases aerodynamic efficiency of a turbine blade cascade according to relevant literature. But Boyle and Senyitko (2003) show that at low Reynolds numbers roughness improves aerodynamic efficiency, while at high Reynolds numbers roughness doubles vane loss. Therefore, to improve the efficiency at both low and high Reynolds numbers, exploring the effects of roughness on the boundary layer is necessary. A recent review of Bons (2010) also reported that a definite region of “roughness benefit” could be obtained if the roughness-induced transition could suppress the separation bubble at low Reynolds numbers within low pressure turbine stage. Rao et al. (2014) presented their work on the individual and coupled effects of the incoming free-stream turbulence and

surface roughness on the transition of a separated shear layer via large eddy simulation (LES). Note that there is a compromise between the positive effects of suppression of the bubble and the negative effects arising from the increasing loss in the reattached rough-surface turbulent boundary layer (Zhang, 2006).

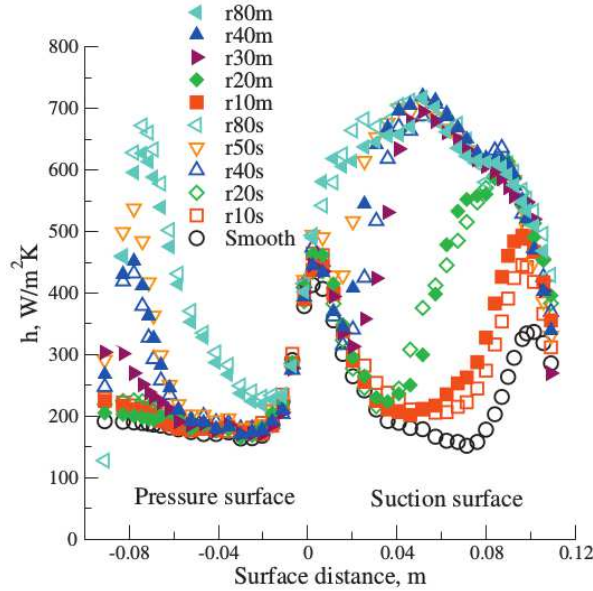


Figure 2.2.6 Experimental data for heat transfer coefficients versus the surface distance. Figure reproduced from Boyle and Stripf (2009), and data originally from the test of Stripf et al. (2005).

2.3 Transition Modeling

There are generally three approaches for transition modeling and prediction: rely on the closure model to transition from laminar to turbulent solutions; use a data correlation to decide when to switch from laminar to turbulent solutions; or devise additional model equations to represent transition. In the last approach, two branches have been explored: the first is to develop an equation for the energy of fluctuations that occur in the laminar region upstream of transition; the second is to develop an equation for the intermittency function, $\gamma(\mathbf{x}, t)$.

2.3.1 Turbulence Models

Most turbulence models are developed for fully turbulent flows and calibrated with turbulent data. However, most transport equation models do converge to a laminar solution at low Reynolds number and to a turbulent solution at sufficiently high Reynolds number. The model equations do evidence a transition between laminar and turbulent solution branches. Most eddy viscosity closure models predict early transition.

As turbine blades often operate at low enough Reynolds numbers to come across significant portions of laminar flow on their surfaces, their boundary layers are better described as buffeted laminar layers. But in such instances, the bulk of the flow may be turbulent and the overall flow calculation must be with a turbulence model. Therefore bypass transition, which is stochastic by nature, is dominant in such boundary layers. Turbulent spots are highly localized, irregular motions inside the boundary layer. So the turbulence models which describe statistical fluid dynamics are not entirely irrelevant; but neither are they entirely rational. Very often the models are solved without revision, depending on their capability of early transition prediction. But when accurate predictions of the laminar and transitional regions are required, the turbulence model must be modified by a method to predict transition.

2.3.2 Data Correlation Based Models

This approach requires a criterion that allows the determination of the position of transition onset, and switches from a laminar to a turbulent computation at this prescribed transition point. For a zero pressure gradient flow, the position of the transition onset has been correlated by [Mayle \(1991\)](#) as

$$Re_{\theta t} = 400Tu^{-0.625}, \quad (2.3.1)$$

where $Re_{\theta t}$ is the momentum thickness Reynolds number at the transition onset location. [Abu-Ghannam and Shaw \(1980\)](#) proposed a criterion for the transition location accounting for the pressure gradient, which reads

$$Re_{\theta t} = 163 + \exp \left[F(\lambda_{\theta}) - \frac{F(\lambda_{\theta})}{6.91} Tu \right], \quad (2.3.2)$$

where

$$\begin{aligned} F(\lambda_\theta) &= 6.91 + 12.75\lambda_\theta + 63.64\lambda_\theta^2 \quad \text{for } \lambda_\theta < 0 \\ F(\lambda_\theta) &= 6.91 + 2.48\lambda_\theta - 12.27\lambda_\theta^2 \quad \text{for } \lambda_\theta > 0, \end{aligned} \quad (2.3.3)$$

θ is the momentum thickness and $\lambda_\theta = \left(\frac{\theta^2}{\nu}\right) \left(\frac{\partial U_\infty}{\partial x}\right)$ is the local pressure gradient parameter. Tu is the free-stream turbulence intensity in percentage, $100\sqrt{2k/3}/U_\infty$, measured in the free stream. Transition occurs where the local momentum thickness Reynolds number exceeds the above critical value.

[Suzen et al. \(2000\)](#) proposed another correlation which provided slightly better approximation than the correlation of [Abu-Ghannam and Shaw \(1980\)](#) for favorable pressure gradients while maintaining the good features of Abu-Ghannam and Shaw in adverse pressure gradient region. The transition criterion was re-correlated to Tu and the acceleration parameter, K ,

$$Re_{\theta t} = (120 + 150Tu^{-2/3})\coth[4(0.3 - K \times 10^5)], \quad (2.3.4)$$

where $K = \left(\frac{\nu}{U_\infty^2}\right) \left(\frac{\partial U_\infty}{\partial x}\right)$.

Another approach is to modulate either the eddy viscosity or the production term in the k equation to increase it from zero to its full value across a transition zone. The basic idea is to introduce an intermittency function, γ , that increases from zero to unity, and to replace the eddy viscosity by $\gamma\nu_T$. If the transition has been predicted to occur at x_t by making use of a transition criterion like Equation (2.3.1), formulas like

$$\gamma = 1 - e^{-(x-x_t)^2/l_t^2}, \quad x \geq x_t, \quad (2.3.5)$$

have been used ([Dhawan and Narasimha, 1958](#)). γ is slowly ramped up from zero to unity until the fully turbulent boundary is achieved. Here l_t is a transition length ($l_t^2 = \nu^2/(\hat{n}\sigma U_\infty^2)$), which has been estimated to be about 126 times the momentum thickness ($l_t = 126\theta$) in zero pressure-gradient boundary layers. The parameter $\hat{n}\sigma$ relates to the propagation rate of turbulent spots in laminar boundary layer. There are many other algebraic models for intermittency and these are usually based on properties like turbulent spot production and propagation rate. Examples include [Gostelow et al. \(1994\)](#) and [Solomon et al. \(1996\)](#). [Steelant and Dick \(1996\)](#) provided the following correlations of $\hat{n}\sigma$ versus Tu and K ,

$$\hat{n}\sigma_{ZPG} = 1.25 \times 10^{-11} \times Tu^{7/4}, \quad (2.3.6)$$

$$\frac{\hat{n}\sigma}{\hat{n}\sigma_{ZPG}} = \begin{cases} (474Tu^{-2.9})^{1-\exp(2 \times 10^6 K)}, & K < 0, \\ 10^{-3227K^{0.5985}}, & K > 0. \end{cases} \quad (2.3.7)$$

where $\hat{n}\sigma_{ZPG}$ is for cases of zero pressure gradient.

2.3.3 Transport Equation Based Models

2.3.3.1 Laminar fluctuation model

As mentioned at the beginning of this section, this type of model is devised with a transport equation for the energy of fluctuations in the laminar boundary layer-the Klebanoff modes or instability waves-and has closer connection to the phenomenology of transition. These fluctuations grow and produce turbulent kinetic energy. The key elements of the equation for the energy of laminar (non-turbulent) fluctuations, k_L , are its production and transfer to turbulence.

Model equations proposed by [Mayle and Schulz \(1997\)](#), and subsequently [Lardeau et al. \(2004\)](#) and [Lardeau et al. \(2009\)](#), in a general form, are written as,

$$D_t k_L = P_L + \nabla \cdot \mathbf{T}_L - D_L - R, \quad (2.3.8)$$

where P_L is the production term and depends on the type of transition considered (bypass or separated-induced), the energy flux \mathbf{T}_L is assumed to be purely viscous, i.e. $\mathbf{T}_L = \nu \nabla k_L$, while the dissipation rate D_L is approximated analogous to that for turbulent flows, namely on dimensional grounds with the kinetic energy and wall-normal distance as the relevant scales, i.e. $D_L = 2\nu k_L/d^2$, where d is the distance from the wall. The right most term R represents breakdown of laminar fluctuations into turbulence, or the transfer of laminar kinetic energy to its turbulent counterpart. The same term, with positive sign, is added to the turbulent kinetic energy equation: $D_t k = P + R - \epsilon \dots$

[Mayle and Schulz \(1997\)](#) proposed a form of the source term

$$P_L = C_\omega \frac{U_\infty^2}{\nu} \sqrt{k_L k_\infty} \exp(-d^+/C_+),$$

based on the assumption that shear production is zero, and [Lardeau et al. \(2004\)](#) adopted this. U_∞ and k_∞ are the mean velocity and kinetic energy in the free stream respectively.

$d^+ = du_*/\nu$ is the dimensionless wall distance with $u_* = \sqrt{\nu\partial_n U|_w}$, being the skin friction. C_ω depends on the effective frequency and the turbulence level in free stream, and $C^+ = 13$. For separation-induced transition, [Lardeau et al. \(2009\)](#) adapted the production term compatible with the turbulent-flow form: $P_L = 2\nu_L |S|^2$. Here $|S|^2 = S_{ij}S_{ij}$ and S_{ij} is the rate of strain tensor.

The total kinetic energy proposed by [Lardeau et al. \(2004\)](#) is written as $k_{tol} = (1-\gamma)k_L + \gamma k$ and the eddy viscosity $\nu_T = f_\mu C_\mu \frac{k_{tol}(\gamma k)}{\epsilon}$. The damping function f_μ represents the influence of molecular viscosity on its turbulent counterpart. Here the intermittency function γ is used to damp the tendency of the turbulence model from inducing early transition by an excessive and rapidly build-up turbulence production. At this point, data correlation similar to Equation (2.3.5) was used for γ distribution, so was Equation (2.3.4) for γ switch-on. This is thereby not formulated locally.

[Walters and Cokljat \(2008\)](#) proposed the form

$$D_t k_L = 2\nu_{Tl}|S|^2 - R - D_L + \nabla \cdot (\nu \nabla k_L), \quad (2.3.9)$$

in which $2\nu_{Tl}|S|^2$ is the rate of production of laminar fluctuations. To accommodate both bypass and natural transition, ν_{Tl} has two components,

$$\nu_{Tl} = \nu_{BP} + \nu_{NT},$$

associated with large-scale eddies and with instability.

Initially, the large-scale eddies are contained in free-stream turbulence. Klebanoff modes are spawned by these large-length-scale motions. The model is motivated by this phenomenology.

[Walters and Cokljat \(2008\)](#) wrote

$$\nu_{BP} = 3.4 \times 10^{-6} f_{\tau l} \frac{\Omega \lambda_{eff}^2}{\nu} \sqrt{k_{Tl}} \lambda_{eff}, \quad (2.3.10)$$

with

$$\lambda_{eff} = \min[2.495d, \sqrt{k}/\omega]$$

providing the length scale; and

$$k_{Tl} = k \left[1 - \left(\frac{\lambda_{eff}}{L} \right)^{2/3} \right],$$

where $L = \sqrt{k}/\omega$, representing the large-scale component of the turbulent kinetic energy. The laminar fluctuation Equation (2.3.9) is conjoined with the k- ω model.

In Equation (2.3.10), Ω is the magnitude of the vorticity vector; and $f_{\tau l}$ is the damping function

$$f_{\tau l} = 1 - \exp \left[-4360 \frac{k_{Tl}}{2\lambda_{eff}^2 |S|^2} \right].$$

The numerical coefficients were adjusted to fit data. The component ν_{BP} becomes small where d is large and where d is small. This matches the exponential observation that Klebanoff modes develop in the central part of the boundary layer.

Natural transition is invoked by

$$\nu_{NT} = 10^{-10} \beta_L \frac{|\Omega| d^2}{\nu} |\Omega| d^2, \quad (2.3.11)$$

with

$$\beta_L = \begin{cases} 0, & R_\Omega < 1000, \\ 1 - e^{-(0.005 R_\Omega - 5)}, & R_\Omega > 1000, \end{cases}$$

where $R_\Omega = |\Omega| d^2 / \nu$, and $|\Omega| = \sqrt{2\Omega_{ij}\Omega_{ij}}$. This acts analogously to an instability criterion. In a Blasius boundary layer, $\max_y R_\Omega = 2.193 R_\theta$. Thus the instability criterion is $R_\theta > 456$ (which is higher than the value of 200 from linear stability theory).

Their R form is

$$R = 0.21 B_L \frac{k_L}{\tau_T},$$

where $\tau_T = \lambda_{eff} / \sqrt{k}$. As the turbulent energy grows, τ decreases, transferring energy from laminar fluctuations to turbulence. The coefficient B_L controls the onset of transition,

$$B_L = \begin{cases} 0, & R_k < 35, \\ 1 - e^{-(R_k - 35)/8}, & R_k > 35, \end{cases}$$

where $R_k = \sqrt{k}d/\nu$. The transition criterion is based on the Reynolds number R_k , which contains wall distance and turbulent kinetic energy. Thus breakdown initiates well above the wall, as occurs in experiments.

[Walters and Cokljat \(2008\)](#) also modified R for natural transition, and introduce other limiting and interpolation functions to improve agreement with data.

2.3.3.2 Intermittency transport equation

The data correlation function, Equation (2.3.5), of [Dhawan and Narasimha \(1958\)](#) proposed a prescribed intermittency distribution across the transition. But it was not clear in general how to predict the transition location, or how to adapt the function to general flows.

A relatively new approach to intermittency modeling is to propose a transport equation for the intermittency factor where the source terms are devised to mimic the behavior of some algebraic intermittency models, such as Equation (2.3.5). This equation can be derived into a transport equation. Note that for $x > x_t$.

$$\frac{d\gamma}{dx} = 2 \frac{x - x_t}{l_t^2} e^{-(x-x_t)^2/l_t^2} = 2 \frac{1-\gamma}{l_t} [-\log(1-\gamma)]^{1/2}.$$

If x is regarded as the stream-wise direction, this can be generalized to

$$\mathbf{u} \cdot \nabla \gamma = |\mathbf{u}| \frac{2(1-\gamma)}{l_t} [-\log(1-\gamma)]^{1/2}.$$

If γ is small $\sqrt{-\log(1-\gamma)} \approx \sqrt{\gamma}$. Adding a diffusion term provides a transport equation

$$D_t \gamma = 2(1-\gamma) \sqrt{\gamma} \frac{|\mathbf{u}|}{l_t} + \nabla \cdot [(\nu + \nu_T) \nabla \gamma], \quad (2.3.12)$$

where ν_T is the eddy viscosity. This is a starting point for more elaborate formulations. The main advantages of this approach is that it is possible to model the transition process not only in the flow direction but also across the boundary layer and thus provide a more realistic prediction of the transition. The transport equation controls the rise of γ from zero in laminar flow to unity in turbulent flow. The onset position of transition still has to be determined by a data correlation like Equation (2.3.2). The correlation involves the boundary layer momentum thickness and the free-stream turbulence. The former is an integral property and the latter a remote variable. This is unsuitable for unstructured-grid CFD codes. Otherwise in boundary layer codes or structured-grid CFD codes, this approach is feasible since the grid lines are aligned normal to the wall and the required variables can be obtained by searching in the grid j coordinate (i.e. in the wall normal direction by assuming the grid is strictly aligned with the wall).

[Steelant and Dick \(1996\)](#) proposed a transport equation for intermittency, in which the source term of the equation was developed such that the γ distribution of [Dhawan and Narasimha](#)

(1958) can be reproduced. But it was restricted to the boundary layer computations. A data correlation for transition onset was used. [Suzen and Huang \(2000\)](#) proposed an extended version of the model of [Steelant and Dick \(1996\)](#) and produced a realistic variation of γ in the cross-stream direction, still requiring a data correlation. [Suzen et al. \(2003\)](#) involved a correlation for $Re_{\theta t}$ in separated flows, again not in terms of local parameters. This is unsuitable for general use in CFD.

To implement such equation in unstructured-grid CFD codes for more general engineering circumstances, some models which are formulated in only local variables are developed ([Menter et al., 2006a,b](#); [Langtry and Menter, 2009](#)). In their method, the data correlation is replaced by a transport Equation (2.3.13) for transition Reynolds number. The intermittency function solves a second transport equation (2.3.14).

$$D_t \widetilde{Re_{\theta t}} = P_{\theta t} + \nabla \cdot [2.0(\nu + \nu_T) \nabla \widetilde{Re_{\theta t}}], \quad (2.3.13)$$

where the source term $P_{\theta t} = 0.03 \frac{\rho U^2}{500\nu} (Re_{\theta t} - \widetilde{Re_{\theta t}})(1.0 - F_{\theta t})$, and $F_{\theta t}$ is a blending function, which is equal to zero in the free-stream and one in the boundary layer.

$$D_t \gamma = P_\gamma - E_\gamma + \nabla \cdot [(\nu + \nu_T) \nabla \gamma]. \quad (2.3.14)$$

The source term P_γ and sink term E_γ are defined as follows,

$$P_\gamma = 2.0|S|(1 - \gamma)(\gamma F_{onset})^{0.5} F_{length}, \quad (2.3.15)$$

$$E_\gamma = 0.06|\Omega|\gamma(50\gamma - 1)F_{turb}, \quad (2.3.16)$$

Here $|S| = \sqrt{2S_{ij}S_{ij}}$, and $|\Omega| = \sqrt{2\Omega_{ij}\Omega_{ij}}$. F_{length} is an empirical correlation that controls the length of transition, and F_{onset} controls the transition onset location. The form of F_{onset} is as follows,

$$\begin{aligned} F_{onset1} &= \frac{Re_\nu}{2.193 \cdot Re_{\theta c}} \\ F_{onset2} &= \min(\max(F_{onset1}, F_{onset1}^4), 2.0) \\ F_{onset3} &= \max\left(1 - \left(\frac{R_t}{2.5}\right)^3, 0\right) \\ F_{onset} &= \max(F_{onset2} - F_{onset3}, 0), \end{aligned} \quad (2.3.17)$$

where

$$\begin{aligned} R_t &\equiv \frac{\nu_T}{\nu} \\ R_\nu &\equiv \frac{d^2|S|}{\nu}. \end{aligned} \tag{2.3.18}$$

Note that the criterion of onset is now controlled by a local parameter R_ν instead of a integral parameter $R_{\theta t}$ in Equation (2.3.2). So far, $Re_{\theta c}$ and F_{length} still need to be determined so as to let production term (2.3.15) be well defined. In Langtry and Menter (2009), these two variables are both functions of $\widetilde{Re_{\theta t}}$, which is the solution of Equation (2.3.13). Data correlations are used to construct the functions for $Re_{\theta c}$ and F_{length} in γ equation, and $Re_{\theta t}$ in $\widetilde{Re_{\theta t}}$ equation.

The idea is similar to earlier models that specify transition location, then solve a γ -equation to represent the transitional zone. But in Langtry and Menter (2009) the data correlation involved in the source term $P_{\theta t}$ in Equation (2.3.13) invokes the mean velocity and the streamline direction. That data correlation is not Gallilean invariant, which is problematic for multiple moving walls in the domain.

Another key point is the sink term E_γ in Equation (2.3.14). Its effect is to drive γ towards zero in laminar boundary layer so that a trivial solution $\gamma = 1$ can be avoided. This idea is also used in the present model. More discussion will be given below.

For the purpose of explanation, the model introduced above is not exactly the same as the one in Langtry and Menter (2009). More parameters and complicated correlations are used to match the experimental data.

2.3.4 Transition Modeling for Rough Wall Cases

A few recent studies proposed roughness induced transition models. Some of them are based on a data-correlation as the criteria of transition onset. In general, the correlation is regarding the critical momentum thickness Reynolds number at the transition location, $Re_{\theta t-rough}$. Its form is $Re_{\theta t-rough}$ as a function of critical Reynolds number for smooth walls $Re_{\theta t-smooth}$, the roughness parameter, and turbulence intensity. The correlation in Stripf et al. (2009a) depends on the effects of both the roughness height and density, while Boyle and Stripf (2009) propose a simpler formula, which only depends on the roughness height. The former needs more information about the roughness geometry than the latter, and in addition, the dimensionless

roughness height used by the former is the ratio of the true roughness height to the displacement boundary layer thickness, r/δ_* , rather than the more general form, $r^+ = ru_*/\nu$. r is the roughness height, and u_* , defined as $u_*^2 = (\nu + \nu_T)\partial_n U|_w$ for rough walls, is the friction velocity. [Lorenz et al. \(2013\)](#) extended Stripf's onset correlation based on more transition onset data, including more roughness geometry parameters.

To complete this type of models, an intermittency expression depending on the stream-wise coordinate downstream of transition onset, and a roughness turbulence model for the fully turbulent region, are needed. More details about the roughness model for fully turbulent boundary layers will be discussed below in Section [3.4.1](#).

For actually rough surfaces, roughness is parameterized by equivalent sand grain roughness, r . The rough surface is replaced by an effective, smooth surface, on which new boundary conditions are imposed. Although the geometry of real roughness is required by some correlations that evaluate the equivalent sand grain roughness, a correlation proposed by [Koch and Smith \(1976\)](#) provides a simple way to obtain the equivalent sand grain roughness solely from statistical parameters of the surface. That method was modified by [Boyle and Stripf \(2009\)](#) to obtain better agreement with the measured data. The revised correlation for r is

$$r = 4.3R_{rms}(1 + C_{sk}S_k), \quad (2.3.19)$$

where C_{sk} is set to 1.0, and the root mean square roughness height R_{rms} and skewness S_k are both statistical parameters, which read

$$R_{rms} = \sqrt{\frac{\sum_{i=1}^n (y_i - \bar{y})^2}{n - 1}},$$

and

$$S_k = \frac{\sum_{i=1}^n (y_i - \bar{y})^3}{nR_{rms}^3}.$$

Here n is the number of grain elements in roughness calculation.

As the correlation proposed by [Boyle and Stripf \(2009\)](#) is a simple one, it will be used in the next chapter, to calibrate parameters. In this approach, transition starts when the momentum thickness Reynolds number Re_θ reaches a critical value, $Re_{\theta t}$.

$$Re_{\theta t-rough} = \frac{Re_{\theta t-smooth}}{1 + Tu^{-0.625}(0.05(r^+ - 5))^{1.25}}, \quad (2.3.20)$$

Tu is the free-stream turbulence intensity at the transition onset location, and r^+ is the dimensionless roughness height. $Re_{\theta t-smooth}$ is evaluated by Equation (2.3.1). The term $r^+ - 5$ implies that a surface roughness can be considered hydraulically smooth if r^+ is less than 5. One can also notice that by this correlation, the transition onset becomes independent of the local turbulence intensity at high r^+ values.

Another type of approach is based on transport equations, using local variables. [Dassler et al. \(2010\)](#) proposed an extension of an existing transition model for smooth walls, which is known as the $\gamma - Re_{\theta t}$ model ([Menter et al., 2006a,b](#); [Langtry and Menter, 2009](#)). An additional transport equation is added on for a “Roughness Amplification”, A_r , that serves as a transition onset criterion. The production term of the transport equation for $\widetilde{Re_{\theta t}}$ in the $\gamma - Re_{\theta t}$ model is modified by a function of A_r to introduce effects of surface roughness.

A more recent paper [Elsner and Warzecha \(2014\)](#) combined the roughness transition model by [Stripf et al. \(2009a\)](#) and the $\gamma - Re_{\theta t}$ model. The transported variable $\widetilde{Re_{\theta t}}$ in the smooth wall model is modified based on the transition onset criterion given by [Stripf et al. \(2009a\)](#). However, the integral quantity δ_* has to be calculated at each time step, so this model is not based on strictly local variables.

CHAPTER 3. DEVELOPMENT OF THE MODEL

3.1 Introduction

This chapter will explain the rational of the basis of the proposed model first. Then the development of the model formulation will be introduced term by term and the roles of tunable parameters will be illustrated.

3.2 Rational of the Current Model

A data correlation given by [Praisner and Clark \(2007\)](#) shows that

$$\Theta_{transition}^2 = 0.07 \frac{\nu \lambda_{\infty}}{u'_{\infty}}. \quad (3.2.1)$$

$\Theta_{transition}$ is the momentum thickness at transition. λ_{∞} is referred to as the free-stream integral length scale, and u' the magnitude of the streamwise velocity fluctuation. The data cover a wide range of pressure gradients, Reynolds numbers, free-stream turbulence intensities and length scales as well as including low supersonic Mach numbers. All those data were collapsed by (3.2.1) independently of all other parameters. [Praisner and Clark \(2007\)](#) cite the estimate $C_{\mu}\omega = u'/\lambda$ for the variable of the $k - \omega$ model. Then (3.2.1) becomes

$$\Theta_{transition}^2 = \frac{7\nu}{9\omega_{\infty}}. \quad (3.2.2)$$

Interestingly, only the time scale of the free-stream turbulence is involved in this correlation. That seems to be too simple, since other data correlations invoke the free-stream turbulence intensity in addition to the dependency on the rate of turbulence decay. But what is most interesting, is that when turbulence scale is included, pressure gradients and other parameters are secondary. Turbulence scale involves the free-stream eddy viscosity $k_{\infty}/\omega_{\infty}$ and the dissipation rate $C_{\mu}k_{\infty}\omega_{\infty}$.

In the present model, the value of γ varies from unity within free-stream turbulent flow to zero in the laminar boundary layer. The function γ is used to suppress production of the turbulent kinetic energy. Bypass transition is initiated through the diffusion of free-stream disturbances into the boundary layer. As γ rises from zero toward unity within the boundary layer, production of γ switches on and the eddy viscosity rises. Meanwhile, in order to have the laminar boundary layer before transition, a sink term is invoked to work within the boundary layer and drive γ towards zero. This model was originally proposed in Durbin (2012). That formulation was deficient in the sink term, and was only tested by boundary layer computations. It contained no method to represent transition in separated flow.

3.3 Modeling for Smooth Wall Cases

The current model is derived from a basic model published in Durbin (2012). The intermittency transport equation in that model is of the form

$$\frac{D\gamma}{Dt} = \partial_j \left[\left(\frac{\nu}{\sigma_l} + \frac{\nu_T}{\sigma_\gamma} \right) \partial_j \gamma \right] + F_\gamma |\Omega| (\gamma_{max} - \gamma) \sqrt{\gamma}. \quad (3.3.1)$$

with the boundary conditions $\gamma = 1$ in the free-stream and $\partial_n \gamma = 0$ on walls. $|\Omega|$ is the mean vorticity. An assessment of this initial approach showed good agreement with the experimental data in flat plate cases, both with and without pressure gradient. The model did not depend explicitly on the pressure gradient, which is consistent with the fact that turbulence closures generally do not depend directly on the pressure gradient.

The formulation (3.3.1) applied only to bypass transition in attached flow and was implemented in a boundary layer code. In order to extend its application to general CFD codes and hence to predict more practical engineering flows, some changes have been made.

Consider an intermittency transport equation as follows,

$$\frac{D\gamma}{Dt} = \partial_j \left[\left(\frac{\nu}{\sigma_l} + \frac{\nu_T}{\sigma_\gamma} \right) \partial_j \gamma \right] + P_\gamma - E_\gamma. \quad (3.3.2)$$

The source term is in the same form as (3.3.1),

$$P_\gamma = F_\gamma |\Omega| (\gamma_{max} - \gamma) \sqrt{\gamma}. \quad (3.3.3)$$

The sink term is defined as,

$$E_\gamma = G_\gamma F_{turb} |\Omega| \gamma^{1.5}. \quad (3.3.4)$$

All the factors and constants will be explained in the following sections.

3.3.1 Diffusion Term

The influence of the two constants σ_l and σ_γ on the transition in the diffusion term is given below. They are set to be 5.0 and 0.2, respectively.

From the diffusion term itself, we can predict that increasing σ_γ decreases turbulent diffusivity and delays transition, and vice versa. In the current model, σ_γ is selected to be 0.2. If it is doubled or more, the diffusion is suppressed and the transition delayed. The model is less sensitive to this parameter once it becomes less than 0.2. When σ_γ is halved, the result changes very slightly; but it does give obvious early transition when σ_γ is 0.02 or even smaller. This is due to the sink term which is designed to drive γ to zero in order to have a laminar region before transition. After transition, the sink vanishes and hence just doubling the value of σ_γ delays the transition significantly. See Figure 3.3.1. Skin friction coefficient (C_f) curves are plotted along the stream-wise direction of a flat plate test case, T3A, one of the T3 series of flat-plate experiments conducted by the European Research Community on Flow Turbulence and Combustion (ERCOFTAC). See Langtry and Menter (2009) and Durbin (2012).

However, the effect of σ_l is a little bit subtle. When it is doubled, the C_f curve transitions early; whereas, transition occurs further downstream if σ_l is halved – a reverse effect of σ_γ (see Figure 3.3.2). Durbin (2012) attributes this to alteration of the mean shear in the upper part of the boundary layer. Decreasing σ_l appears to decrease the mean shear and hence generate lower k and delay the transition. To illustrate the respective effects of the laminar and turbulent diffusivity, the diffusion term with another three cases – only $\nu = 0$, only $\nu_T = 0$ and $\nu = \nu_T = 0$ are set and compared with the normal case. See Figure 3.3.3, and the black lines represent the profiles of the δ_{99} boundary layers. The deficiency of laminar diffusion, i.e. $\nu = 0$, enhances diffusion with high values of γ in the boundary layers. The lack of turbulent diffusion presents an opposite effect.

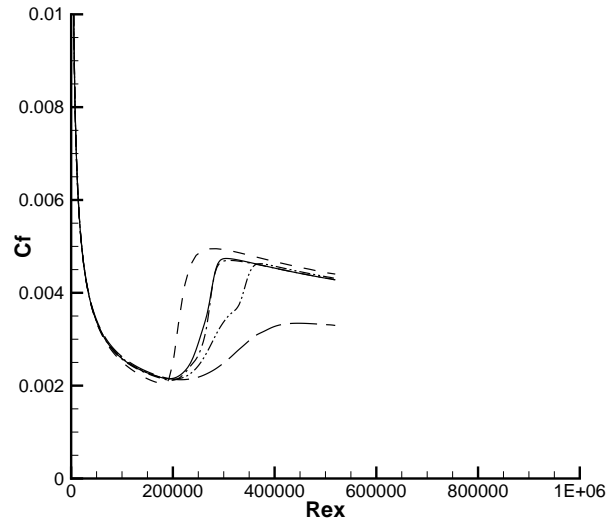


Figure 3.3.1 Sensitivity of σ_γ to the transition location. $\sigma_\gamma = 0.2$ (solid), $\sigma_\gamma = 0.02$ (dash), $\sigma_\gamma = 0.1$ (dash-dot), $\sigma_\gamma = 0.4$ (dash-dot-dot), $\sigma_\gamma = 0.8$ (long-dash).

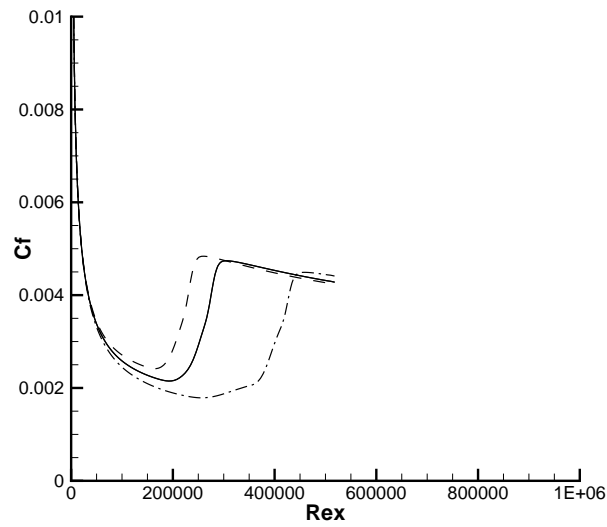


Figure 3.3.2 Sensitivity of σ_l to the transition location. $\sigma_l = 5.0$ (solid), $\sigma_l = 10.0$ (dash), $\sigma_l = 2.5$ (dash-dot).

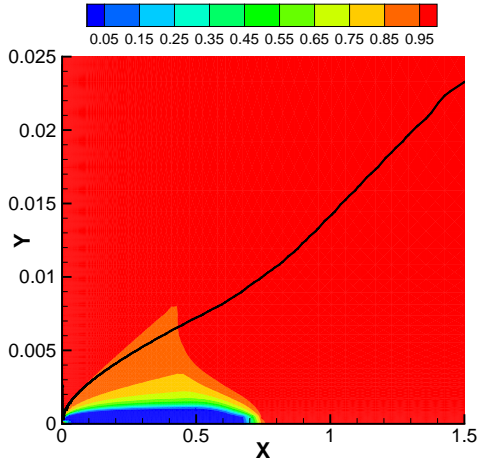
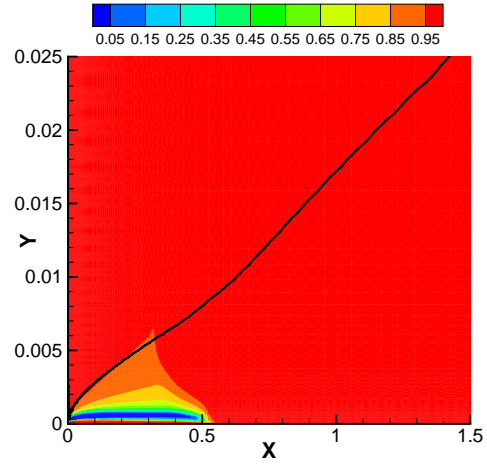
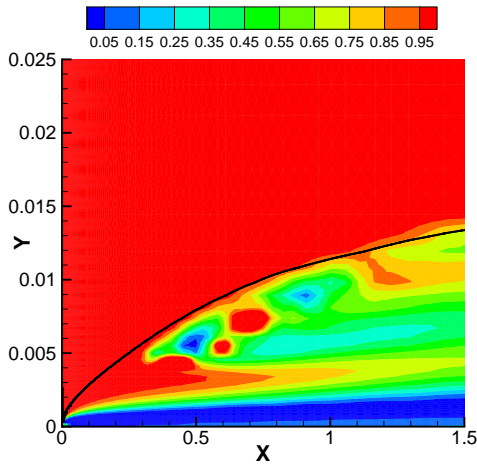
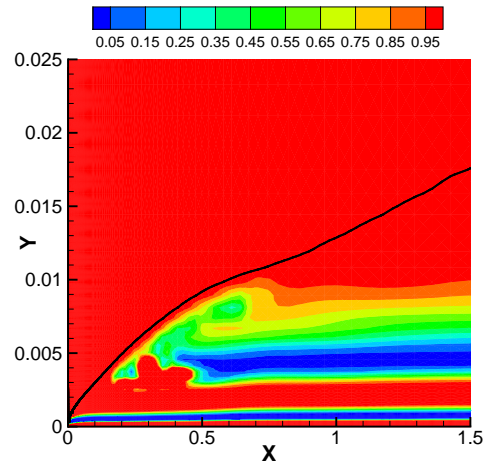
(a) ν and ν_T are both normal values.(b) $\nu = 0$ but ν_T is normal.(c) ν is normal but $\nu_T = 0$.(d) ν and ν_T are both zero.

Figure 3.3.3 Contours of γ for the T3A case, with different values of ν and ν_T in the diffusion term. The black lines represent the profiles of the δ_{99} boundary layers.

3.3.2 Source Term

Note that $\gamma_{max} = 1.1$ instead of unity is placed in the source term (Equation 3.3.3). This is in order to enhance the effect of the source term to drive γ to one. Accordingly, γ could exceed unity due to such source, which is not allowed. After each step of the computation, γ is forced

to the value of $\min(\gamma, 1)$ to prevent values greater than unity. This has a small effect, but it does force a full transition to turbulence guaranteeing γ to be unity after transition. This clipper will be embedded into the standard $k - \omega$ RANS model with which Equation (3.3.2) is coupled.

Mean shear is represented by the magnitude of the mean rotation rate $|\Omega|$ (i.e. $\sqrt{2 \cdot \Omega_{ij} \Omega_{ji}}$). It recalls that turbulence is caused by mean shear. $|\Omega|$ is an invariant measure of shear, and it vanishes in the irrotational free-stream.

The factor F_γ is a function of two parameters, R_ν and T_ω . F_γ switches on as transition proceeds. Once it comes into play, γ will increase up to unity within the region that F_γ affects. Therefore, turbulent kinetic energy k increases as well as the eddy viscosity. Figure 3.3.4 depicts the contours of the source term, whose trigger-on point is at the upstream of the transition onset location. By comparing Figure 3.3.3(a), the effect of the source term is clear to be seen.

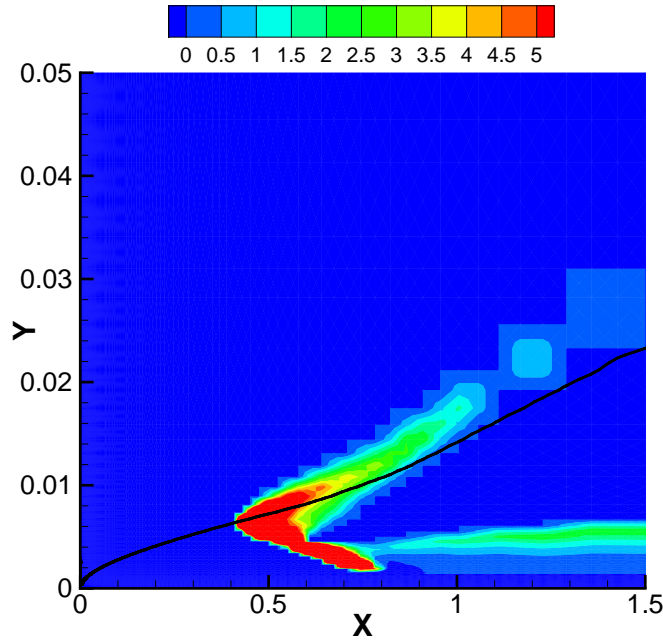


Figure 3.3.4 Contours of the source term for the T3A case. The black line represents the profile of the δ_{99} boundary layer.

Three non-dimensional parameters are involved, where d is distance to the wall. R_t is the ratio of eddy viscosity to molecular viscosity, namely the turbulent Reynolds number. The

parameter T_ω is R_t multiplied by $|\Omega|/\omega$ to make it vanish in the free-stream. Another view of T_ω is that in parallel flow $T_\omega = |\overline{uv}|/\nu\omega$. In the log-layer it equals to $u_*^2/\nu\omega = 1/\omega_+$.

$$\left\{ \begin{array}{l} R_t \equiv \frac{\nu T}{\nu}, \\ T_\omega \equiv R_t \frac{|\Omega|}{\omega}, \\ R_\nu \equiv \frac{d^2 |\Omega|}{2.188 \nu}. \end{array} \right. \quad (3.3.5)$$

R_ν is the vorticity Reynolds number, which depends only on local variables. Note that near a wall it goes like wall distance squared, i.e. $R_\nu \rightarrow y_+^2/2.188$, as $y_+ \rightarrow 0$. It is defined as such that in the Blasius boundary layer its maximum in the normal wall direction is equal to the momentum thickness Reynolds number: $\max_y R_\nu = R_\theta$. When the boundary layer is subjected to pressure gradients, the relationship between momentum thickness and vorticity Reynolds number will change due to the change of the profile of R_ν . In Falkner-Skan boundary layers $\max_y R_\nu$ is less than R_θ for favorable pressure gradients and greater than R_θ for adverse pressure gradients. So a fixed value of R_ν will correspond to a higher R_θ for favorable pressure gradients and a lower R_θ as the pressure gradient becomes adverse. In addition, this relative relation between R_ν and R_θ can also be used to predict separation-induced transition when strong adverse pressure gradient exists.

[Langtry and Menter \(2009\)](#) also stated a physical reason of using R_ν , by arguing that the combination $y^2|\Omega|$ is responsible for the growth of disturbances inside a boundary layer, while ν is responsible for their damping. To be concise, R_ν implicitly contains information on R_θ which in data correlations is used to indicate the onset of transition.

Now come back to the definition of F_γ . T_ω is used to form a critical Reynolds number, R_c . It is a decreasing function of T_ω . If the turbulence intensity is low, T_ω will be low and R_c will be high. R_c is a linear ramp down between 400 and 40.

$$R_c = 400 - 360 \min\left(\frac{T_\omega}{2}, 1\right). \quad (3.3.6)$$

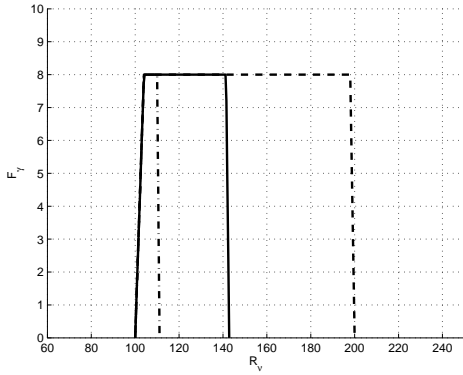
As the local Reynolds number R_ν crosses R_c from below, F_γ ramps up from zero. Again a linear ramp is used. Meanwhile, a ramp down is included if the Reynolds number crosses

$R_{\nu bound} = 100/0.7$ without the flow becoming turbulent. This approach is to suppress F_γ for low free-stream turbulence. The concrete formula for F_γ is

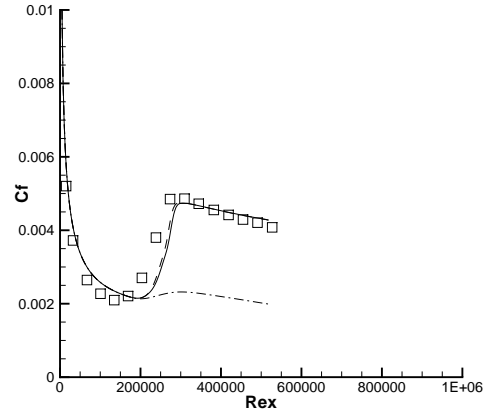
$$F_\gamma = 2 \max [0, \min (100 - 0.7R_\nu, 1)] \times \min [\max (R_\nu - R_c, 0), 4]. \quad (3.3.7)$$

In other words,

$$F_\gamma = \begin{cases} 0, & \text{if } R_\nu \leq R_c, \text{ or if } R_\nu \geq 100/0.7, \\ 8, & \text{if } R_\nu > R_c + 4 \text{ and } R_\nu \leq 100/0.7 - 1. \end{cases}$$



(a) F_γ vs. R_ν with $R_c = 100$.



(b) C_f with different $R_{\nu bound}$.

Figure 3.3.5 $R_{\nu bound}$ is equal to 100/0.5 (dash); 100/0.7 (solid); 100/0.9 (dash-dot).

Note that this is a recalibration of the formulas in Durbin (2012) because of the addition of E_γ to Equation (3.3.2). The specific upper limit of 4 in the second factor of the right-hand side of Equation (3.3.7) has a small effect; a greater value does not change the result very much. A plot of F_γ versus R_ν is given in Figure 3.3.5, when the critical Reynolds number R_c is 100, which illustrates how F_γ ramps up then down. The upper limit of R_ν where F_γ crosses from non-zero to zero ($R_{\nu bound}$) is sensitive to the location of transition. If it is set to be greater than 100/0.7, transition is accelerated; if it is less, transition is delayed. However, due to the effect of the sink term discussed in the next section, if for example $R_{\nu bound} = 100/0.5$ is used, the C_f

curve will be barely changed rather than showing an early transition. When $R_{\nu bound} = 100/0.9$, it does result in a late transition.

3.3.3 Sink Term

Without a sink term, the γ -equation (3.3.2) would have the solution $\gamma \equiv 1$. The numerical elliptic solver will converge to unity within the whole domain, which will produce fully turbulent results. See Figure 3.3.6.

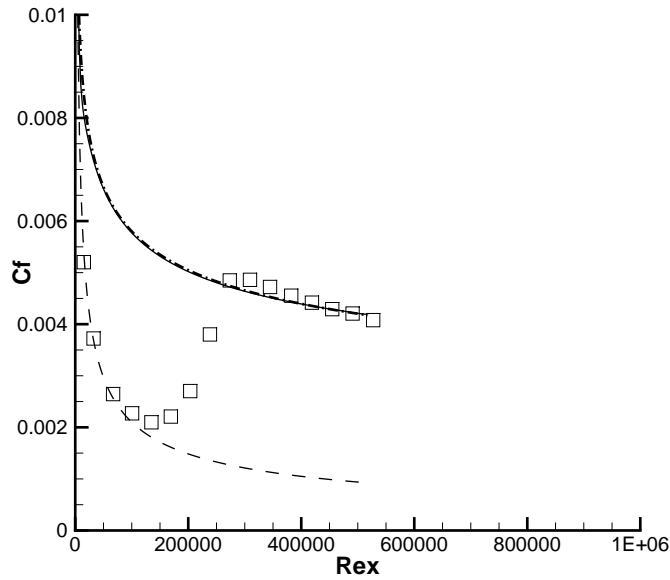


Figure 3.3.6 Skin friction coefficient vs. Re_x in a flat plate test case (T3A); the solid curve represents the result based on the model without sink term. The other three represent the experimental data (square), theoretical laminar (dash) solution, and semi-empirical turbulent solution (dash-dot) respectively.

In order to force γ close to zero within the laminar region, a sink term is added in Equation (3.3.2). Another feature of the sink term is that it has to vanish after transition because γ is supposed to be unity in the fully turbulent region. This feature is implemented by the multiplication of two functions, G_γ and F_{turb} . See Figure 3.3.7 – contours of the sink term, along with Figure 3.3.3(a) and 3.3.4. γ is low within the laminar region under the work of the sink term and rises to unity downstream after the source term switches on whereas the sink

switches off. Note that the sink term in [Langtry \(2006\)](#) does not shut off in the fully turbulent region. γ remains very small near the wall after transition.

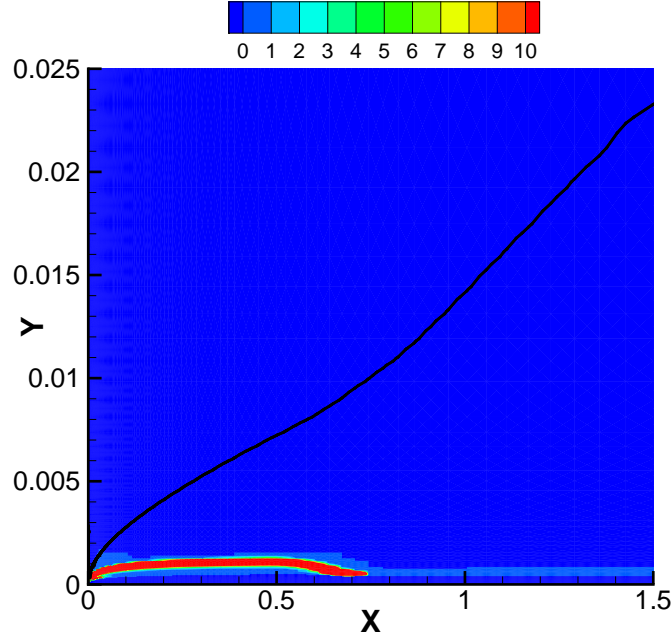


Figure 3.3.7 Contours of the sink term for the T3A case. The black line represents the profile of the δ_{99} boundary layer.

The definition of G_γ is similar to F_γ in the source term, as defined in Equation (3.3.8). It is used to ensure the laminar region before transition. It ramps up from $R_\nu = 18$ and ramps down after $R_\nu = 100$. See Figure 3.3.8. A factor 7.5 in (3.3.8) is chosen for the strength of the sink term.

$$G_\gamma = 7.5 \max [0, \min (100 - R_\nu, 1)] \times \min [\max (R_\nu - 18, 0), 1]. \quad (3.3.8)$$

In other words,

$$G_\gamma = \begin{cases} 0, & \text{if } R_\nu \leq 18, \text{ or if } R_\nu \geq 100, \\ 7.5, & \text{if } R_\nu > 19 \text{ and } R_\nu \leq 99. \end{cases}$$

The lower bound $R_{\nu\text{bound}} = 18$ is critical, to some extent. In the test case T3B ([Langtry and Menter, 2009](#)), with high free-stream turbulence intensity, the model will be invalid if $R_{\nu\text{bound}}$ too large.

For such a case, the laminar region is thin and short. Therefore, a relatively high $R_{\nu}lbound$ may not catch the thin laminar region near the wall and hence the sink term may vanish. See Figure 3.3.8. Too small a value for $R_{\nu}lbound$ is not proper either because the sink term is supposed to vanish after transition. Recall that R_{ν} goes like y_{\mp}^2 near the wall so that too small $R_{\nu}lbound$, say 0, makes G_{γ} non-zero into the turbulent region, with the sink term not vanishing.

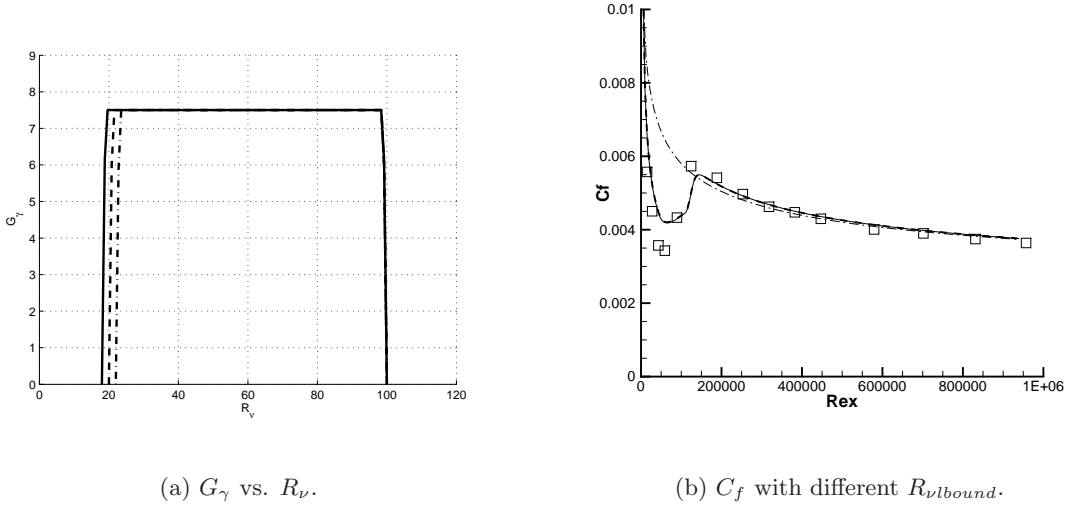


Figure 3.3.8 $R_{\nu}lbound$ is equal to 18 (solid); 22 (dash); 26 (dash-dot). From 18 to 22, the difference is tiny; but from 22 to 26, C_f curve suddenly becomes fully turbulent.

F_{turb} is a function of R_{ν} and R_t . It will vanish outside the laminar boundary layer. It is defined as,

$$F_{turb} = e^{-(R_{\nu}R_t)^{1.2}}. \quad (3.3.9)$$

The power 1.2 is selected to match data. A large value of it will reduce the region affected by F_{turb} , which in turn suppresses the sink and leads to early transition.

3.3.4 Separation Modification

When a laminar boundary layer approaches separation, inflection point instability becomes a cause of transition. In this mechanism, an instability wave serves as the precursor to transition,

and the phenomenology is different from bypass transition. However, free-stream turbulence can promote break down of instability waves into turbulence.

Langtry (2006) pointed out that when separated flow transition was involved, their model (without modification for separation) would predict the turbulent reattachment location too far downstream. The same issue happens to the present model. And in some cases the reattachment may not occur at all. The low turbulent kinetic energy k in the separating shear layer is the deficiency of the model because k grows too slowly to cause the boundary layer to become turbulent and reattach at the right location. The main idea proposed by Langtry (2006) is to allow the intermittency function to exceed 1 wherever the laminar boundary layer separates. This will lead to large production of k and hence allow k to grow rapidly to accelerate the transition or reattachment.

In order to invoke this idea, a criterion to locate the laminar separation should be introduced. Consider a series of velocity profiles of the Falkner-Skan boundary layer. See Figure 3.3.9. The parameter yU''/U' (blue curves) will have a positive region in adverse pressure gradients and become large if the flow separates. It does not involve turbulence parameters and hence may be a good parameter to locate the laminar separation. Replacing U' by an invariant of mean velocity gradient, $|S|$, the parameter becomes $d \cdot (\mathbf{n}_w \cdot \nabla|S|) / |S|$. d is the wall distance and \mathbf{n}_w is the unit normal vector of the wall. These two are not local variables, and they have to be evaluated by locating the closest point of each grid to the wall. $|S|$ is defined as $\sqrt{S_{ij}S_{ji}}$ so that $\sqrt{2}|S|$ equals to $|\partial_y U|$ in parallel flows.

Note that $\nabla|S|$ (i.e. $|U'|'$) is used instead of ∇S (i.e. U''). The difference between these two is illustrated in Figure 3.3.10 (see the two right most curves). The inflection point, marked by a circle, is what is needed to locate, i.e. the zeros in the two right most curves. Close to the wall, the right most blue curve appears to cross the vertical axis but in fact here is a jump rather than a continuous steep rise. Hence both can locate the inflection point properly. While ∇S is ambiguous and complex since S is a tensor rather than a scalar, the scalar $|S|$ is selected for simplicity.

The final form of parameter that is used is as follows,

$$R_s \equiv d \cdot \frac{\mathbf{n}_w \cdot \nabla |S| \omega}{\sqrt{2} |S|^2}. \quad (3.3.10)$$

This is actually the parameter described above multiplied by $\omega / (\sqrt{2} |S|)$. The extra factor increases R_s in the separated layer.

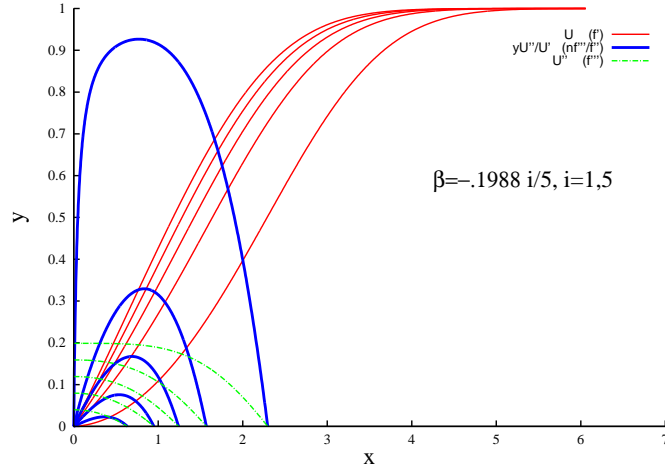


Figure 3.3.9 The blue curve evaluates yU''/U' for Falkner-Skan boundary layer profiles. The pressure gradient parameter $\beta = -0.1988$ is just before separation. x-axis: vertical coordinate to the wall; y-axis: velocity and functions of its derivative.

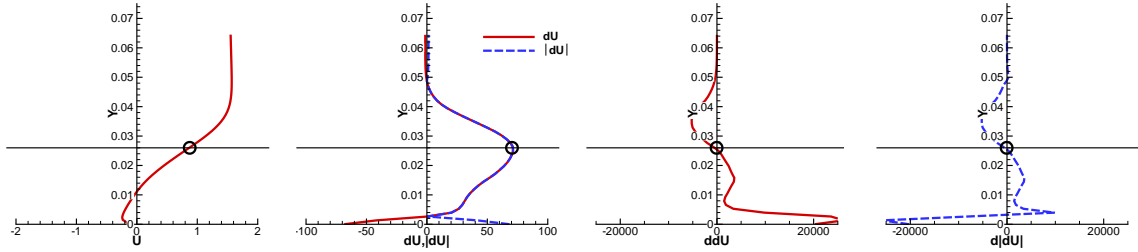


Figure 3.3.10 Comparison of a velocity profile in a separated region and related derivatives. U , U' and $|U'|$, U'' , and $|U''|$ are plotted from left to right. The velocity profile was extracted within the separated region from LES data by [Lardeau et al. \(2012\)](#). $|U''|$ (i.e. $\nabla |S|$), rather than U'' is actually used to define the parameter R_s in Equation (3.3.10).

The effective intermittency function γ_{eff} in Equation (3.3.11) is the modification to the intermittency function γ for predicting transition by laminar separation. The limiter $\min(1, \gamma)$

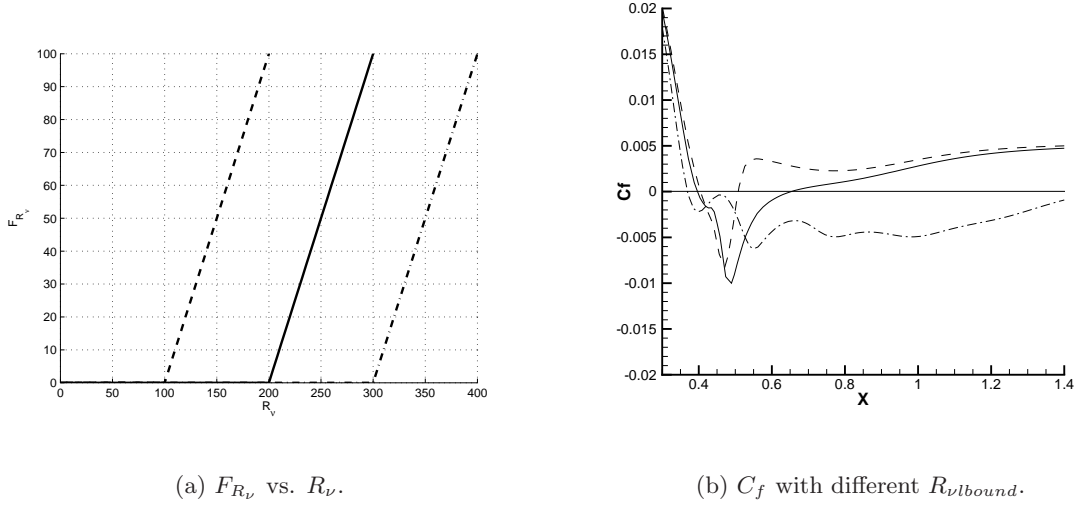


Figure 3.3.11 Linear ramps for F_{R_ν} . $R_{\nu lbound} = 200$ (solid); $R_{\nu lbound} = 100$ (dash) and too early reattachment is seen; $R_{\nu lbound} = 300$ (dash-dot) and no reattachment is seen.

was explained above in Section 3.3.2.

$$\gamma_{eff} = \max[\min(1, \gamma), \min(2, F_{R_t} F_{R_\nu} F_{R_s})]. \quad (3.3.11)$$

This modification involves 3 factors defined as follows,

$$F_{R_t} = e^{-(R_t/10)^3}, \quad (3.3.12)$$

$$F_{R_\nu} = \max(R_\nu - 200, 0), \quad (3.3.13)$$

$$F_{R_s} = \min[1.0, \max(10 + 5R_s, 0)] \\ \times \min[1.0, \max(10 - 5R_s, 0)], \quad (3.3.14)$$

They are functions of R_t , R_ν , and R_s , respectively. Linear ramps are again used as in the source and sink terms. The test case chosen to evaluate the model is a flat plate separated flow which has been simulated in both [Wissink and Rodi \(2006b\)](#) and [Lardeau et al. \(2012\)](#) using

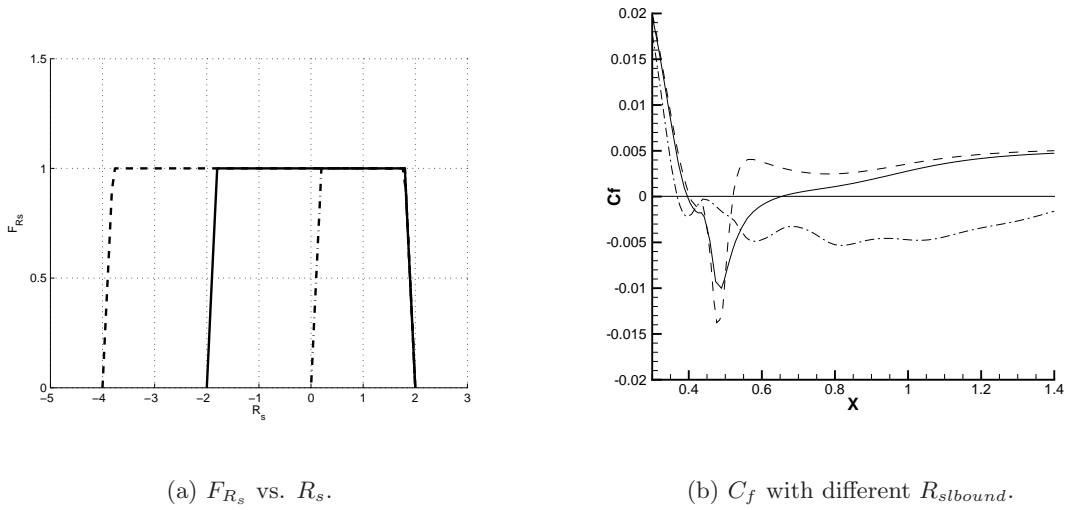


Figure 3.3.12 Linear ramps for F_{R_s} . $R_{slbound} = -2$ (solid); $R_{slbound} = -4$ (dash) and too early reattachment is seen; $R_{slbound} = 0$ (dash-dot) and no reattachment is seen.

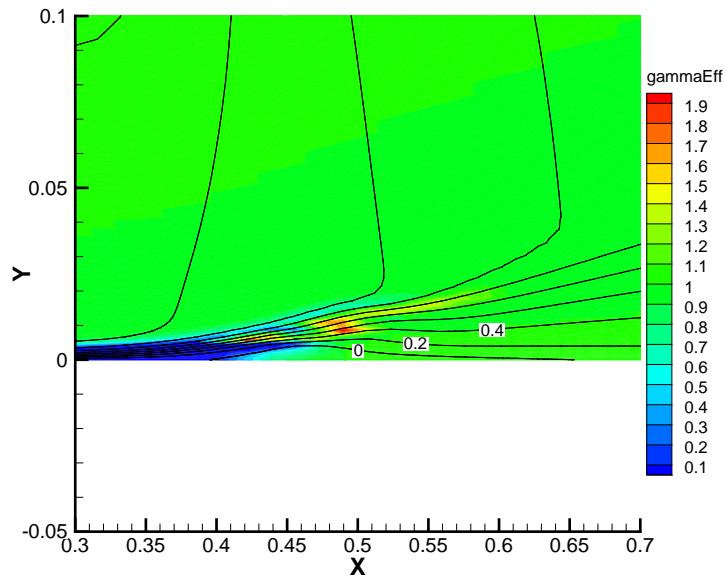


Figure 3.3.13 Distribution of γ_{eff} and line contours of U_x around the separation bubble for the flat plate separation test case.

direct numerical simulation (DNS) and large eddy simulation (LES) respectively. F_{R_s} as defined above serves as a factor to locate the separation and switch the modification. In separated flow, F_{R_s} is positive between the layers where $|S| = 0$ and $\mathbf{n}_w \cdot \nabla|S| = 0$. The influence of the lower bound of R_s for the ramp up is shown in Figure 3.3.12. As to the upper bound of the ramp down, values greater than 2 affect very little since R_s itself has an upper bound. F_{R_ν} is used for both triggering the modification and representing its strength. Shown by Figure 3.3.11, the greater the threshold R_ν is, the later the reattachment will be. F_{R_t} plays the role of removing the modification in the free-stream. Figure (3.3.13) displays the distribution of γ_{eff} along with the contour of stream-wise velocity around a separated region. γ_{eff} is greater than 1 after the separation point and becomes unity when the flow is fully turbulent. Before the separation point, γ_{eff} is close to zero in the boundary layer. It exceeds unity only within a thin region around the separation bubble to achieve the reattachment. It appears to be a good parameter to represent the separation-induced transition.

3.3.5 Revision of the $k - \omega$ Model

The current formulation is applied to the $k - \omega$ RANS closure (Wilcox, 1993). The production term of the k equation is multiplied by γ_{eff} . This is the only appearance of γ within the turbulence model.

$$\frac{Dk}{Dt} = P_k - C_\mu k\omega + \partial_j \left[\left(\nu + \frac{\nu_T}{\sigma_k} \right) \partial_j k \right], \quad (3.3.15)$$

$$P_k = \min \left(2\nu_T |S|^2, k|S|/\sqrt{3} \right) \gamma_{eff}, \quad (3.3.16)$$

$$\frac{D\omega}{Dt} = 2C_{\omega 1} |S|^2 - C_{\omega 2} \omega^2 + \partial_j \left[\left(\nu + \frac{\nu_T}{\sigma_\omega} \right) \partial_j \omega \right], \quad (3.3.17)$$

where $C_\mu = 0.09$, $C_{\omega 1} = 5/9$, $C_{\omega 2} = 3/40$ and $\sigma_\omega = \sigma_k = 2$. The eddy viscosity ν_T is k/ω . Non-zero γ will diffuse into the boundary layer, allowing k to be produced, thereby creating eddy viscosity and further enhancing the diffusion of γ . In this way, transition occurs by penetration of free-stream turbulence into the boundary layer via molecular and turbulent diffusion.

The rationale of the limiter for the production term in (3.3.16) is explained in Durbin and Reif (2011) (page 139-141). It is to fix the stagnation-point anomaly of turbulence kinetic energy. For example, in some cases like flow around a blade leading edge, the limiter can avoid unphysically large levels of k near the stagnation-point.

This model has been published in Ge et al. (2014).

3.4 Modeling for Rough Wall Cases

In this section, the details of the roughness modification will be presented and the rationale will be provided. The modification consists of two steps: the first step is to add an effective displacement the origin, depending on the equivalent sand grain roughness height, to the wall distance. The data correlation (2.3.20) is used to calibrate the effective displacement. The second step is to modify some parameters in the sink term of the intermittency equation in order to make the model suitable to turbine blade cases where, there is a strong acceleration downstream of the stagnation point.

Before introducing the roughness modification, a roughness model is required to predict fully turbulent boundary layers over rough walls. In the literature, different boundary conditions were used to represent the roughness effects with a dependence of roughness heights and effective wall origins. The first subsection below is a review for such models.

3.4.1 Prediction for Fully Turbulent Boundary Layers on Rough Walls

Surface roughness will increase the drag force. In a channel flow with constant pressure gradient, the increased drag would decrease the mass flux and hence the velocity profile would shift. In the log-law layer, the velocity profile impacted by roughness can be expressed in the form below,

$$\frac{U}{u_*} = \frac{1}{\kappa} \log(y^+) + B + \Delta B_r(r^+) \quad (3.4.1)$$

where u_* is the friction velocity, and r^+ is the dimensionless sand grain roughness height. See their definition in Section 2.3.4. Here $y^+ = yu_*/\nu$ and y is the wall distance. In log-law formulation, it is conventional to use y instead of d to denote the wall distance, while the latter is

preferred for the modeling formulation of the current work and used in other places throughout this thesis. The function $\Delta B_r(r^+)$ represent the alternation of the additive constant $B = 5.5$. [Ligrani and Moffat \(1986\)](#) proposed a curve fit based on the measured data,

$$\Delta B_r = \begin{cases} 0, & r^+ < 2.25, \\ \xi(8.5 - B - 1/\kappa \log(r^+)), & 2.25 \leq r^+ \leq 90, \\ 8.5 - B - 1/\kappa \log(r^+), & r^+ > 90. \end{cases} \quad (3.4.2)$$

These three formulas correspond to effectively smooth, transitionally rough, and fully rough conditions respectively. The blend function ξ is

$$\xi = \sin \left(\frac{\pi/2 \cdot \log(r^+/2.25)}{\log(90/2.25)} \right)$$

which increase from 0 to 1 through the transitionally rough range.

Based on the sand grain roughness, [Durbin et al. \(2001\)](#) proposed a rough wall modification for the two layer $k - \epsilon$ model. This approach is aimed to predict the shift of the velocity profiles due to roughness. An effective *displacement of the wall distance origin* is introduced and related to the sand grain roughness height through a calibration procedure. The effective displacement is related to a hydrodynamic roughness length in this paper, that is used to modify the length scales for the lower layer and the boundary condition for ϵ . The following equation is used to blend between the smooth and fully rough boundary conditions for k :

$$k|_w = \frac{u_*^2}{\sqrt{C_\mu}} \min \left[1, (r^+/90)^2 \right], \quad (3.4.3)$$

Note that this approach was originally developed only for sand roughness and should be adjusted if applied to other roughness geometries. To use this model for other roughness types, their equivalent sand grain roughness needs to be estimated in advance.

Similar roughness boundary conditions for fully turbulent boundary layer have been proposed to extend the standard $k - \omega$ model, such as the well-known Wilcox's roughness modification ([Wilcox, 1998](#)). Only the wall-value of ω is modified to model effects of surface roughness.

$$k|_w = 0,$$

$$\omega|_w = \frac{u_*^2}{\nu} S_r, \quad S_r = \begin{cases} (50/r^+)^2, & 5 < r^+ < 25, \\ 100/r^+, & r^+ \geq 25. \end{cases} \quad (3.4.4)$$

This is valid for values of r^+ up to about 400 in sand grain roughness. For $r^+ \leq$, the effectively smooth boundary conditions are

$$k|_w = 0,$$

$$\omega|_w = 60 \frac{\nu}{\beta y^2(1)}, \quad (3.4.5)$$

where $y(1)$ is the wall distance of the grid point next to the wall. Both [Dassler et al. \(2010\)](#) and [Elsner and Warzecha \(2014\)](#) used the $k - \omega$ -SST model, and they choose Wilcox's roughness boundary condition to predict the fully turbulent boundary layer with rough surfaces.

While the Wilcox model requires a very fine mesh resolution ($y^+(1) \approx 0.01$ or even less) and is not accurate for transitionally rough walls, newer models by [Seo \(2004\)](#) and [Knopp et al. \(2009\)](#) give satisfactory results with near wall grid spacing close to that for smooth walls ($y^+(1) \approx 0.3$ is sufficient). In addition, predictions of roughness effects under for the transitionally rough condition are improved by these models as well.

Under fully rough conditions, the log-layer solution $k = u_*^2 / \sqrt{C_\mu}$ extends to the effective wall origin, where the log-layer eddy viscosity $\nu_T = u_* \kappa (y + d_0)$ reduces to $u_* \kappa d_0$. Here d_0 is the effective displacement of the wall origin. d_0 can be determined analytically under fully rough conditions based on the shift of the velocity profile in the log-layer. This shift has been measured experimentally and fitted such that the new velocity profile can be written

$$U/u_* = 1/\kappa \log(y/r) + 8.5$$

where $\kappa = 0.41$. Then, if d_0 is defined in terms of U by

$$U/u_* = 1/\kappa \log((y + d_0)/d_0)$$

the last two equations give

$$\frac{y + d_0}{d_0} = \frac{y}{r} e^{8.5\kappa}$$

Using the approximation $d_0 \ll y$,

$$d_0 = e^{-8.5\kappa r} \approx 0.03r. \quad (3.4.6)$$

From the definition $\nu_T = k/\omega$, the boundary condition for ω under fully rough condition should be

$$\omega = \frac{u_*}{\sqrt{C_\mu \kappa d_0}}. \quad (3.4.7)$$

Generally, the ω boundary condition represented as

$$\omega|_w = \frac{60\nu}{\beta y_{eff}^2}, \quad (3.4.8)$$

where $y_{eff} = \max[y(1), y_r]$ in Knopp's model and $y_{eff} = (y(1) + y_r)$ in Seo's. Here $y(1)$ is the grid point next to the wall and

$$y_r = \frac{\nu}{u_*} \left(\frac{60\kappa\sqrt{C_\mu}}{\beta} d_0^+ \right)^{1/2},$$

to agree with (3.4.7), where $\beta = 0.075$.

The variable d_0^+ is a function of r_+ that is obtained by calibration against the log-layer displacement, $\Delta U(r^+)$ (Durbin, 2009). Knopp proposes

$$d_0^+ = 0.03r^+ \min \left[1, \left(\frac{r^+}{30} \right)^{2/3} \right] \min \left[1, \left(\frac{r^+}{45} \right)^{1/4} \right] \min \left[1, \left(\frac{r^+}{60} \right)^{1/4} \right]. \quad (3.4.9)$$

Seo gives

$$d_0^+ = \begin{cases} 0.56 \left(\frac{r^+}{20} \right)^{2.5} & ; 0 \leq r^+ < 20 \\ 0.63\zeta(r^+) + 0.028r^+ & ; 20 \leq r^+ < 90 \\ 0.031r^+ - 0.27 & ; 90 \leq r^+ \end{cases}$$

where $\zeta(r^+) = \sin[\pi((r^+ - 20)/70)^{0.9}]$. It is easy to see that ω_w decreases with increasing r^+ , which leads to increase of C_f .

Under transitionally rough conditions, Knopp et al. (2009) use a linear blending function

$$k|_w = \frac{u_*^2}{\sqrt{C_\mu}} \min(1, r^+/90), \quad (3.4.10)$$

for the k boundary condition, while Seo (2004) retains (3.4.3).

To correctly simulate the roughness effects on the skin friction and heat transfer coefficients in the fully turbulent regime, Equations (3.4.10)–(3.4.9) proposed by Knopp et al. (2009) are chosen as the boundary conditions for k and ω on rough walls because of its better behavior than Wilcox’s boundary conditions. The starting point of modeling for rough wall cases is to implement Knopp’s model in the code used by the present work and validate the implementation.

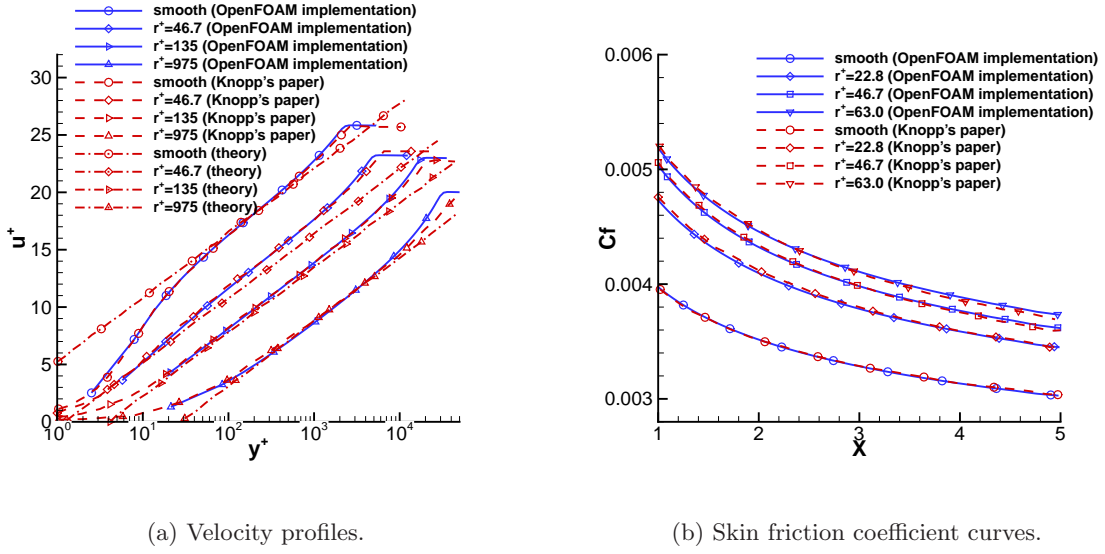
Figure 3.4.1 shows the velocity profiles and C_f curves for different roughness heights r^+ in the test cases by Ligrani and Moffat (1986). They are flat plate turbulent boundary layer flows over spherical roughness elements. Equivalent sand grain roughness heights are given in these cases. The inlet $Tu = 0.1\%$ and $R_t = 0.1$. Refer to Knopp et al. (2009) for more details about flow setup. Data from Knopp’s paper and the results from the author’s implementation are compared and very slight differences are obtained. The code platform is OpenFOAM. The existing $k - \omega$ model in OpenFOAM along with new boundary conditions for k and ω is used. The results for the smooth wall case in Figure 3.4.1 are gained by applying Equation 3.4.8 instead of the default boundary condition for ω in OpenFOAM. The curves marked by ‘theory’ in Figure 3.4.1(a) are calculated by Equation 3.4.1 and 3.4.2. More computation details will be described in the next chapter.

3.4.2 Modification on the Effective Wall Origin

Inspired by the idea of the equivalent sand grain roughness and the *displacement of origin* approach for the roughness modification in fully turbulent flow, a displacement of origin method is developed for the intermittency equation. (However, the sink term in the intermittency equation needs a non-displacement type of modification.) Equations (3.4.8), (3.4.9) and (3.4.10) are chosen as the boundary conditions for k and ω on rough walls.

To modify the smooth wall transition model, $C_r r$ is added to the original model wherever the wall distance appears.

$$R_\nu \equiv \frac{(d + C_r r)^2 |\Omega|}{2.188\nu}, \quad (3.4.11)$$



(a) Velocity profiles.

(b) Skin friction coefficient curves.

Figure 3.4.1 Validation for the implementation of the Knopp's rough wall boundary conditions applied to the standard $k - \omega$ turbulence model. The near wall grid resolution is $y^+(1) \approx 0.3$. Test case by [Ligrani and Moffat \(1986\)](#).

$$R_s \equiv (d + C_r r) \cdot \frac{\mathbf{n}_w \cdot \nabla |S| \omega}{\sqrt{2} |S|^2}, \quad (3.4.12)$$

where d is the true wall distance, r is the equivalent sand grain roughness height, and C_r is a constant coefficient. (See original definitions of R_ν and R_s in Section 3.3.)

The key modification is to R_ν . R_ν is a replacement for R_θ , which is used to indicate transition onset in data correlations. R_ν is therefore a typical parameter for transition modeling based on only local variable. For smooth surfaces, near the wall, $R_\nu \rightarrow d_+^2/2.188$ as $d_+ \rightarrow 0$. For rough surfaces, R_ν invokes a displaced origin and becomes non-zero at the wall.

To calibrate the coefficient C_r in Equations (3.4.11) and (3.4.12), a flat plate test case with zero pressure gradient is adapted from the T3A setup for smooth walls. The original free-stream Tu for T3A is 3.5%, but the transition location is more sensitive to roughness with lower free-stream Tu . Therefore $Tu = 1.5\%$ was selected for the present calibration. The inflow velocity $U_{in} = 5.2m/s$ and turbulence Reynolds number $R_t = \nu_T/\nu = 14$ are kept unchanged. The predicted critical Reynolds number Re_{θ_t} and the correlated $Re_{\theta_t-rough}$ from Equation (2.3.20), are in good agreement when $C_r = 0.26$. When evaluating $Re_{\theta_t-rough}$ using Equation (2.3.20),

$Re_{\theta t-smooth}$ was not obtained from Equation (2.3.1); instead, the predicted velocity profiles from simulations of smooth wall cases were integrated to compute $Re_{\theta t-smooth}$ and thereafter to calculate $Re_{\theta t-rough}$.

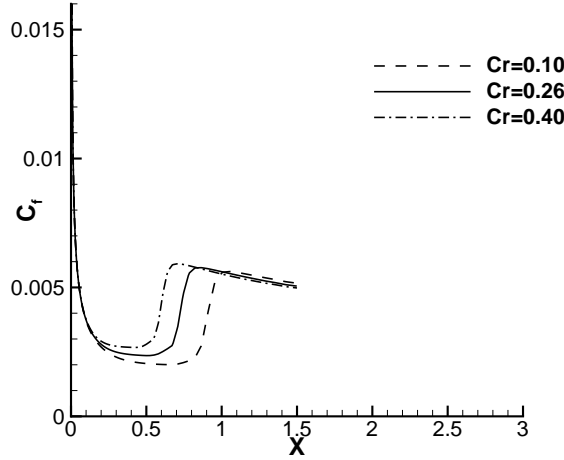


Figure 3.4.2 Effects of C_r . This test case is a flat plate case with inflow turbulence intensity $Tu = 1.5\%$. The roughness height $r = 10 \times 10^{-4}m$ is set unchanged for different C_r s.

Figure 3.4.2 shows how the coefficient C_r determines the transition location: with small C_r , the critical Reynolds number $Re_{\theta t}$ is overestimated, whereas early transition is predicted with large C_r . This is understandable since $C_r r$ defines the effective wall displacement, which is an indicator of the extent to which surface roughness will affect the near wall region of the boundary layer. For given r , the larger C_r , the farther the wall origin extends into the flow, and the earlier the transition occurs.

However, this simple change is not enough, even for flat plate cases. As one may expect, a change may bring improvement in one place, but it may cause some issues in another. In this case, the sink term will not vanish after transition is complete, which leads to the intermittency function γ not being unity. As a result, the skin friction will be under-estimated in the fully turbulent region. The lower R_ν bound, in the function G_γ , is modified to fix this issue.

To shed light on how this modification works for the intermittency equation, the expression

of the sink term of the intermittency equation (Section 3.3) is recalled:

$$E_\gamma = G_\gamma F_{turb} |\Omega| \gamma^{1.5}$$

with G_γ and F_{turb} defined as

$$G_{\gamma-smooth} = 7.5 \max [0, \min (100 - R_\nu, 1)] \times \min [\max (R_\nu - 18, 0), 1],$$

$$F_{turb-smooth} = e^{-(R_\nu R_t)^{1.2}}.$$

The subscript ‘smooth’ means the definition for a smooth wall, which will be changed for a rough wall. As mentioned above, when $r_+ > 5$, surface roughness will influence transition onset. Therefore, the sink term should be affected by the surface roughness. G_γ switches from 0 to 7.5 in the range $18 < R_\nu < 100$. Near the wall this implies $18 < d_+^2/2.188 < 100$ or $6.3 < d_+ < 14.8$. This needs to be adjusted.

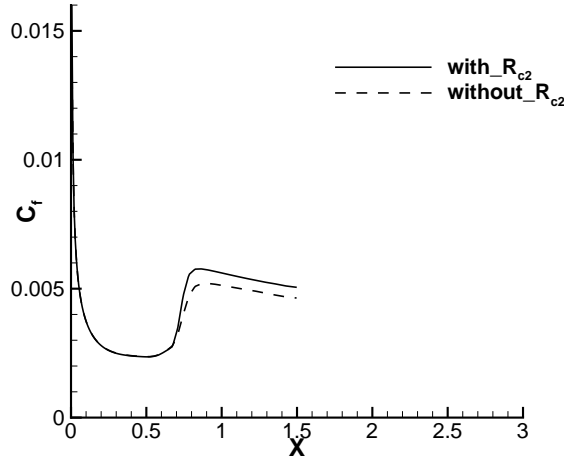


Figure 3.4.3 The effect of R_{c2} . This test case is the same as Figure 3.4.2.

To adjust the active region, the sink term is modified as

$$G_{\gamma-temp1} = 7.5 \max [0, \min (100 - R_\nu, 1)] \times \min [\max (R_\nu - (18 + R_{c2}), 0), 1], \quad (3.4.13)$$

$$R_{c2} = 3.0 \left[\frac{(C_r r)^2 |\Omega|}{2.188 \nu} \right]^{0.8}. \quad (3.4.14)$$

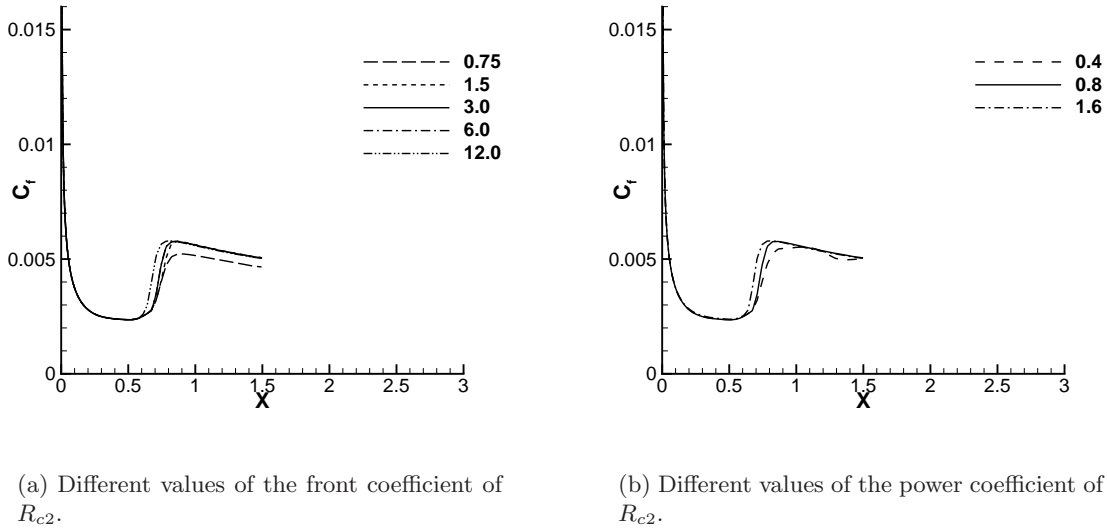


Figure 3.4.4 The effects of coefficients in R_{c2} . This test case is the same as Figure 3.4.2.

This switches off G_γ in the near wall region after transition is complete, thereby making the sink term vanish appropriately. For smooth walls, R_{c2} becomes zero, eliminating the roughness effect. The contribution of R_{c2} is illustrated by Figure 3.4.3. Without R_{c2} , the C_f curve is underestimated due to the existence of sink term in the fully turbulent region. (The C_f curves in Figure 3.4.2 were obtained with R_{c2} included in the sink term.)

The two coefficients – the multiplicative constant and the exponent of R_{c2} – affect the results, as shown in Figure 3.4.4. Figure 3.4.4(a) shows that the results are far less sensitive to the coefficient in R_{c2} than to the key coefficient C_r . As the selected value, 3.0, is halved or doubled, very slight differences are obtained. 4 times the selected value leads to early transition, because the lower bound of R_ν for G_γ is too high and hence the sink term shrinks. 0.25 times the selected value will not shift the transition location, but this provides too small R_{c2} so that C_f is underestimated in the fully turbulence region. Similarly, a larger value of the exponent causes earlier transition, and a lower value makes C_f smaller after transition, as depicted in Figure 3.4.4(b).

Note that the upper bound on R_ν in the function G_γ has not been adjusted so far, because in the fully turbulent region $R_\nu = 100$ generally occurs far away from the wall, where the sink

term is driven to be zero by the factor F_{turb} . But it has to be modified for cases having a strong acceleration, like the region right after the leading edge of a turbine blade. This is explained in the next section.

3.4.3 Modification for Strong Acceleration Flows

In some realistic cases, for example near the leading edge of a turbine blade, flow acceleration can be very large. A strong acceleration causes very large values of $|\Omega|$ in the near wall region (effectively, r^+ becomes large). Consequently, R_ν , defined by Equation (3.4.11), becomes extremely large close to the wall if $r \neq 0$. Then the sink term will vanish right after the stagnation point, because both the factors, F_{turb} and G_γ , of the sink term vanish for large R_ν .

This can be overcome by decreasing R_ν in F_{turb} and increasing the upper bound of R_ν in G_γ . It turns out that the former is more effective. We introduce a revision to R_ν so that F_{turb} will not suppress the sink term in highly strained flow:

$$F_{turb} = e^{-(R_{\nu_{new}} R_t)^{1.2}}, \quad (3.4.15)$$

$$R_{\nu_{new}} = R_\nu e^{-F_Q^{1.5}/350}, \quad (3.4.16)$$

$$F_Q = \max \left[0, \frac{r^2 \sqrt{|Q|} \text{sign}(Q)}{\nu} \right], \quad (3.4.17)$$

where $Q = \Omega_{ij}\Omega_{ij} - S_{ij}S_{ij}$. Q is the difference between the magnitude of the rate of rotation and the rate of strain. For zero pressure gradient flow, Q is zero. For favorable pressure gradient flow, Q is positive, and it is negative in adverse pressure gradients. Based on this property, Q serves to indicate the high acceleration region on a turbine blade. Hence F_Q is non-zero in a favorable pressure gradient and it decreases $R_{\nu_{new}}$.

Without this modification, the sink term would always vanish right after the stagnation point over the suction surface, even for low inflow Reynolds numbers and small roughness: see Figure 3.4.5(a). The modified F_{turb} fixes this quite effectively. Figure 3.4.5(b) shows a reasonable laminar region over the front part of the suction surface.

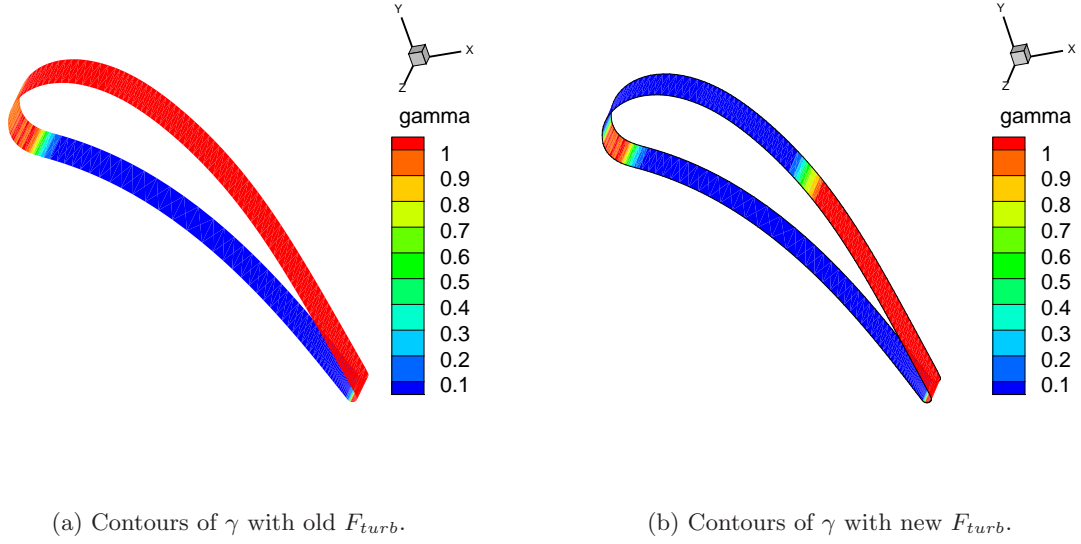


Figure 3.4.5 The effect of the modified F_{turb} . This test case uses the Stripf's turbine, with inflow chord Reynolds number $Re_c = 1.4 \times 10^5$, turbulence intensity at the mid-pitch of the leading edge location $Tu_{l.e.} = 2.7\%$, and roughness height $r = 1.47 \times 10^{-4}m$.

The constants in Equation (3.4.16) were calibrated with the correlation-based model in Boyle and Stripf (2009) for a high pressure turbine blade case which was experimentally tested by Stripf et al. (2005) and Stripf (2007). The quantity $F_Q^{1.5}/350$ is plotted in Figure 3.4.6. It is nonzero only in a very thin region of strong acceleration, on the suction surface. More details about this test case are introduced in the next chapter.

For high roughness, the modified R_ν may exceed the upper bound of 100, in G_γ , even close to the wall. This issue can be solved by increasing this upper bound as follows

$$G_\gamma = 7.5 \max [0, \min ((100 + R_{c3}) - R_\nu, 1)] \times \min [\max (R_\nu - (18 + R_{c2}), 0), 1]. \quad (3.4.18)$$

$$R_{c3} = 0.3 \frac{(d + C_r r)^2 \sqrt{|Q|} \text{sign}(Q)}{\nu},$$

$$R_{c3} = \max [\min (R_{c3}, 100), -100]. \quad (3.4.19)$$

R_{c3} is again a function of Q so that it becomes active in the acceleration region. It uses the effective wall distance instead of the roughness height r ; the aim is to take into account pressure

gradient effects, even for smooth wall cases. Favorable pressure gradients can enhance the sink term and delay the transition. Adverse pressure gradients can suppress the sink term and accelerate the transition. The limiters in Equation (3.4.19) make the modified upper bound of R_ν range between 0 and 200.

The coefficient 0.3 in R_{c3} is calibrated on Stripf's turbine test cases. Its effect on C_f is depicted in Figure 3.4.7. This shows the Nusselt number distribution over the suction surface versus the surface coordinate. When this coefficient is halved the transition is accelerated. When it is doubled, the opposite effect is observed. The selected value, 0.3, gives good agreements with Stripf's data for a wide range of roughness heights, Reynolds numbers and free-stream turbulence intensities.

The modification above for roughness induced transition has been published in [Ge and Durbin \(2015\)](#).

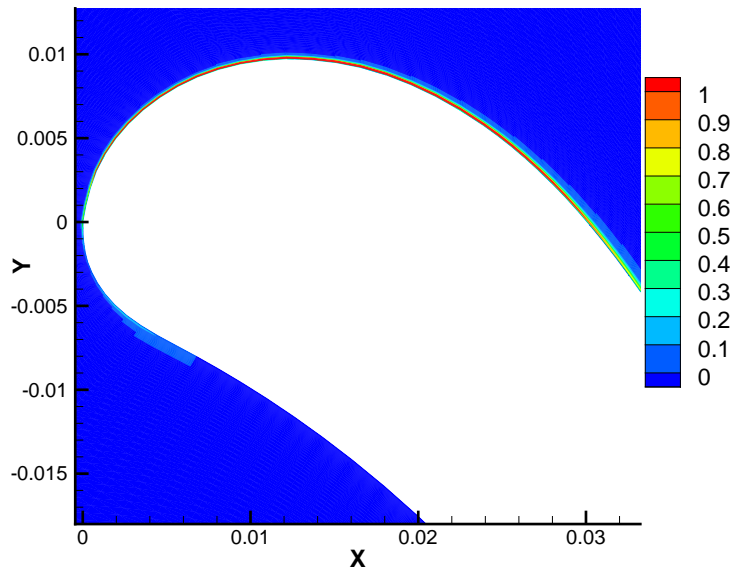


Figure 3.4.6 Contours of quantity $F_Q^{1.5}/350$. This test case is the same as Figure 3.4.5.

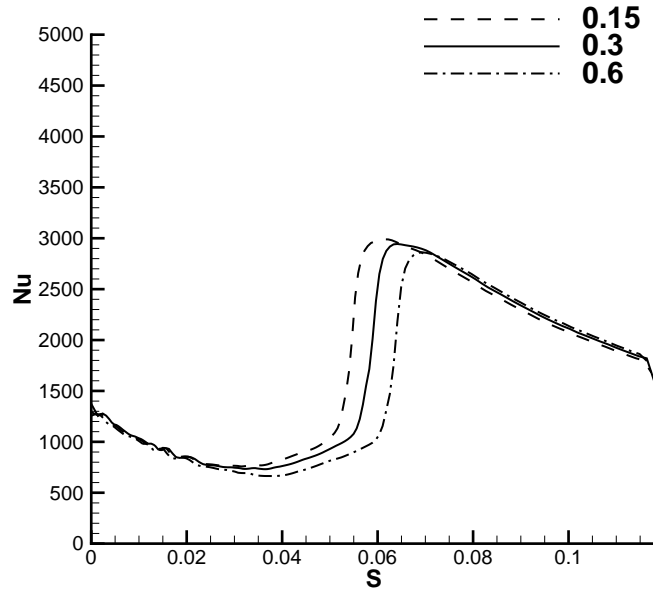


Figure 3.4.7 Effects of the multiplicative coefficient in R_{c3} . This test case uses the Stripf's turbine, with inflow chord Reynolds number $Re_c = 2.5 \times 10^5$, turbulence intensity at the mid-pitch of the leading edge location $Tu_{l.e.} = 1.6\%$, and roughness height $r = 0.73 \times 10^{-4}m$.

CHAPTER 4. COMPUTATION

4.1 Introduction

All cases are computed in OpenFOAM with the current transition model implemented in it. SIMPLEFOAM and PISOFOAM solvers are employed to solve all transport equations involved for steady and transient cases, respectively. CFD codes in OpenFOAM are based on finite volume discretization. Schemes with second order of accuracy are applied in discretization of the spatial and temporal derivatives. Relaxation factors are used in steady cases for convergence.

Section 4.2 is for validation of the transition model for smooth wall cases. Test cases include a flat plate with different Reynolds numbers, various free-stream turbulence intensity Tu , zero or non-zero pressure gradients, and with/without separation, a compressor blade cascade with different Tu , and a flat plate with periodically impinging wakes. Section 4.3 is for validation of the roughness extension. Flat plate cases, and both high and low pressure turbine blade cases, with different Tu , and a wide range of roughness heights are selected for computation. Complex cases are run in parallel at high performance computing platform.

4.2 Smooth Wall Cases

4.2.1 Flat Plate Cases

Test cases in this section are the T3A-C experiments conducted by ERCOFTAC. Cases T3A and T3B have zero stream-wise pressure gradients with different turbulence intensities. Note that another case, T3A-, is not included in the present work. It has low free-stream turbulence intensity (0.9%) (Durbin, 2012). According to the classification of transition in Langtry (2006), it tends to be orderly transition instead of bypass transition. The model in Durbin (2012) works for T3A- in a boundary layer computation, but the current model predicts

early transition for this case. Cases T3C1-5 combine the influences of free-stream turbulence and favorable/adverse pressure gradients imposed by converging/expanding flow channel. The main difference between the various T3C test cases is the free-stream velocity, and hence the Reynolds number (T3C1 is an exception, which has high free-stream turbulence intensity and slow turbulence decay).

Two different domains are used. Both are two dimensional (2D) with only one cell in span-wise direction. One is for the zero pressure gradient test cases (T3A and T3B). It is comprised of a flat plate wall with a length of 1.5 m and a symmetric flat top surface with height of 0.8 m. The inlet surface is at 0.04 m upstream of the plate leading edge to eliminate an ambiguous specification of free-stream conditions. The narrow bottom surface between the inlet and the plate leading edge is set as a symmetric boundary. The inlet boundary has uniformly fixed-value velocity, U_{in} , turbulent kinetic energy, k_{in} , specific dissipation rate, ω_{in} and zero pressure gradient. The outlet boundary has zero-gradient U , k , and ω along with zero pressure (the reference pressure). A grid-independence check is performed, and a mesh of 160 (stream-wise) \times 100 (wall-normal) is found to be sufficient. The first neighbor node to the wall is located at $y^+(1) \approx 1.0$ in the turbulent region. Different values of $y^+(1)$, 0.05, 0.1, 0.5 and 1.0, have been tested for grid convergence check. The results are not notably sensitive when $y^+(1) \leq 1.0$. The wall-normal grid expansion ratio is 1.1, and the stream-wise grid expansion ratio from the leading edge is 1.05, which is consistent with [Langtry \(2006\)](#). The same expansion ratios are adopted for the mesh of T3C cases.

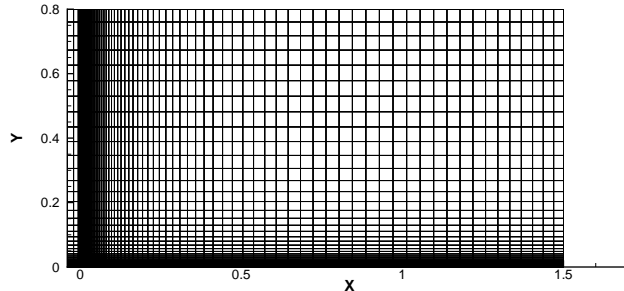


Figure 4.2.1 Mesh used to compute T3A and T3B cases showing every other line in x and y.

The other is for varying pressure gradient test cases (T3C series), which consists of a flat

plate bottom wall with length of 1.65 m and a slip top wall with various height. At the entrance, the gap between the upper and bottom walls is 0.3 m and the height varies along the stream-wise direction corresponding to the experimental data of the pressure gradient variation. The length of bottom surface between the inlet and the leading edge is 0.15 m and again set as a symmetric boundary. Boundary types of inlet and outlet are the same as those of the zero pressure gradient cases. A mesh 230 (stream-wise) \times 125 (wall-normal) is used. The first spacing is set to be $y^+(1) \approx 0.1$ in the turbulent region. Values of $y^+(1) \leq 0.1$ have been used, which turns out that 0.1 is sufficient. For $y^+(1) > 0.5$, noticeable delay of transition will happen. The upper contour is determined by an explicit expression offered in [Suluksna et al. \(2009\)](#). Note that the upper contour of T3C4 is different from the other T3C cases due to a different pressure gradient. Moreover, the length of the plate for T3C4 is 2.00 m, longer than that of other cases, because in this case transition occurs very close to the exit in the experimental data. Extension of the numerical domain guarantees the source term works upstream of the new exit.

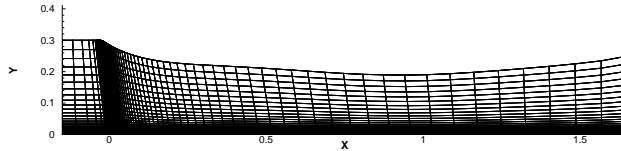
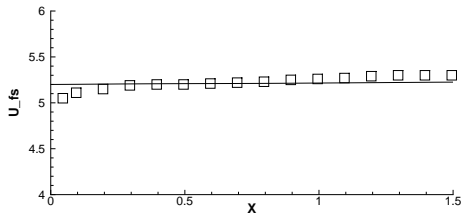


Figure 4.2.2 Mesh used to compute T3C series cases showing every other line in x and y.

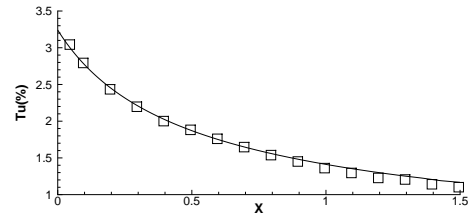
Table 4.2.1 Summary of inlet conditions for flat plate cases.

Case	$U_{in}(m/s)$	$Tu_{in}(\%)$	R_t	$\nu(\times 10^{-5}m^2s^{-1})$
T3A	5.2	3.5	14	1.5
T3B	9.4	6.5	100	1.5
T3C1	6.0	10.0	50	1.5
T3C2	5.0	3.7	12	1.5
T3C3	3.8	3.4	8	1.5
T3C4	1.2	3.5	3.5	1.5
T3C5	8.6	4.3	17	1.5

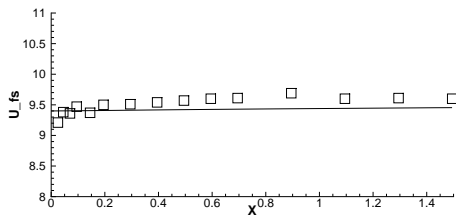
The SIMPLE algorithm for steady flow is applied to solve all the partial differential equations. Numerical discretization of second order accuracy is employed. These numerical setups are used for all the other test cases for the present work. The fluid density ρ and the molecular



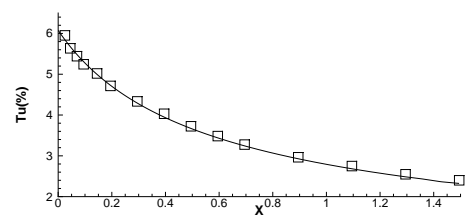
(a) Free-stream velocity in T3A.



(b) Turbulence intensity decay in T3A.



(c) Free-stream velocity in T3B.



(d) Turbulence intensity decay in T3B.

Figure 4.2.3 Free-stream velocity and turbulence intensity in T3A and T3B cases. Experiment data (symbols), simulation results (lines).

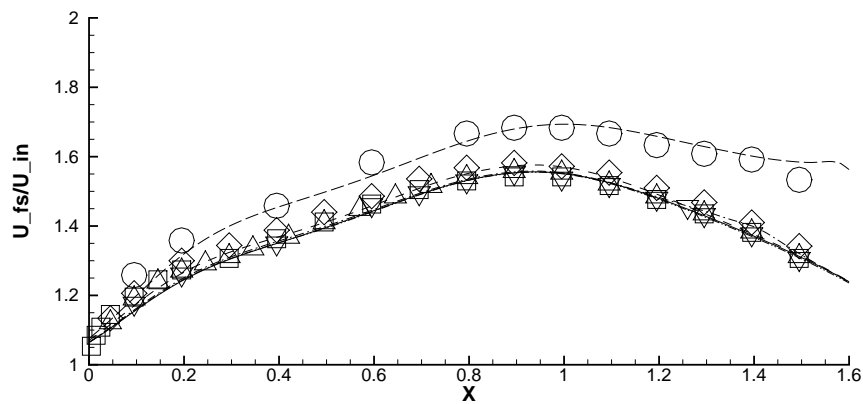
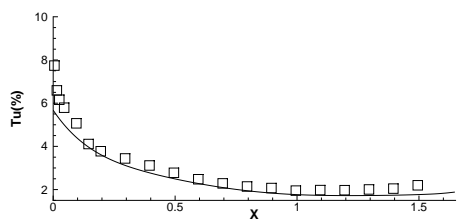
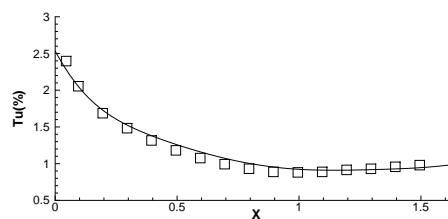


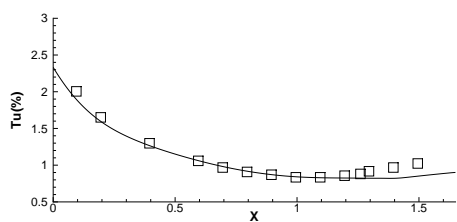
Figure 4.2.4 Normalized free-stream velocity in T3C cases. Experiment data (symbols), simulation results (lines). The circle symbol and long-dash line refer to case T3C4, and the other T3C cases collapse together.



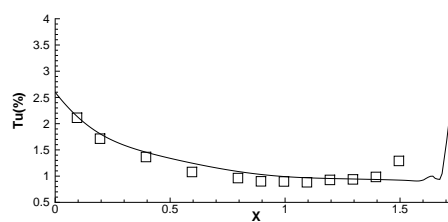
(a) T3C1.



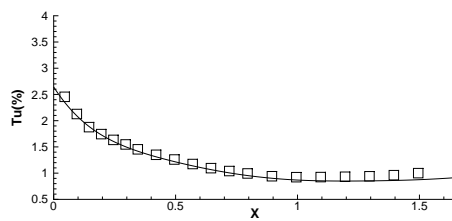
(b) T3C2.



(c) T3C3.



(d) T3C4.



(e) T3C5.

Figure 4.2.5 Free-stream turbulence intensity in T3C cases. Experiment data (symbols), simulation results (lines).

viscosity μ are 1.2 kg/m^3 and $1.8 \times 10^{-5} \text{ kg/m} \cdot \text{s}$, respectively. Then the kinematic viscosity $\nu = \mu/\rho = 1.5 \times 10^{-5} \text{ m}^2\text{s}^{-1}$. The Reynolds number, Re_x , is based on the length from the leading edge and local free-stream velocity. The inlet velocity, U_{in} , is specified to match the data of measured local free-stream velocity through the channel. The inlet turbulent kinetic energy k_{in} can be obtained based on the definition of turbulence intensity. See Equation (4.2.1),

$$Tu_{in} = \frac{\sqrt{2/3k_{in}}}{U_{ref}}, \quad (4.2.1)$$

where U_{ref} equals to U_{in} in zero-pressure-gradient cases, but to local free-stream velocity in varying-pressure-gradient cases. The inlet viscosity ratio, R_t , is used to calculate and specify the inlet specific dissipation rate, ω_{in} ,

$$\omega_{in} = \frac{k_{in}}{R_t\nu}. \quad (4.2.2)$$

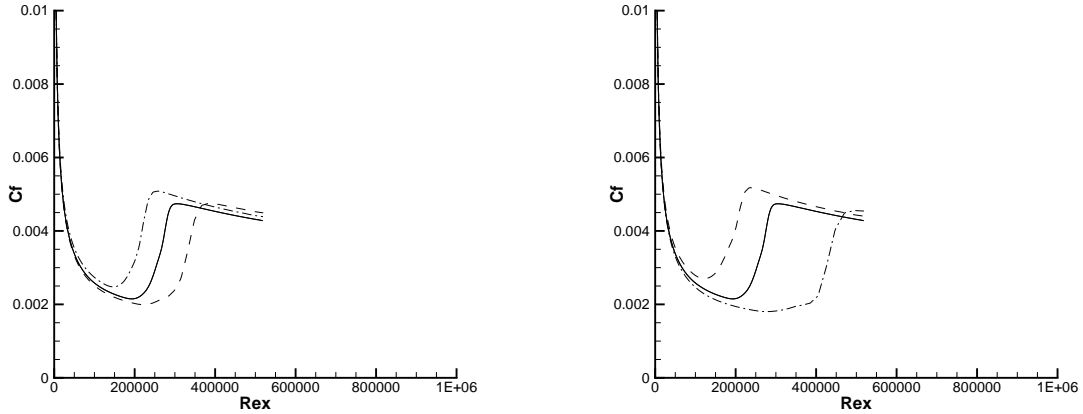
Both Tu_{in} and R_t are determined by agreement with the data for decay of the free-stream turbulence intensity. Figures 4.2.3, 4.2.4 and 4.2.5 show the free-stream velocity and turbulence intensity for the T3 series. Good agreement between simulations and the experimental data has been obtained by using inlet conditions in Table 4.2.1.

There is experimental evidence that both turbulence time-scale and intensity affect bypass transition, i.e. the results are sensitive to the free-stream or inlet conditions. Computations with the current model illustrate this.

Skin friction curves computed with the same inlet dissipation rate (ω_{in}) and with varying turbulence intensity are shown in Figure 4.2.6(a). Note that $k \propto Tu^2$, with other conditions unchanged, the greater the intensity, the greater the kinetic energy. As we can see from the figure, increasing Tu accelerates transition.

Skin friction curves computed with the same $Tu = 3.5\%$ and with different ω_{in} are displayed in (4.2.6.b). Decreasing ω_{in} makes turbulent energy decay slower and increases the eddy viscosity in the free stream. Both effects accelerate transition, and vice versa.

Contours of intermittency function, γ near the wall for zero pressure gradient cases are displayed in Figure 4.2.7(a) and Figure 4.2.7(c) for T3A and T3B cases respectively. Due to



(a) C_f curves for $Tu=3.0$ (dash), $Tu=3.5$ (solid), $Tu=4.0$ (dash-dot).

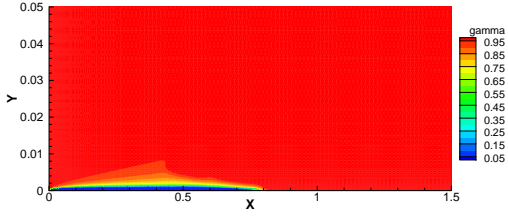
(b) C_f curves for proper ω_{in} times 0.5 (dash), proper ω_{in} (solid), proper ω_{in} times 2 (dash-dot).

Figure 4.2.6 Sensitivity to inlet k and ω (test case: T3A).

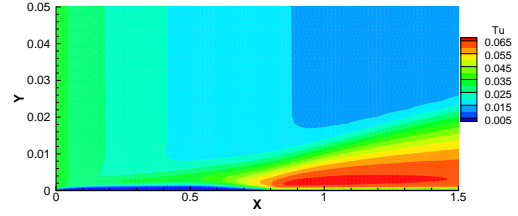
the effect of the sink term, γ rapidly decreases to zero near wall right after the leading edge. With the diffusion of γ from high values inside the free-stream to low values within the laminar boundary layer, transition is initiated, and hence the sink term starts to vanish with the source term switching on. At around the transition location, γ increases to one and the boundary layer becomes turbulent. Figure 4.2.7(b) and (4.2.7.d) present contours of turbulent kinetic energy k . At the transition region, k starts to grow from zero and reaches the turbulent level when transition is complete.

The computed skin friction coefficient for the T3A case is compared with the experimental data in Figure 4.2.8(a). The Blasius laminar boundary layer solution and semi-empirical turbulent boundary layer solution are also plotted. The simulation result is in decent agreement with the measured data. The laminar region is slightly above the data and the transition part of the curve is a little sharper than the data. In the words, the onset location of transition is a bit late and the transition length is therefore short as it reaches the fully turbulent region on time. This issue exists in all the other T3 cases.

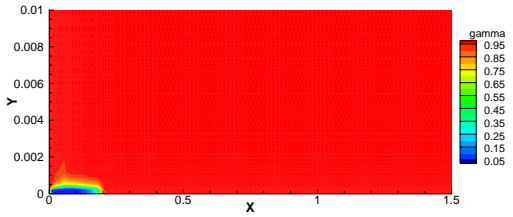
The computed skin friction coefficient for T3B is compared with the experimental data in



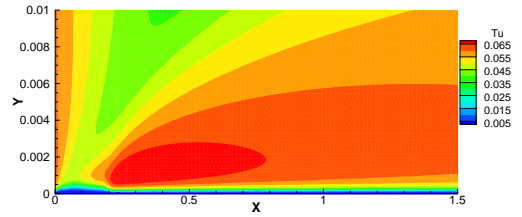
(a) Contours of γ for T3A (zoom into the boundary layer).



(b) Contours of turbulence intensity for T3A (zoom into the boundary layer).



(c) Contours of γ for T3B (zoom into the boundary layer).



(d) Contours of turbulence intensity for T3B (zoom into the boundary layer).

Figure 4.2.7 Contours of intermittency function and turbulence intensity for T3A and T3B.

Figure 4.2.8(b). Due to the high turbulence intensity, the skin friction before the completion of transition is over-predicted. But it does make an improvement compared with results in [Langtry and Menter \(2009\)](#). The minimum skin friction obtained by the current model is close to 0.004 while results of other models are just around 0.005.

The T3C test cases can be classified into two groups. T3C1 is a high free-stream turbulence level case (first data point with $Tu \approx 8.0\%$), and the other T3C cases are moderate free-stream turbulence level cases (first data point with $Tu \approx 2.5\%$).

Like the case T3B, with high free-stream turbulence intensity, the skin friction for T3C1 shown in Figure 4.2.9(a) is better than the result of [Suluksna et al. \(2009\)](#). The smallest skin friction is closer to the experimental data.

The results for T3C2 are shown in Figure 4.2.9(b). In this case, the transition occurs in the adverse pressure gradient region because of the low Reynolds number. The onset location of transition is a bit late. But as mentioned above, the fast transition makes it up and meets

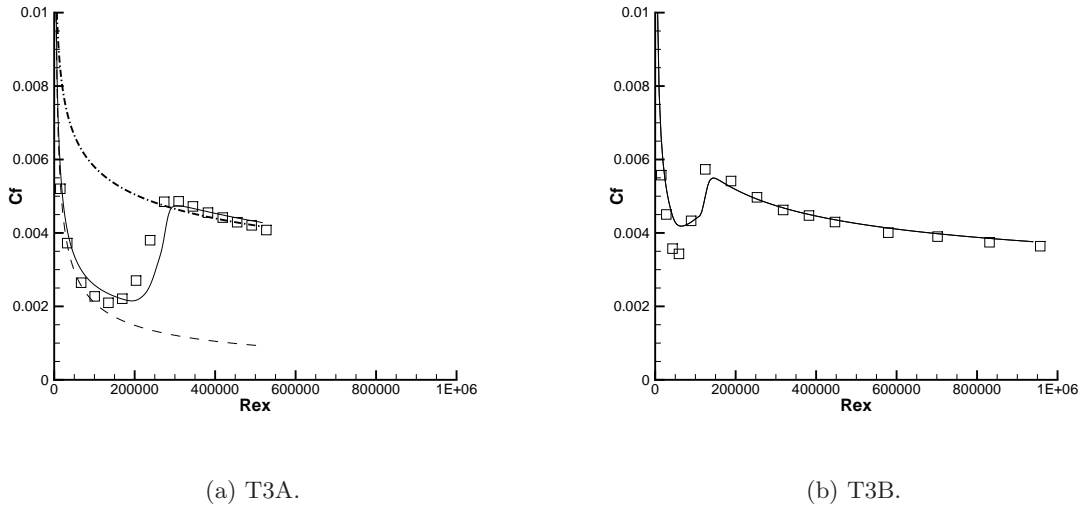


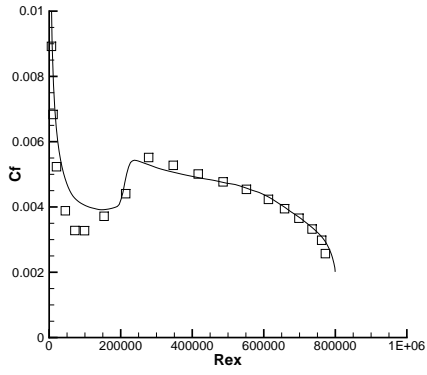
Figure 4.2.8 Skin friction for T3A and T3B. Experimental (symbols), laminar (dash), turbulent (dash-dot), simulation (solid).

the turbulent region at almost the same Reynolds number as measured.

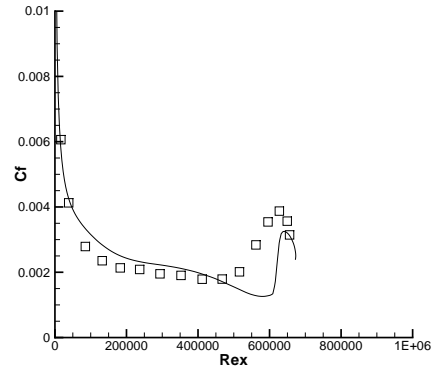
The case T3C3 has even later transition than T3C2 as displayed in Figure 4.2.9(c), because its Reynolds number is smaller and the turbulence decay is faster than T3C2. In addition, it is getting closer to separation. Both of these are predicted by the current model with acceptable agreement with the data though late transition is predicted again.

T3C4 is regarded as a benchmark for separation-induced transition in Langtry and Menter (2009) and Suluksna et al. (2009). However, the onset location of transition is very close to the exit according to the experimental data, which has only one data point after transition. Another problem is that the data shows a very tiny separation region. Even if this case may not be proper to test a model for transitional separated flow due to these two drawbacks, Figure 4.2.9(d) still shows that the current model is able to predict the transition and reattachment after flow separates with an acceptable error compared with the data. Another case of flat plate separated flow from Lardeau et al. (2012) is invoked to test the separation modification to the basic model as discussed in Section (4.2.2).

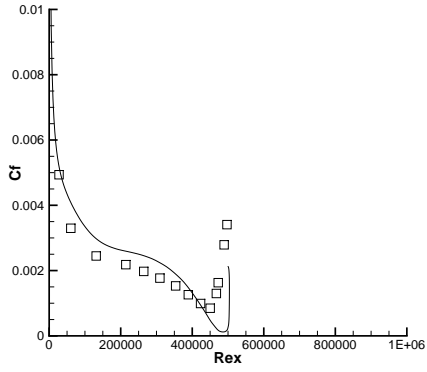
Figure 4.2.9(e) presents the skin friction coefficient computed by the current model for the T3C5 case. Transition occurs before the throat of the flow channel, i.e. within the favorable



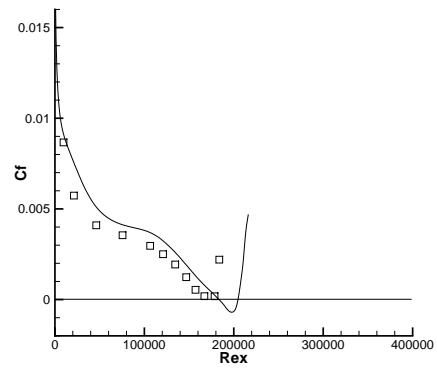
(a) T3C1.



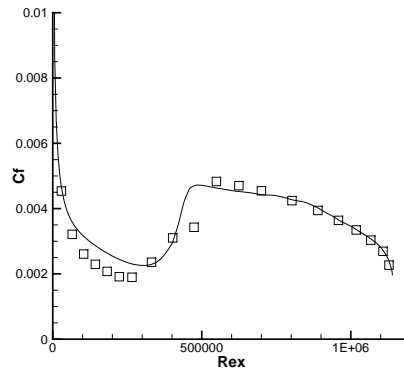
(b) T3C2.



(c) T3C3.



(d) T3C4.



(e) T3C5.

Figure 4.2.9 Skin friction for T3C cases. Experiment data (symbols), simulation results (lines).

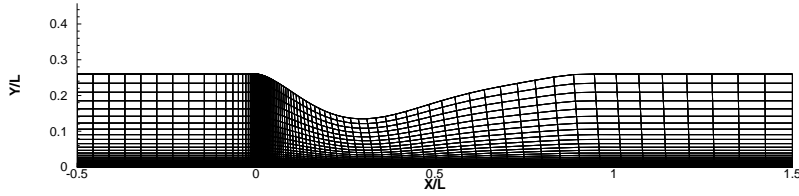


Figure 4.2.10 Mesh for flat plate separated flow case showing every other line in x and y .

pressure gradient region since the inlet velocity and therefore the Reynolds number is high. Because of the strong favorable pressure gradient the transition length is extended to some extent. The model approximately predicts the behavior with small difference from the experimental data.

4.2.2 A Flat Plate Separated Flow

This test case was firstly studied experimentally by [Lou and Hourmouziadis \(2000\)](#), and numerically by [Wissink and Rodi \(2006b\)](#) based on DNS and by [Lardeau et al. \(2012\)](#) based on LES. The current model is able to predict locations of transition and reattachment with decent accuracy compared to the LES data of [Lardeau et al. \(2012\)](#). The inlet is set half of the "chord" length L upstream of the leading edge. But the plate length in the present work is extended to the computational exit, $X/L = 1.5$, in order to allow a fully turbulent region downstream and uniform pressure profile at the exit. For simplicity, X/L is replaced with X in the following plots. The contour of the upper wall is exactly as [Lardeau et al. \(2012\)](#). The bottom surface from the inlet to the leading edge is specified as a symmetric boundary, and after the leading edge, it is a non-slip wall boundary to the outlet. The whole top surface is a slip wall boundary. Uniform profiles for U_{in} , k_{in} and ω_{in} are specified at the inlet. The Reynolds number, based on the chord length L and the inflow velocity U_{in} is 60,000. k_{in} and ω_{in} are again determined to match the decay of the free-stream turbulence intensity of the LES data. At the outlet, zero pressure gradient is used for most of the variables except p with uniform zero value. The 2D mesh for this case in [Figure 4.2.10](#) is 200 (stream-wise) \times 80 (wall-normal), with first grid spacing $y^+(1) \approx 0.1$ in the turbulent region. A mesh finer than this has little effect on the results.

Two simulations with different free-stream turbulence intensities are performed. The higher the free-stream turbulence intensity is, the earlier the transition and reattachment will be. Details about the inlet conditions are listed in Table 4.2.2. Figure 4.2.11 shows the free-stream turbulence intensity distributions for these two simulations. The reference velocity to define Tu is the local free-stream velocity. Though the inlet Tu is different from the LES data, the present simulations reproduce very similar levels of Tu after the leading edge where $X = 0$.

Table 4.2.2 Summary of inlet conditions for the flat plate separated flow case.

Case	$U_{in}(m/s)$	$Tu_{in}(\%)$	$\omega_{in}(s^{-1})$	$\nu(\times 10^{-5}m^2s^{-1})$
Simulation 1	0.9	5.8	90	1.5
Simulation 2	0.9	7.5	60	1.5

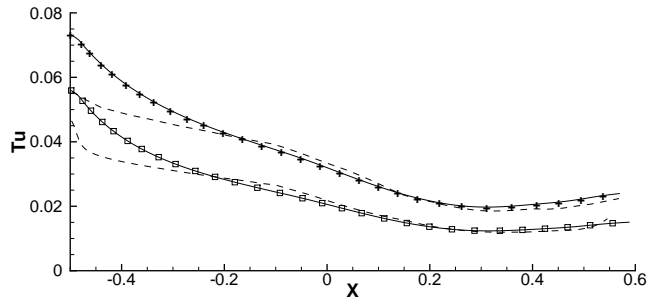
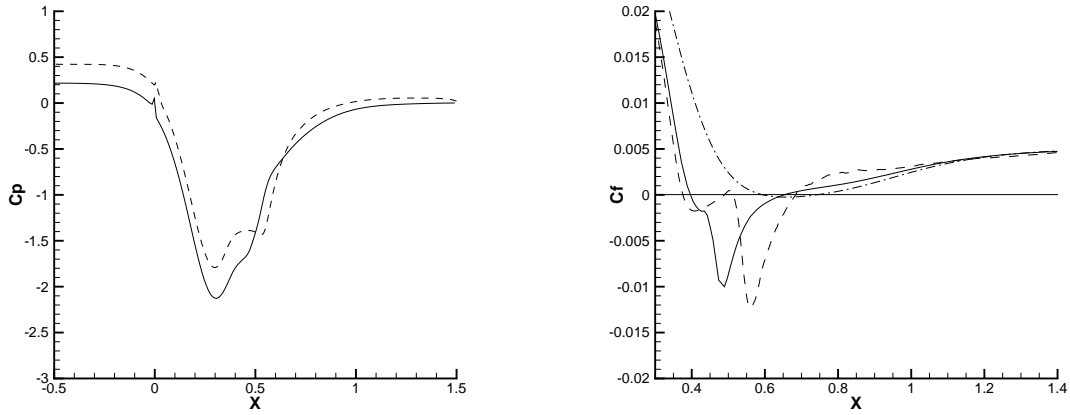


Figure 4.2.11 Distributions of free-stream turbulence intensity for the flat plate separated flow case. “Simulation 1” (\square), “Simulation 2” ($+$); current model (solid), LES by Lardeau et al. (2012) (dash).

The pressure distribution and skin friction on the wall for Simulation 1 are displayed in Figure 4.2.12. The reference pressure is the exit pressure, and the reference velocity is simply U_{in} for both C_p and C_f . There should be a sudden increase of pressure and a pressure plateau in the separated region, but the current model does not predict the plateau very clearly. And also the smallest pressure is underestimated by the model. The level of C_f at the beginning of the turbulent region is under-predicted, but this is attributed to the $k - \omega$ model. The intermittency model transits to full turbulence after the flow reattaches, but the $k - \omega$ model itself cannot predict the correct level of C_f in the turbulent region.

The location of separation and reattachment simulated by the current model is relatively



(a) Pressure coefficient.

(b) Skin friction.

Figure 4.2.12 Plots for Simulation 1. Current model (solid), LES by [Lardeau et al. \(2012\)](#) (dash), $k-\omega$ model (dash-dot).

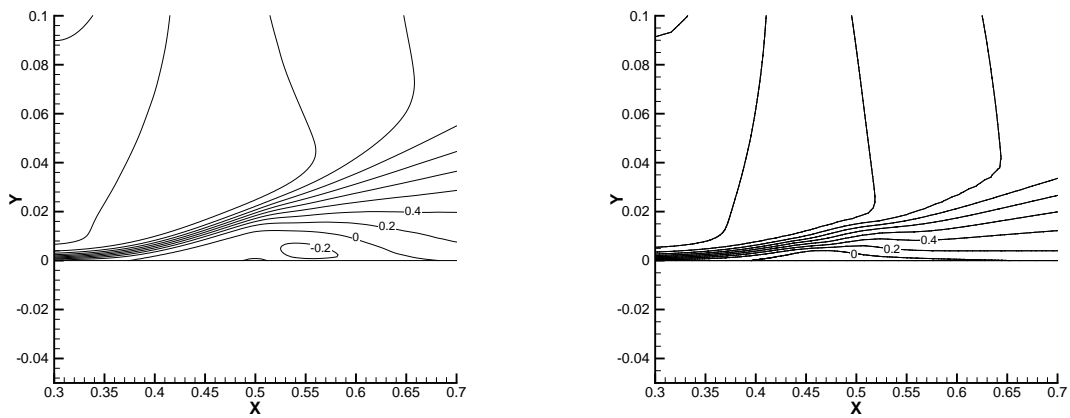
(a) Contours of U_x by [Lardeau et al. \(2012\)](#) based on LES.(b) Contours of U_x by current model.

Figure 4.2.13 Contours of stream-wise velocity around the separation bubble for Simulation 1.

accurate, though the transition occurs a bit early. This again leads to the observation that the nature of transition of separated boundary layer is different from the bypass transition. The former has an inflection point but the latter does not. It is difficult to simulate such a complicated case very accurately by using a simple RANS model since the transition in this case may be induced by various mechanisms. However, the current model is a considerable improvement on the original $k - \omega$ RANS model, which is shown in Figure 4.2.12(b).

Figure 4.2.13 depicts the contours of stream-wise mean velocity computed both by LES and the current model. The separation bubble produced by the model is thinner than that of LES.

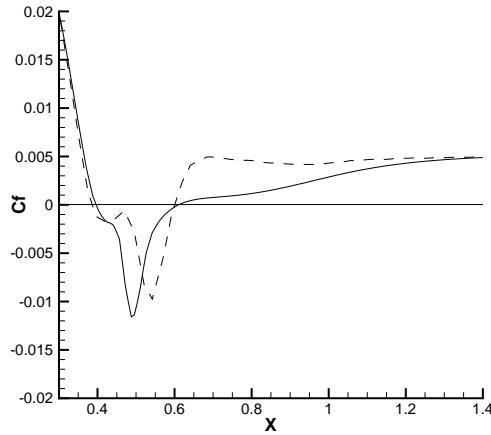


Figure 4.2.14 Skin friction for Simulation 2. Current model (solid), LES by [Lardeau et al. \(2012\)](#) (dash).

The skin friction coefficient of Simulation 2 is plotted in Figure 4.2.14. Similar to simulation 1, the model predicts the locations of separation and reattachment with good agreement with the LES data, but the transition location and the turbulence level are not accurate. In addition, comparing the results shown both in Figure 4.2.12(b) and 4.2.14, the difference between the two C_f curves of the model is slight, whereas that of the LES data is noticeable. This means that the results based on the model are not sensitive to the free-stream turbulence intensity except for an earlier reattachment in Simulation 2 which has higher free-stream Tu .

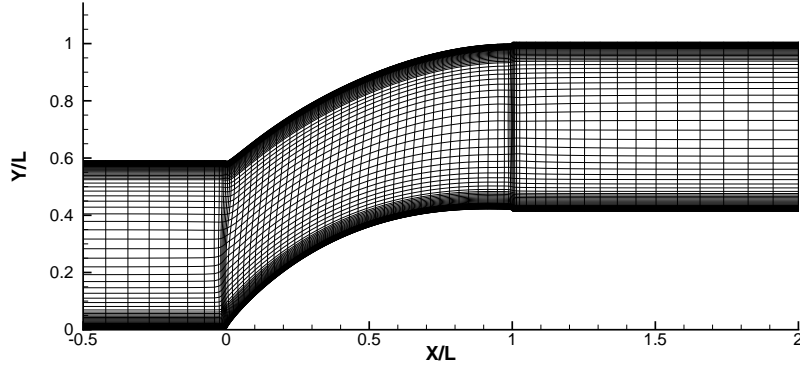


Figure 4.2.15 Mesh for compressor blade cascade case showing every third line in x and y.

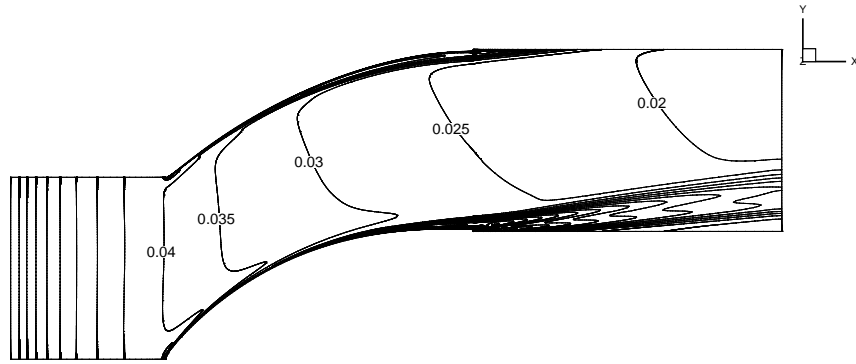
4.2.3 A Compressor Blade Cascade

In this section, a 2D flow through a V103 low pressure compressor blade passage with two different free-stream turbulence intensities is simulated by the current model and the results are compared with the DNS data in [Zaki et al. \(2010\)](#).

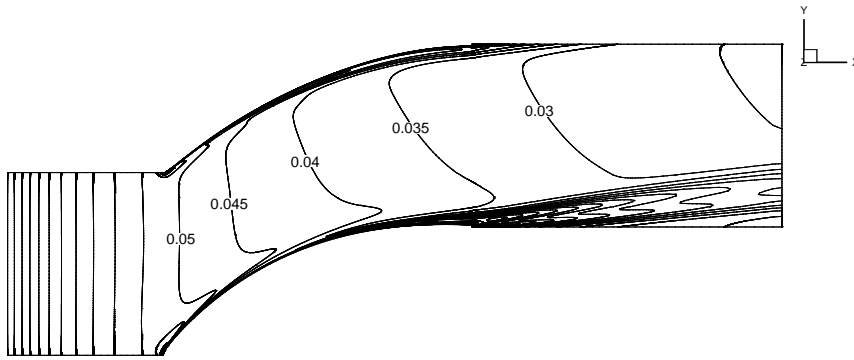
Table 4.2.3 Summary of inlet conditions for the compressor blade cascade case.

Case	$U_{in}(m/s)$	$Tu_{in}(\%)$	$\omega_{in}(s^{-1})$	$\nu(\times 10^{-5}m^2s^{-1})$
Simulation 1	2.0775	9.0	130	1.5
Simulation 2	2.0775	11.0	100	1.5

The computational domain with the grid is shown in Figure 4.2.15. The coordinates of the blade are based on a NACA 65 airfoil ([Zaki et al., 2010](#)). The mesh is 223 (stream-wise) \times 286 (wall-normal) with the first grid spacing $y^+(1)$ ranging between 0.1 and 1.0. To simulate the compressor blade cascade, periodic boundary conditions upstream and downstream of the blade surface are used. The periodic surfaces are specified at $X/L < 0$ and $X/L > 1$, where the axial chord L is selected as the reference length scale. A non-slip boundary condition is applied on the blade surfaces. The blade pitch, i.e. the height of the inlet and outlet is $P = 0.59L$. The inlet is located at $X/L = -0.5$, and the outlet is extended to $X/L = 2$. For simplicity, X/L is denoted as X below. At the inlet boundary, uniform U_{in} , k_{in} and ω_{in} are specified to produce the desired free-stream mean velocity and turbulence decay. The angle between the inlet mean velocity vector and the horizontal axis is $\alpha = 42^\circ$. The Reynolds number based on



(a) Simulation 1.



(b) Simulation 2.

Figure 4.2.16 Contours of turbulence intensity for both simulations.

U_{in} and L is 138,500. The outlet boundary condition is the same as the other cases described above.

In Table 4.2.3 are values of variables at the inlet for both simulations. And the corresponding contours of the turbulence intensity are displayed in Figure 4.2.16. These are similar to the distributions of Tu obtained by Zaki et al. (2010). The values of Tu at the mid-pitch follows the DNS data from the leading edge to the trailing edge, which reproduces the same free-stream turbulence intensity as Cases T2 and T3 in Zaki et al. (2010). Pressure coefficient and skin friction on the surfaces of the blade are plotted in Figure 4.2.17 and 4.2.18 for both simulations.

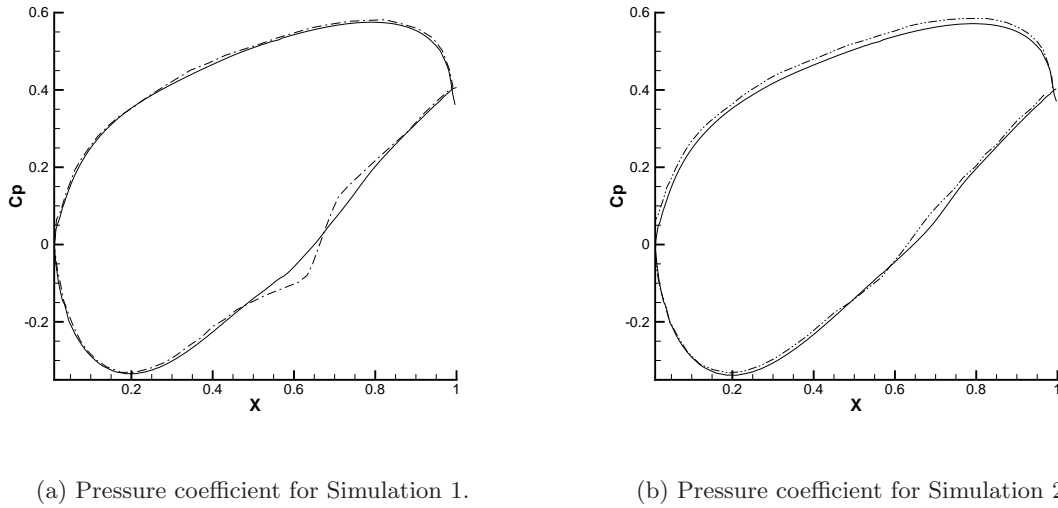


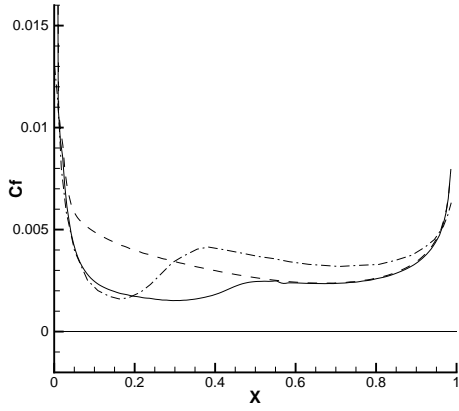
Figure 4.2.17 Pressure coefficient of the compressor blade case. Current model (solid), DNS (dash-dot for Simulation 1, dash-dot-dot for simulation 2).

The reference pressure is at the leading edge and the reference velocity is U_{in} . Contours of γ on the blade surfaces and separation bubbles over the suction sides for both simulations are depicted in Figure 4.2.19.

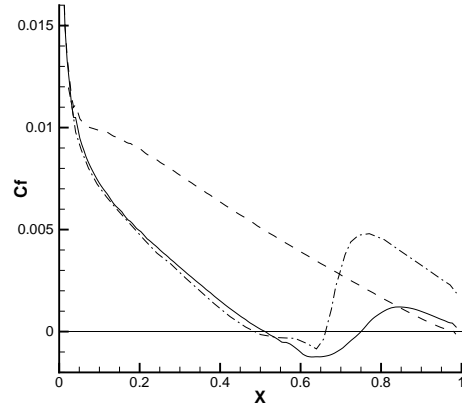
In the separated region of Simulation 1, the model does not produce an obvious pressure plateau and then a sudden pressure rise as the DNS data on the suction surface, though the negative skin friction by the model extends farther than the DNS. The onsets of transition are later and the lengths of transition are longer than DNS data on both surfaces.

The most significant issue for Simulation 2 is the unphysically separated region on the suction surface predicted by the current model (Figure 4.2.18(d) and 4.2.19(d)). The transition occurs too late to keep the flow attached. Note that transition on the suction surface occurs in an adverse pressure gradient region, which tends to cause late transition by the current model (see Section (4.2.1) about T3C cases). On the pressure side, the location and length of transition appear close to the DNS data, whereas the level of the skin friction is higher in the laminar region.

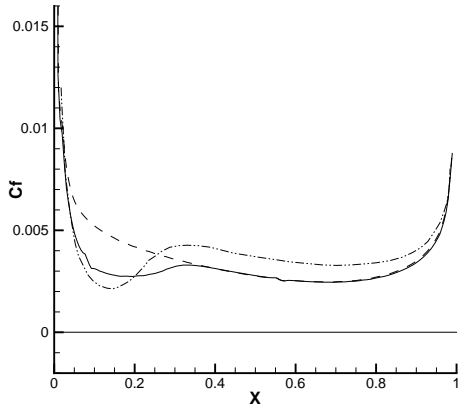
With higher free-stream turbulence intensity, transition occurs earlier and the length of transition becomes shorter, which illustrates that the current model is able to predict the



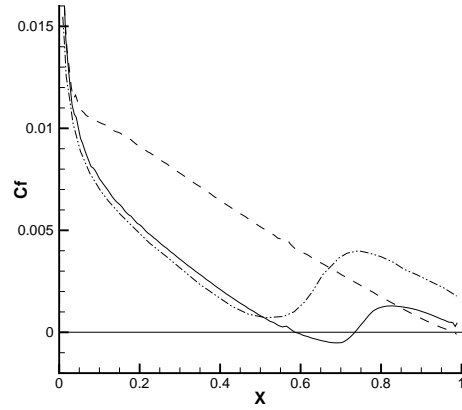
(a) Skin friction on the pressure side for Simulation 1.



(b) Skin friction on the suction side for Simulation 1.

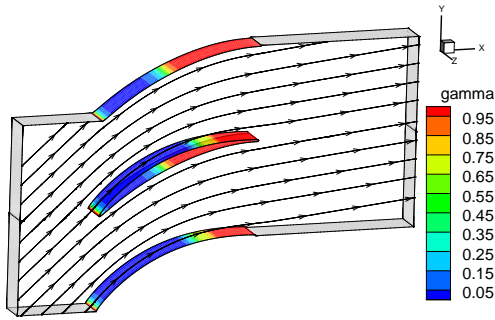


(c) Skin friction on the pressure side for Simulation 2.

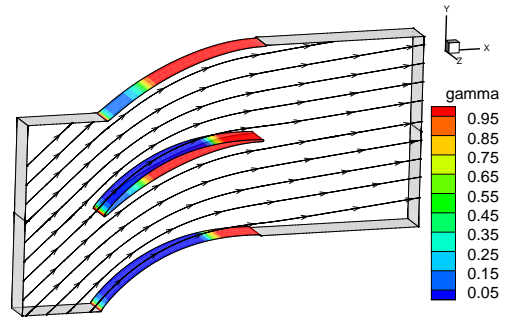


(d) Skin friction on the suction side for Simulation 2.

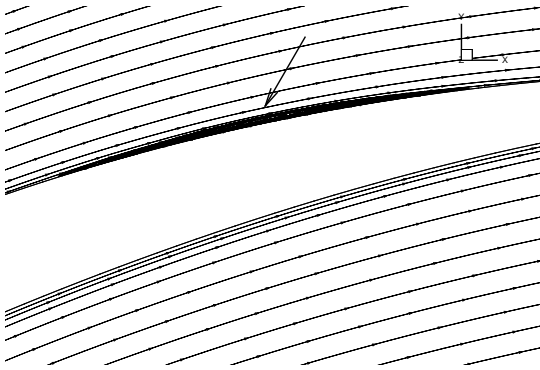
Figure 4.2.18 Skin friction of the compressor blade case. Current model (solid), $k - \omega$ RANS model (dash), DNS (dash-dot for Simulation 1, dash-dot-dot for simulation 2).



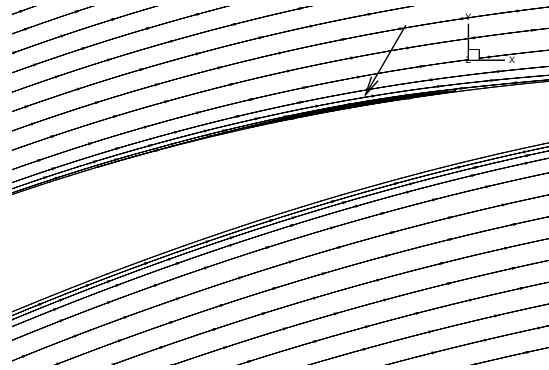
(a) Contours of γ on the blade surfaces along with streamlines for Simulation 1.



(b) Contours of γ on the blade surfaces along with streamlines for Simulation 2.



(c) The separation bubble over the suction surface for Simulation 1.



(d) The separation bubble over the suction surface for Simulation 2.

Figure 4.2.19 Contours of γ and separation bubbles of the compressor blade cases.

sensitivity to the free-stream turbulence intensity for this case.

In both simulations, the turbulent levels are lower than the DNS data. But again this is caused by the original turbulence model as can be seen in the figures. After the transition, the computations shifts to pure $k - \omega$ and C_f reaches the identical turbulent level predicted by the $k - \omega$ model. One can infer that the current model for bypass transition may work fine if the $k - \omega$ RANS model were able to predict the fully turbulent region of this flow more accurately. In other words, benefit is indeed gained when this intermittency model is applied to the $k - \omega$ model even for such a challenging case.

4.2.4 Periodic Wakes Impinging on a Flat Plate

Figure 4.2.20 shows the layouts of a experiment and a simulation for turbulent wake swept across a flat plate boundary layer. These setups mimic the phenomenon of wake-induced transition occurring within an intermediate stage of a turbomachine. Recall Figure 2.2.4. Benchmark data from DNS of this test case (Wu et al., 1999) was presented and compared with the RANS solutions in Wu and Durbin (2000). Again, this benchmark test case is simulated by using the proposed transition model and the results along with a small subset of the DNS data will be presented below.

In the experiment of Liu and Rodi (1991), a squirrel cage of cylinders produced an extra wake on the upstream of the leading edge. There is a difficulty in the experiment on the quantification of space-time, phase-averaged statistics, i.e. one wants $\langle f \rangle (x, y, 2\pi\phi)$. Here angle brackets denote a phase average, f is the variable of interest, and ϕ is the phase of the periodic wake passing. This technical problem can be overcome by DNS, in which a wealth of data can be generated. In the DNS of Wu et al. (1999), the turbulent wake velocities were generated from a separate precomputation on a temporally decaying, self-similar plane wake, and then superimposed to a Blasius profile at the domain inlet. Variables with respect to the wake-coordinate system should be transformed to the flow domain coordinate system with respect to the wake inclination angle $\alpha = \tan^{-1}(U_{cyl}/U_{ref})$. See Figure 4.2.20.

In the RANS computation by Wu and Durbin (2000), self-similar wake profiles are translating periodically across the entrance to the flow domain superimposed onto a Blasius boundary

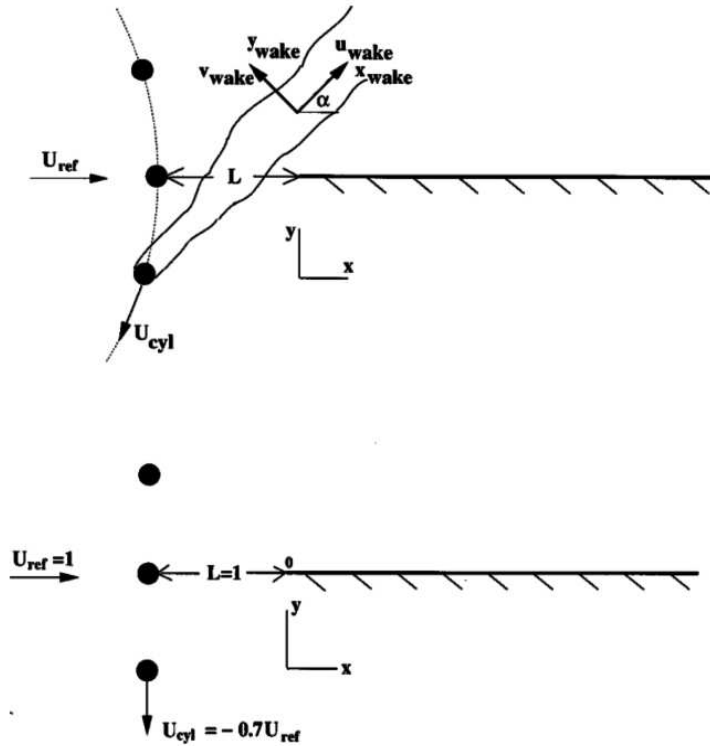


Figure 4.2.20 The upper: schematic of the experiments of [Liu and Rodi \(1991\)](#); the lower: schematic of the simulation of [Wu and Durbin \(2000\)](#).

layer profile with $Re_\theta = 80$. The flow domain is a rectangle, $0.1 \leq x \leq 3.5$, $0 \leq y \leq 0.8$ in dimensionless units. The characteristic length scale is the distance between the cylinder translating trajectory and the leading edge, $L = 1$. See the lower portion of Figure 4.2.20. The leading edge is at $x = 0$. The Reynolds number $Re = U_{ref}L/\nu = 1.5 \times 10^5$, where $U_{ref} = 1$ is the inlet reference velocity. The wakes' half-width b is 0.1 and the centerline deficit velocity U_{def} is 0.14 at the inlet $x = 0.1$, scaled by U_{ref} . The only difference for the flow setup between the current simulation and [Wu and Durbin \(2000\)](#) is the inlet location. The new domain entrance is at $x = -0.05$ and the leading edge is included within the domain, similar to the flat plate cases in Section 4.2.1. Though in this case no Blasius profiles are needed at the new inlet, proper wake profiles for U , k and ω should be specified such that the corresponding profiles at $x = 0.1$ closely match the profiles of [Wu and Durbin \(2000\)](#), with $U_{def} \approx 0.14$ and $b \approx 0.1$. See Figure 4.2.21. U_{def} and b at $x = -0.05$ are finally chosen 0.48 and 0.03, respectively.

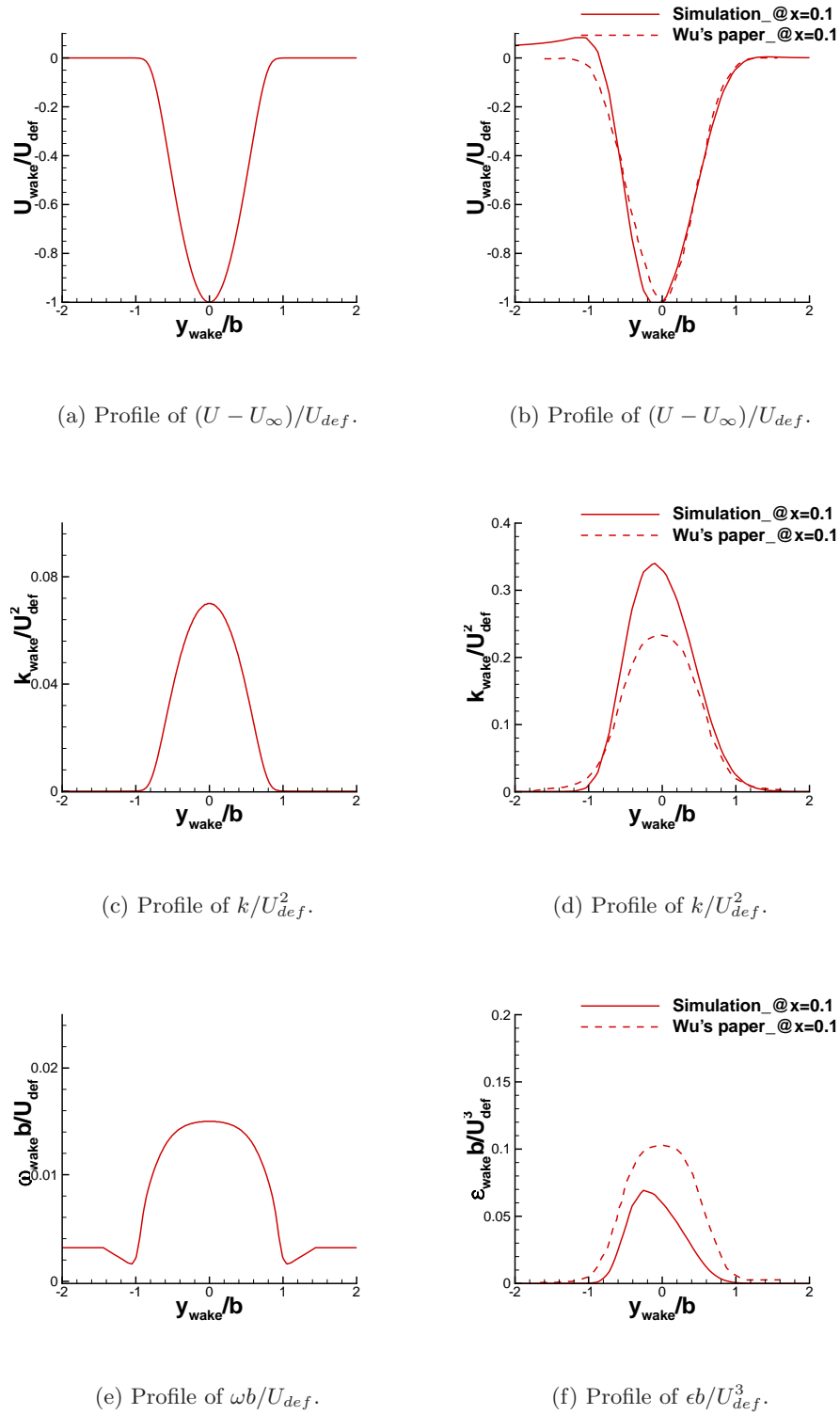
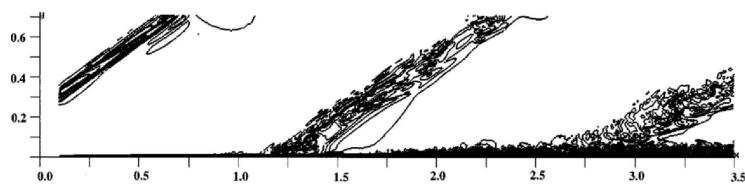


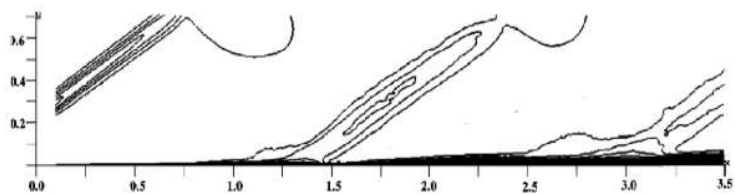
Figure 4.2.21 Dimensionless profiles of the wake at $x = -0.05$ (left column) and $x = 0.1$ (right column), where the wake halfwidth $b = 0.03$ and 0.1 , and deficit velocity $U_{def} = 0.48$ and 0.14 , respectively. The data from [Wu and Durbin \(2000\)](#) are denoted by dash lines and used for generation of their inlet profiles.

The wake passing period is $T = 1.67$, and hence the distance between wake centers is $1.67 \times 0.7 = 1.17$, which is 11.7 times their half-width at $x = 0.1$. In this case wakes remain well separated. Unsteady RANS computations with the proposed transition model are performed on a 211×101 grid in streamwise and wall normal direction with 10 grid points in the pre-leading-edge region and 201 grid points along the flat plate. The wall normal space is stretched in y with $y^+(1) \approx 1$. In x direction, grid is refined around the leading edge and nearly uniform further downstream.

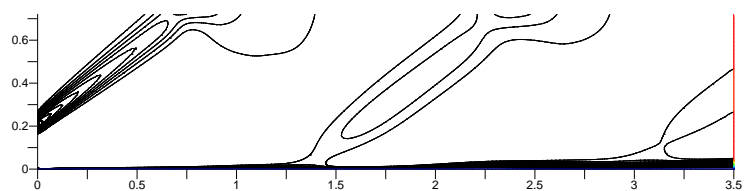
Figure 4.2.22 depicts three sets of contours: the instantaneous streamwise velocity \tilde{u} from DNS data in Wu et al. (1999); the phase-averaged stream velocity $\langle \tilde{u} \rangle$ of the DNS data; and the result from the unsteady RANS simulation using the current transition model. One can observe that the boundary layer is laminar for $x < 1$ and turbulent for $x > 1.5$ where the boundary layer becomes thick. The thickening beneath the wake is also observed, which is the forced response of the buffeted laminar boundary layer to the passing wakes. From the contours of the RANS simulation, one can observe the growth of the wake width and the damping of the wake deficit velocity are faster than the DNS data. This is caused by relative higher k at location $x = 0.1$ obtained in the RANS simulation than the DNS. See Figure 4.2.21(d). The higher the turbulence level, the more mixing and spreading of the wake to the free stream. The first criterion of choosing values of k and ω in the wake profiles at the actual inlet $x = -0.05$ was to obtain correct U_{def} and b at $x = 0.1$ (Figure 4.2.21(b)). Velocity contours in the RANS simulation appear nonphysical near the top boundary due to the symmetry boundary condition used, but this would not impact the solution near the flat plate.



(a) Instantaneous streamwise velocity at $t = 32.5T$ from DNS of Wu et al. (1999).



(b) Phase-averaged streamwise velocity at $\phi = 0.5$ from DNS of Wu et al. (1999).



(c) Phase-averaged streamwise velocity at $\phi = 0.5$ from the unsteady RANS using the proposed model.

Figure 4.2.22 Comparison of contours of streamwise velocity between the DNS and present simulation.

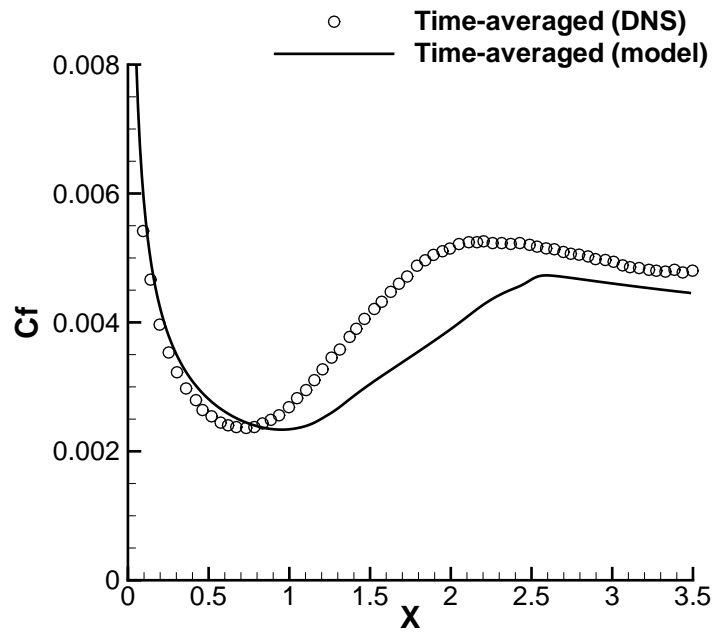
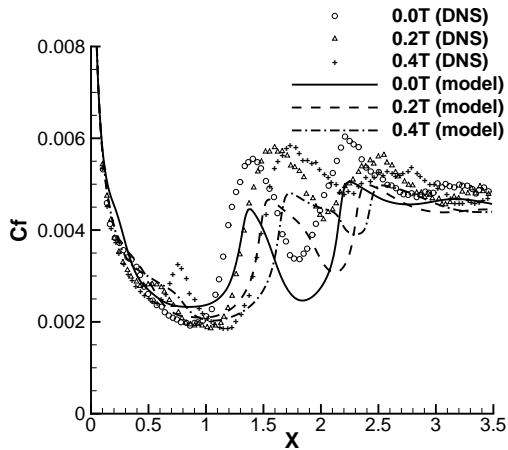
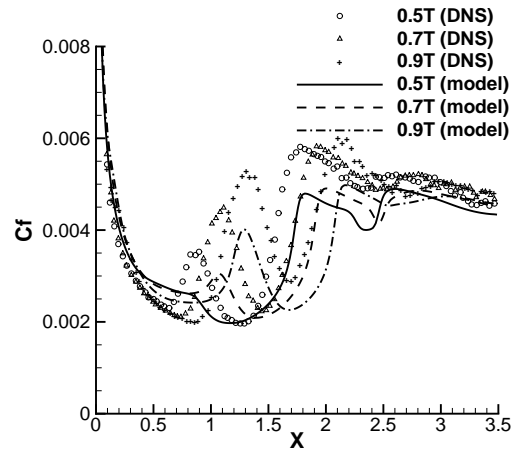


Figure 4.2.23 Time-averaged mean C_f curves. Symbols: DNS of Wu et al. (1999); lines: present model.

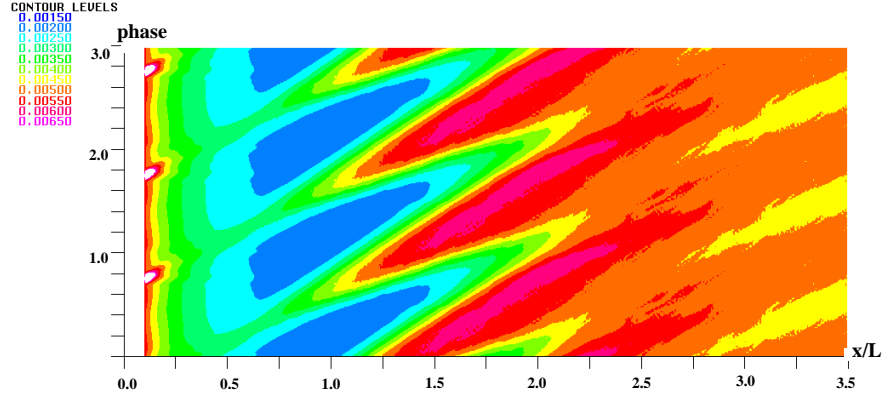


(a) C_f curves at $0.0T$, $0.2T$ and $0.4T$.

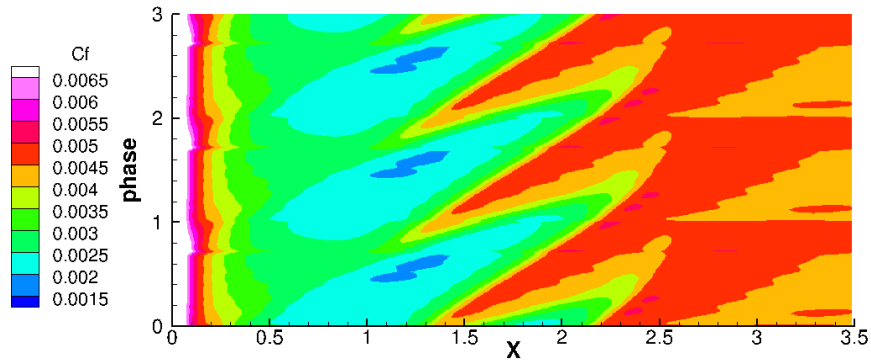


(b) C_f curves at $0.5T$, $0.7T$ and $0.9T$.

Figure 4.2.24 Phase-averaged mean C_f curves. Symbols: DNS of Wu et al. (1999); lines: present model.



(a) DNS of Wu et al. (1999).



(b) Present model.

Figure 4.2.25 X-phase diagram of the phase-averaged mean C_f . The contour levels are from 0.0015 to 0.0065 with an increment of 0.0005.

Figure 4.2.24 shows the phase-averaged C_f curves at instant $\phi = 0.0, 0.2$, and 0.4 in part (a), and at $\phi = 0.5, 0.7$, and 0.9 in part (b). A typical $\langle C_f \rangle$ curve at an instant perturbed by the wakes, say $\phi = 0$, cuts across the buffeted laminar region, switches into the turbulent region, intersects a path of perturbed laminar flow, and finally traverses the downstream turbulent region. Bell-shaped upward protrusions upstream of $x = 2.0$ are the footprint of the passing wakes. They progress downstream, becoming increasingly noticeable. In a frame of reference moving with a wake, it looks that the peak of a protrusion grows due to extended forcing of

the buffeted laminar layer, and is different from the bifurcation to turbulence. This feature is predicted by both DNS and RANS simulations. When $x > 2.0$, the flow is almost self-sustained turbulent, although perturbations by the wakes still exist.

Space-time fields, $\langle C_f \rangle (x, \phi)$ are displayed in Figure 4.2.25. C_f curves along the plate at an instant are horizontal sections across the contour plot. DNS data are present in part (a), and the RANS results by using the proposed model are in part (b). The transition region shifts periodically as wakes pass across the inlet. The tongue-shaped protrusions in both C_f contours (blue patches) are areas in which the laminar skin friction is highly disturbed by the wakes. This is well predicted by the current transition model.

The contour levels downstream of transition are underestimated by the model compared with the overshoot C_f in the DNS data. This is a common drawback of RANS simulations. The time-averaged C_f plotted in Figure 4.2.23 also presents this feature. Slightly late transition predicted by the current model is observed both in 4.2.25 and 4.2.23 compared to the DNS. At $\phi = 0$, both the DNS data and RANS solutions show C_f passes into and out of the turbulent region. A laminar patch inserts the turbulent region at around $x = 1.75$. The transition model successfully predicts this undulation form of transition (also see Figure 4.2.24 for $\phi = 0$).

4.3 Rough Wall Cases

4.3.1 Flat Plate Cases

The set up for this case has been described in Section 3.4.2. It is modified from the T3A test case (Roach and Brierley, 1992). The only change of the inflow condition is the turbulence intensity, Tu_{in} . Two values, $Tu_{in} = 1.5\%$ and 3.5% , are specified. Another difference is the wall boundary conditions for k and ω : Equations (3.4.10) and (3.4.8) are used. Grid independence has been checked. The first grid point was refined down to $y^+(1) \approx 0.1$, to show grid independence in the flat plate, rough wall cases. $y^+(1)$ was 1.0 in the smooth wall cases in Ge et al. (2014). This is consistent with the grid requirements for Knopp's model: from grid independence tests, $y^+(1) \lesssim 0.3$ is sufficient for accurate velocity profiles in the fully turbulent region over rough surfaces.

A prerequisite of the current modeling is that the transition location computed by the *smooth wall* transition model should not shift when only the roughness boundary conditions for k and ω are imposed, because the roughness should not affect the laminar boundary layer (at least, for relative low roughness heights). The only influence should be an increase of the C_f values in the fully turbulent region, compared to the smooth wall case.

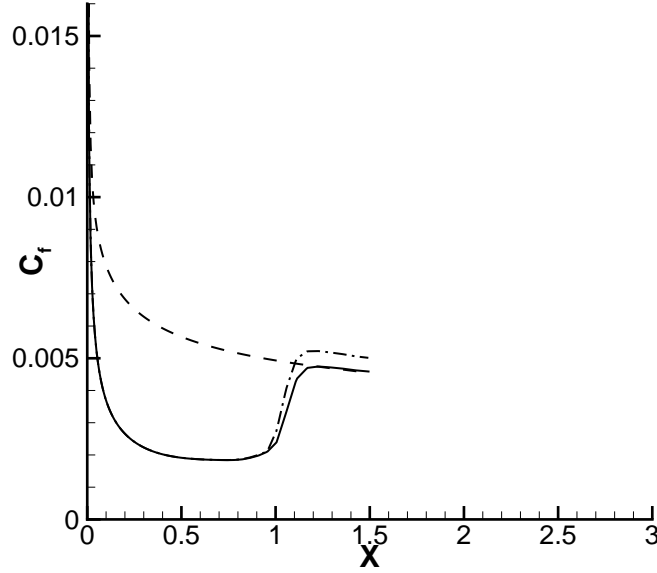


Figure 4.3.1 Contribution of the smooth Leading edge. The smooth wall case (solid), the case with the rough wall boundary conditions and uniform roughness (dash), and the case with the rough wall boundary conditions and a smooth leading edge (dash-dot).

However, this prerequisite cannot be satisfied unless a tiny, smooth leading edge region is specified. The reason is obvious: for an ideal, flat plate, the sharp leading edge leads to infinite skin friction coefficient $C_f \sim 1/\sqrt{x}$ as $x \rightarrow 0$; therefore, r^+ becomes infinite, which is physically unacceptable. If the roughness boundary conditions are imposed at the leading edge, the very large r_+ causes the boundary layer to transition immediately. Numerically, the computation converges to a fully turbulent solution. For a realistic geometry, with a rounded leading edge, with a stagnation point, C_f would be finite.

The need for a smooth leading edge is illustrated in Figure 4.3.1 where $Tu_{in} = 1.5\%$ and

$r = 7 \times 10^{-4}m$ ($r^+ \approx 12$). The solid line represents the solution for the smooth wall case. When boundary conditions (3.4.10) and (3.4.8) for k and ω are imposed on a wall with uniform roughness, the result is the dash line. When a tiny smooth region ($r = 0m$ if $x < 0.01m$) is imposed, the C_f curve is the dash-dot line. The transition location predicted in this case is the same as the smooth wall case, with greater C_f values in the fully turbulent region.

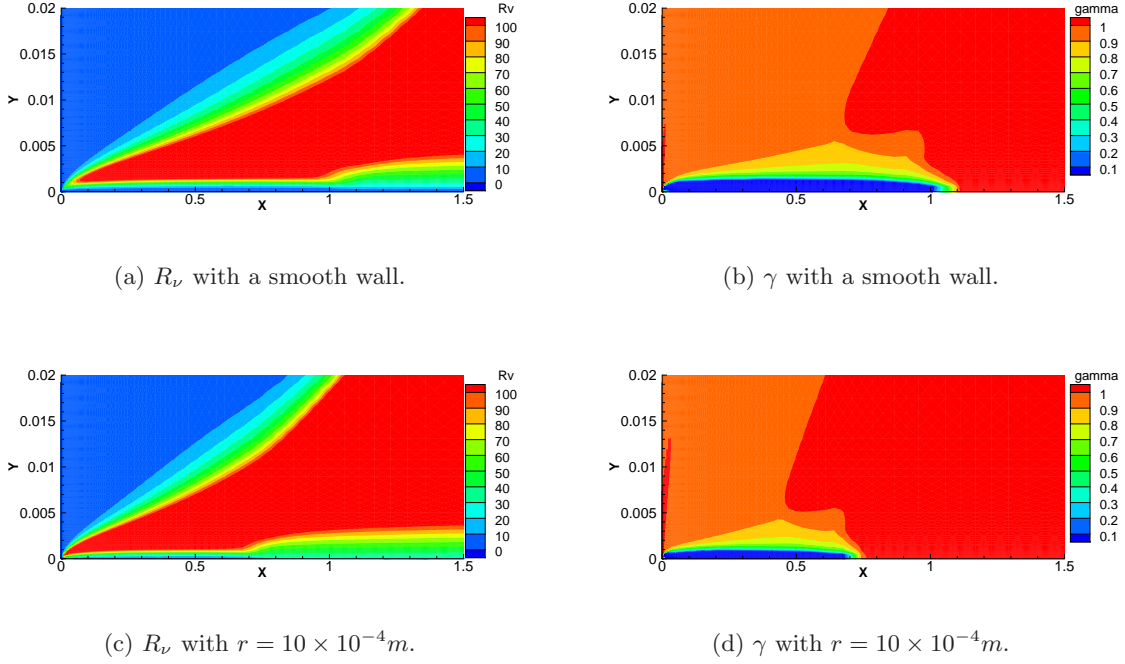


Figure 4.3.2 Near wall distributions of R_ν and γ compared between smooth and rough walls.

With this caveat about the leading edge, the new roughness modification is validated. Contours of R_ν and γ , with and without roughness, are plotted in Figure 4.3.2. Contours of R_ν with a rough wall in Figure 4.3.2(c) show higher values near the wall than those in Figure 4.3.2(a) with a smooth wall, as if there is a displacement of the wall origin upward into the flow field in going from the smooth wall case to the rough wall case. The contours of γ in Figure 4.3.2(b) and 4.3.2(d) depict the laminar region moving upstream, as the roughness increases.

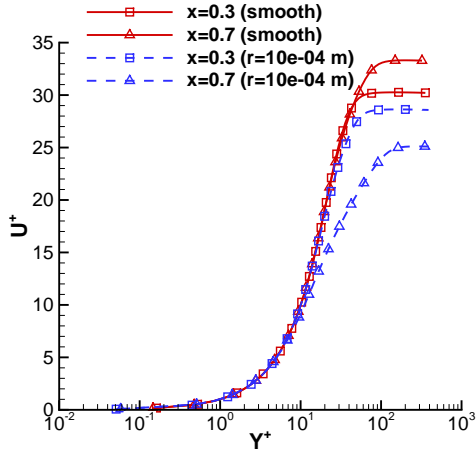
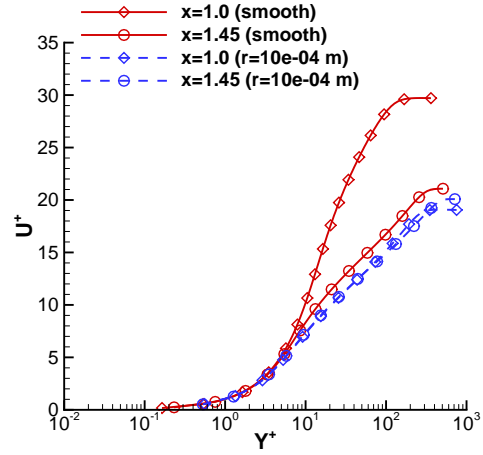
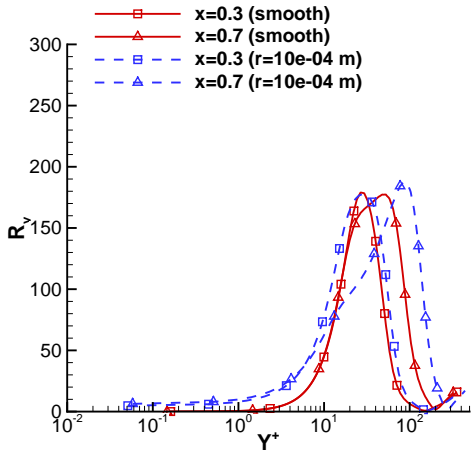
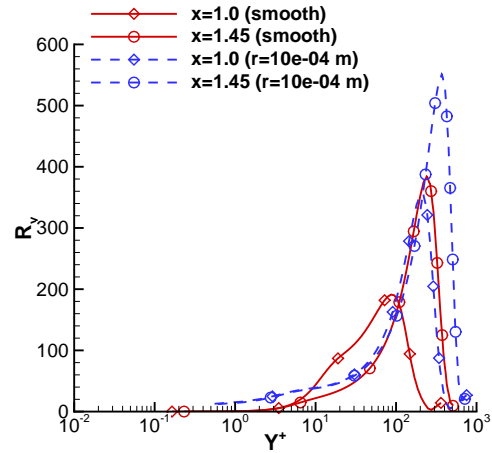
(a) U^+ vs. y^+ at $x=0.3$ and 0.7 .(b) U^+ vs. y^+ at $x=1.0$ and 1.45 .(c) R_ν vs. y^+ at $x=0.3$ and 0.7 .(d) R_ν vs. y^+ at $x=1.0$ and 1.45 .

Figure 4.3.3 Profiles of U^+ and R_ν at $x=0.3, 0.7, 1.0$ and 1.45 . Transition onset is around $x=0.7$ for the rough wall case, and $x=1.0$ for the smooth wall case.

Figure 4.3.3 plots the profiles of $U^+ = U/u_*$ and R_ν for the two cases in Figure 4.3.2. Four different locations are selected – $x=0.3, 0.7, 1.0$ and 1.45 . Transition onset is around $x=0.7$ for the rough wall case, and $x=1.0$ for the smooth wall case. At $x=0.3$, both cases are laminar and their U^+ and R_ν are very close. From around $x=0.7$, the rough wall case starts to transition – the U^+ decreases and the peak location of R_ν with respect to y^+ increases

rapidly, whereas the smooth wall case keeps laminar. At around $x = 1.0$, transition starts to occur for the smooth wall case where the U^+ profiles falls and the peak location of R_ν moves to the right. The rough wall case becomes fully turbulent at this position. Close to the outflow at $x = 1.45$, both the cases are turbulent, while there is a negative offset of U^+ from the smooth to rough case, representing the roughness effects in the fully turbulent boundary layer. It is clearly shown in (c) and (d) that R_ν values close to the wall is non-zero for the rough wall case.

The C_f curves predicted by the current model for several different roughness heights are displayed in Figure 4.3.4. As the roughness increases, the transition location moves upstream toward the leading edge. In the fully turbulent region, the C_f values become larger with higher roughness. For higher turbulence intensity, Figure 4.3.4(b) shows that the transition locations become less sensitive to the roughness height. Similarly, for higher roughness, the transition locations become less sensitive to the free-stream turbulence intensity.

Reasonable agreement is observed between the critical Reynolds number Re_{θ_t} predicted by the model and that calculated from the correlation Equation (2.3.20). Table 4.3.1 contains details for the case with $Tu_{in} = 1.5\%$. For the majority of the roughness heights, the predicted Re_{θ_t} is a little overestimated. For large roughness heights, when $Re_{\theta_t} < 200$, the model tends to predict early transition.

Note that, from the C_f curves, it is very ambiguous which point, exactly, is the transition location. The same question arises for the experimental data. In the present case, the point where the C_f curves start to rise is assumed to be the onset of transition. To calculate the momentum thickness at transition onset, θ_t , the velocity profile is extracted and integrated. This quantity along with local free-stream Tu and C_f may introduce errors in evaluating both the predicted and correlated Re_{θ_t} . In addition, a wide range of critical Reynolds numbers are obtained from cases with various roughness heights, whereas the number of parameters in the present model is relatively few. Thus, very precise prediction of Re_{θ_t} is not expected.

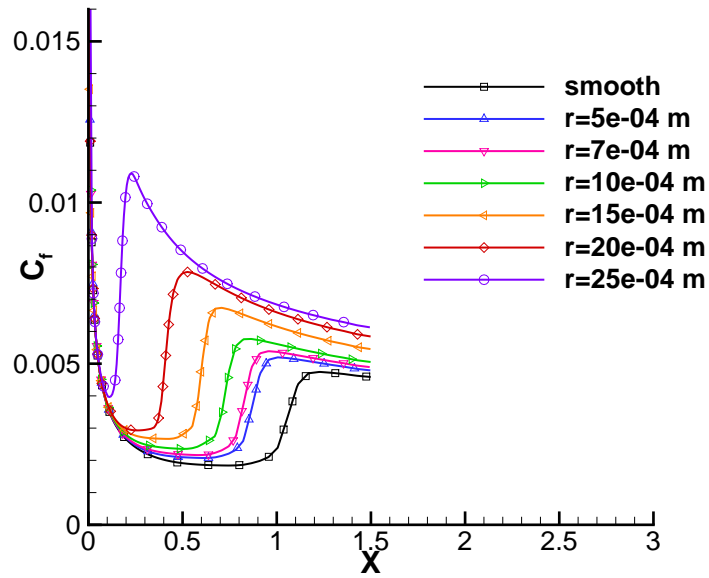
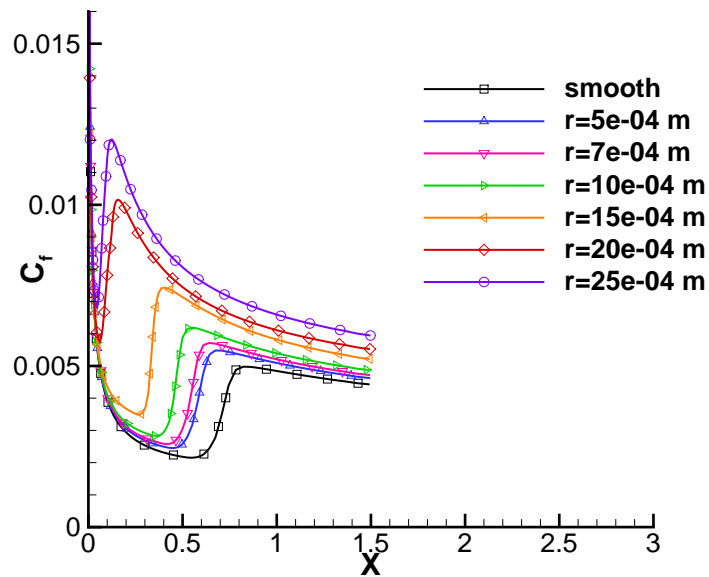
(a) $Tu_{in} = 1.5\%$.(b) $Tu_{in} = 3.5\%$.

Figure 4.3.4 Skin friction for flat plate cases with different roughness heights and different inflow turbulence intensities.

Table 4.3.1 Summary of roughness heights and transition locations (T3A: $Tu_{in} = 1.5\%$).

r ($\times 10^{-4}m$)	5	7	10	15	20	25
r^+	8.5	12.0	17.4	27.2	37.5	48.0
X_t	0.83	0.78	0.67	0.48	0.35	0.11
$Re_{\theta t-pr}$	412	401	372	303	255	132
$Re_{\theta t-cr}$	427	394	346	282	226	173
$Re_{\theta t-smooth}$	442					

The subscript “pr” means predicted, and “cr” means correlated.

4.3.2 A High Pressure Turbine Blade Cascade

In this section, 2-D flow through a passage of a high pressure turbine (HPT) blade cascade is tested with variation of inlet turbulence intensity, Reynold number and roughness height. An experimental database is available in [Stripf et al. \(2005\)](#) and [Stripf \(2007\)](#).

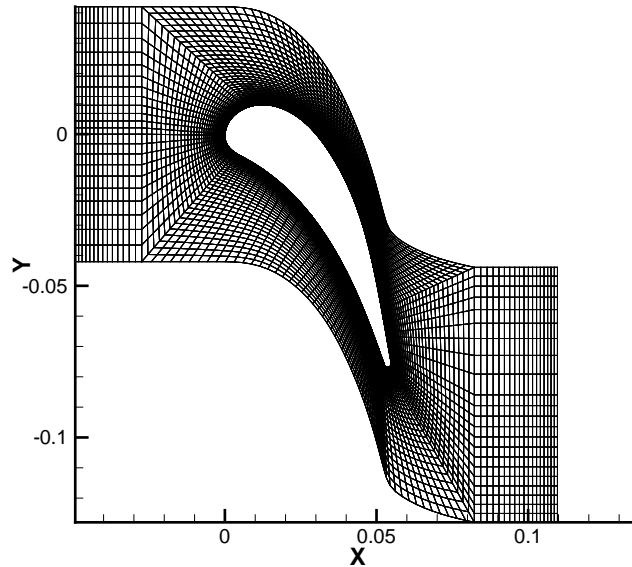


Figure 4.3.5 Mesh used to the HPT blade case showing every other line in tangential and normal wall directions.

Coordinates for the turbine blade geometry are provided by [Stripf \(2007\)](#). The true chord is $93.95mm$ and the axial chord is about $53mm$. The blade pitch is $81.26mm$. Figure 4.3.5 displays the mesh for this case. It is a 3-block grid with an O-grid block as the center part

around the blade and two H-grid blocks as the extended inlet and outlet passages. The flow is incompressible.

Cyclic boundary conditions are imposed on the top and bottom boundaries. The reference pressure is set zero at the outlet and the pressure gradient is zero at the inlet. Table 4.3.2 lists the flow conditions for all test cases. The inlet velocity has only the x -component with the value shown as U_{in} . $Tu_{l.e.}$ and $R_{t-l.e.}$ represent the turbulence intensity and Reynolds number ($k/\omega\nu$) at the mid-pitch of the leading edge location. The kinematic viscosity is $1.5 \times 10^{-5} m^2 s^{-1}$. The inflow Reynolds number based on the true chord Re_c is 2.5×10^5 for TC1-2, and 1.4×10^5 for TC3-4. The number of grid points of the O-grid block is 321×101 for the high Re_c and 161×101 for the low Re_c , in circumferential and wall normal directions respectively. The H-grid blocks have 15×46 and 19×46 grid points in x and y directions at the inlet and outlet for the high Re_c , and 15×23 and 19×23 for the low Re_c . The first grid spacing is set to $y^+(1) \approx 0.5$ for both grids. The pressure coefficient distribution $C_p = (p - p_{static}) / (p_{total} - p_{static})$ on the blade surface for $Re_c = 2.5 \times 10^5$ is displayed in Figure 4.3.6.

To compute the heat transfer to the blade surface, the energy equation is solved along with the continuity and momentum equations. An effective thermal diffusivity $\kappa_{eff} = \nu / Pr + \nu_T / Pr_T$ is used to represent heat transport. The laminar and turbulent Prandtl numbers, Pr and Pr_T , are 0.72 and 0.86, respectively. The air density is $1.2 kg/m^3$ and the heat capacity c_p is $1000 m^2 / (s^2 K)$. A constant surface temperature, $300^\circ K$, is specified, and the ambient temperature is $400^\circ K$.

Table 4.3.2 Summary of inlet conditions for the Stripf's HPT blade case.

Case	$U_{in}(m/s)$	$Tu_{l.e.}(\%)$	$R_{t-l.e.}$	$\nu(\times 10^{-5} m^2 s^{-1})$
TC1	39.915	2.4	12.0	1.5
TC2	39.915	1.6	5.5	1.5
TC3	22.352	4.3	21.6	1.5
TC4	22.352	2.7	8.4	1.5

The computed results are plotted in Figure 4.3.7 and 4.3.8. The Nusselt numbers predicted by the current model on the suction surface are compared with the predicted heat transfer coefficient by Boyle's correlation-based model. Reasonable agreement is achieved, in term of

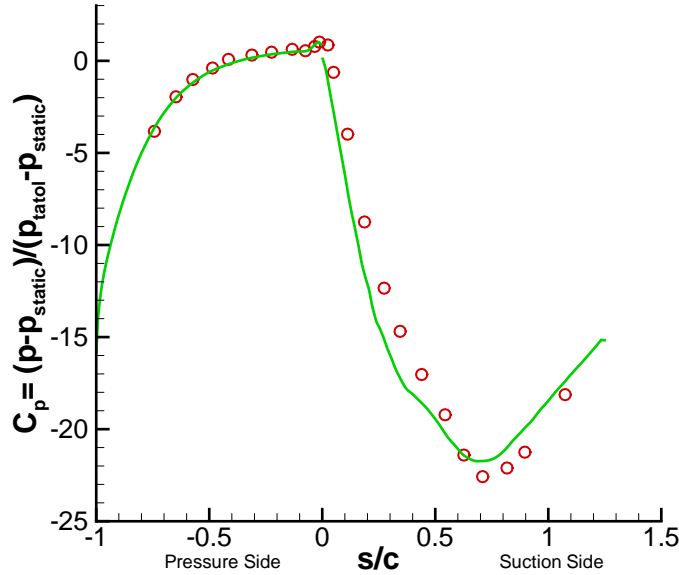


Figure 4.3.6 Pressure distribution on the blade surface for $Re_c = 2.5 \times 10^5$. The circles represent the experimental data of Stripf (2007) at the mid-span of the blade surface. The solid line represents the simulation result.

the shape of the curves, and more importantly the transition location. As the roughness height increases, the transition location moves upstream, to the leading edge.

Comparison between Figures 4.3.7(a) and (b) shows that for relative high roughness, the transition onset becomes less sensitive to the free-stream Tu . This observation agrees with the experimental database. Similarly, high Tu leads to less sensitivity to the roughness height. In addition, one sees that the transition location on the rough wall is more sensitive to the chord Reynolds number than that on the smooth wall. This is shown by comparing 4.3.7(a) and (c), or 4.3.7(b) and (d).

There is some uncertainty about the free-stream turbulence in these experiments. The inflow k and ω were adjusted for the current simulations so that the solid and dashed, red curves provide similar transition locations in the smooth wall case. The experimental data suggest a much quicker decay than the $k - \omega$ model does, even if a very high dissipation rate, ω , is specified to the free-stream. Therefore, our method to determine the inlet k and ω is to make the transition location the same as the experimental data for the smooth wall case.

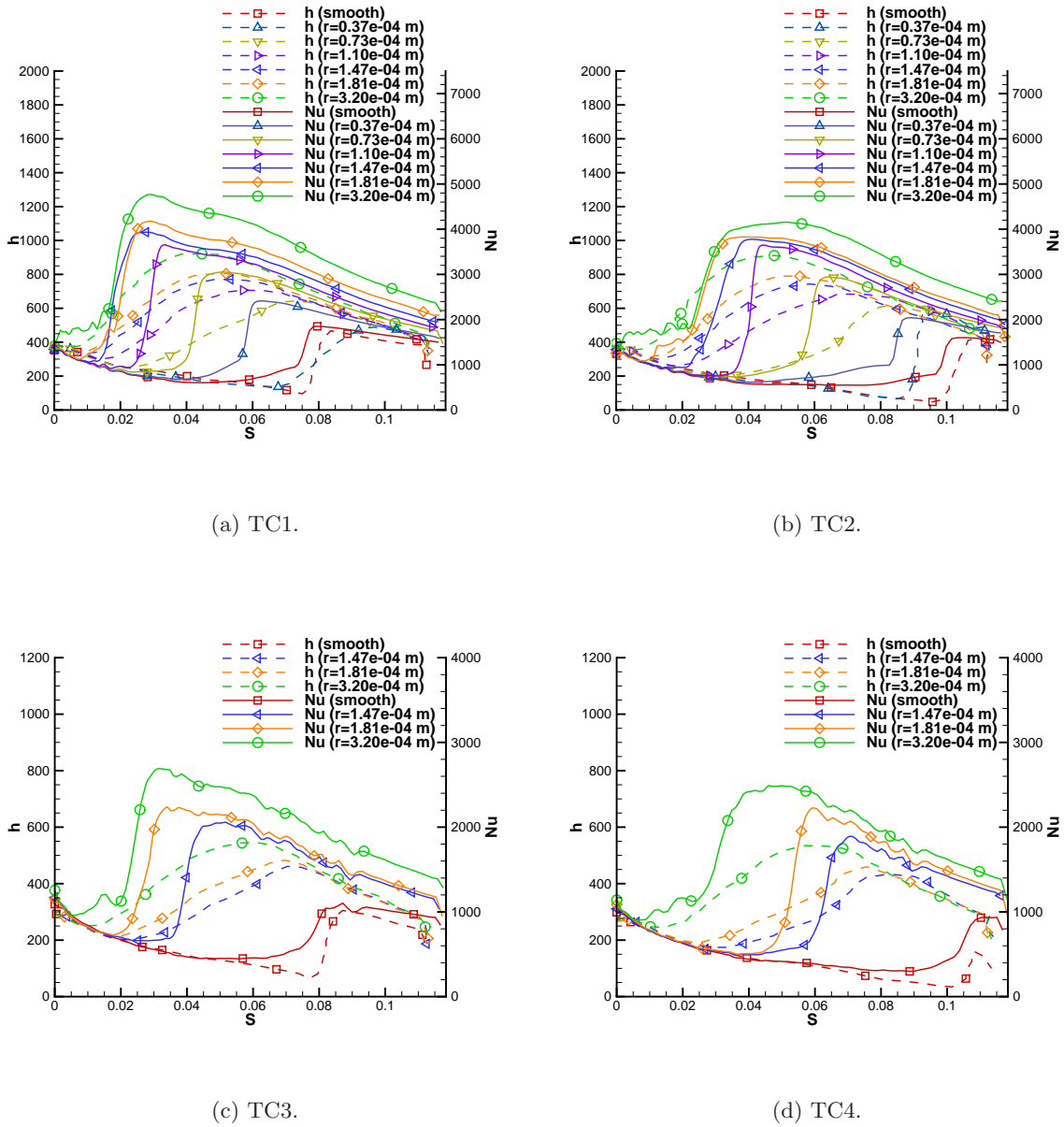


Figure 4.3.7 Results for the Strip's HPT blade case. The solid lines are the predicted curves for the Nusselt number by the current model, and the dash lines are the predicted curves for the heat transfer coefficient by the correlation-based model in Boyle and Stripf (2009).

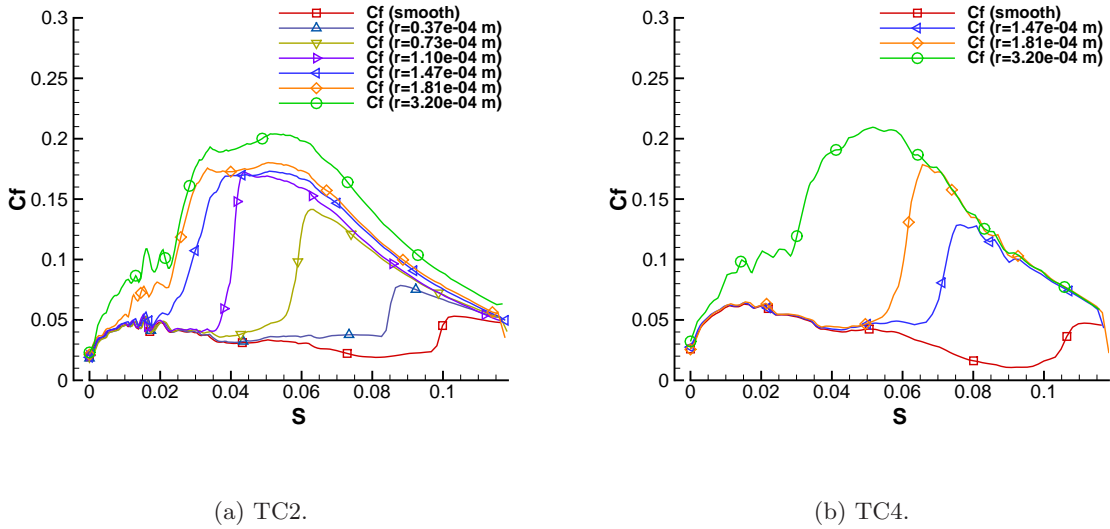


Figure 4.3.8 Skin friction coefficient for the Stripf's HPT blade: Case TC2 and TC4.

In the fully turbulent region, it is reasonable that the heat transfer rate becomes higher as the roughness increases. However in the experimental data, heat transfer is not very sensitive to the roughness height. However, the C_f curves appears less sensitive to various roughness heights in the fully turbulent region, especially for case TC4. See Figure 4.3.8(b). The dimensionless roughness r^+ is evaluated from C_f close to the trailing edge and listed in Tables 4.3.3 and 4.3.4. Only the highest roughness reaches the fully rough condition ($r^+ > 90$). Most of the cases are transitionally rough, which should cause sensitivity to the roughness geometry in the fully turbulent region. In the experiment, the boundary layer may have not developed into a fully turbulent condition, even after transition.

Table 4.3.3 Summary of roughness heights for the Stripf's HPT blade, TC2.

r ($\times 10^{-4}m$)	0.37	0.73	1.10	1.47	1.81	3.20
r^+	16.1	32.0	47.7	65.3	82.0	153.3

Table 4.3.4 Summary of roughness heights for the Stripf's HPT blade, TC4.

r ($\times 10^{-4}m$)	1.47	1.81	3.20
r^+	40.0	49.3	90.0

4.3.3 A Low Pressure Turbine Blade Cascade

The database provided by [Stripf \(2007\)](#) also contains a low pressure turbine (LPT) blade cascade. This may serve as a good supplementary validation of the roughness model. [Stripf et al. \(2009b\)](#) and [Boyle and Stripf \(2009\)](#) use this case to validate their correlation-based model. In addition to the effect of roughness height, some other factors, such as roughness density, and locally varying roughness are investigated for this case in their papers. Since the current model considers only the effective sand grain roughness height r , the influence of various r evaluated by [Boyle and Stripf \(2009\)](#) for different rough surfaces are examined in this section along with two different free-stream Tu . The predicted results are compared with the measured data given in [Stripf et al. \(2009b\)](#).

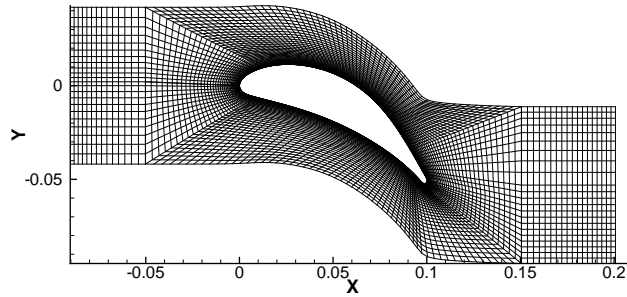


Figure 4.3.9 Mesh used to the LPT blade case showing every other line in tangential and normal wall directions.

The geometry is again obtained from [Stripf \(2007\)](#). The true chord is 113.34mm and the axial chord is about 100mm . The blade pitch is 83.4mm . The same approach as the HPT case is used to generate the LPT mesh; see [Figure 4.3.9](#). The size of the O-grid block is 321×101 with $y^+(1) \approx 0.3$. The H-grid blocks have 15×46 and 19×46 grid points at the inlet and outlet. Similar boundary conditions are employed as the HPT case. The flow parameters are shown in [Table 4.3.5](#). The true chord Reynolds number Re_c is 2.5×10^5 . Parameters for the energy equation are all the same as the previous case.

The computed results are depicted in [Figure 4.3.10](#) and [4.3.11](#). Decent agreement is observed between the Nusselt number distribution predicted by the current model and measured in the experiment on the suction surface. The effect of the roughness height is shown clearly. The

Table 4.3.5 Summary of inlet conditions for the Stripf's LPT blade case.

Case	$U_{in}(m/s)$	$Tu_{l.e.}(\%)$	$R_{t-l.e.}$	$\nu(\times 10^{-5}m^2s^{-1})$
TC5	33.086	3.1	30.0	1.5
TC6	33.086	2.7	22.3	1.5

inflow conditions for k and ω for this case are again chosen based on the criterion that computed results of the smooth wall cases should match the experimental data. By comparing the results with two different Tu , one can infer that the transition location becomes less sensitive to Tu as the roughness becomes higher, which is both presented by the experimental data and by the current model. These observations are consistent with the HPT blade case. Both Nu and C_f in fully turbulent region show very slight sensitivity to various roughness heights for LPT cases. Various r^+ for TC6 are given in Table 4.3.6, which are smaller than those in the HPT case with comparable values of r , due to lower skin friction.

Table 4.3.6 Summary of roughness heights for the Stripf's LPT blade, TC6.

$r(\times 10^{-4}m)$	1.21	2.23	3.95
r^+	14.0	22.7	36.2

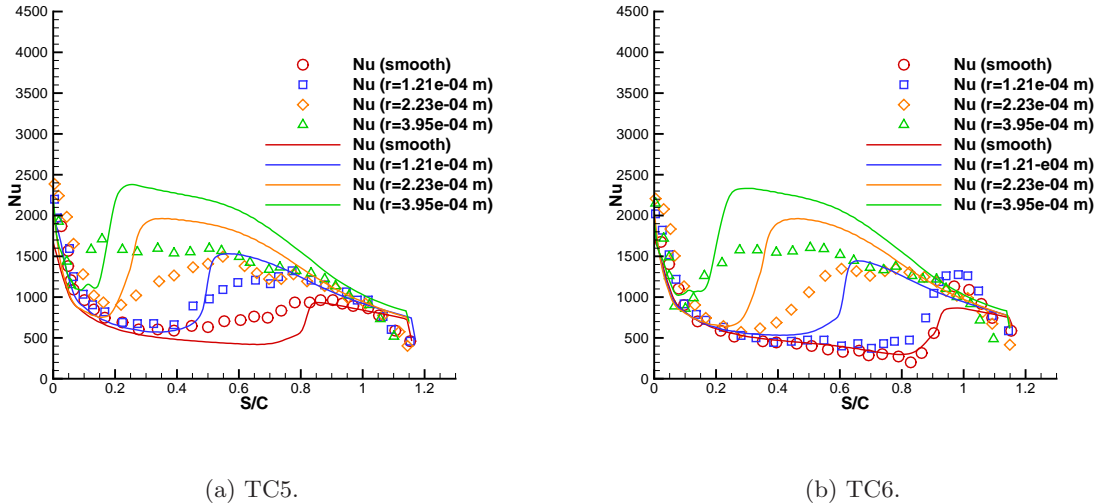


Figure 4.3.10 Nusselt number for the Stripf's LPT blade case. The solid lines are the predicted curves for the Nusselt number by the current model, and the symbols present the experimental data.

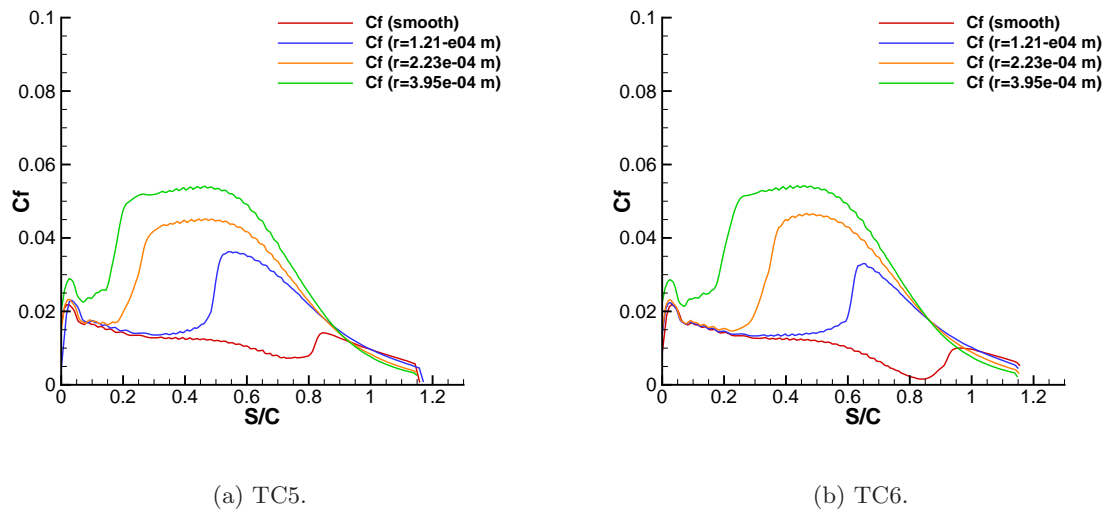


Figure 4.3.11 Skin friction coefficient for the Stripf's LPT blade: Case TC5 and TC6.

CHAPTER 5. SUMMARY

5.1 Conclusion

The present work has proposed an intermittency bypass transition model that is simpler than those published and without data correlation. Although it remains quite empirical, the number of parameters is fewer and the role of each more apparent. It depends on only local variables and hence is suitable for general computational fluid dynamics applications. One single intermittency transport equation is developed and coupled with the $k - \omega$ RANS model. Transition is initiated by diffusion and a source term carries it to turbulence. A sink term is applied to ensure a laminar boundary layer before transition and it vanishes in the turbulent region. Moreover, the model does not depend directly on pressure gradient and is capable of predicting separation-induced transition and reattachment in a strong adverse pressure gradient region.

Based on the concept of the *equivalent sand grain roughness* and effective *displacement of the origin*, this intermittency model is extended to predict roughness effects on transition. The local Reynolds number is modified by adding an effective displacement to the wall distance. Some other modifications are needed for practical cases, like a turbine blade cascade. Boundary conditions for the fully turbulent region of the boundary layer on rough walls are imposed. The performance of this proposed model for prediction of roughness effects depends on the performance of the model for smooth wall cases. The key point is that the roughness modification is capable of properly shifting the smooth wall results for boundary layer transition.

A range of test cases were computed to validate the model for smooth walls, under different free-stream Reynolds numbers, turbulence intensities, pressure gradients, and periodic passing turbulent wakes. The numerical results showed decent agreement with the experimental or

DNS data.

The rough wall model was validated by flat plate and turbine blade cases, with variations of roughness height, Reynolds number, free-stream turbulence intensity and pressure gradient. Reasonable agreement, especially in terms of transition location, with the results of a data correlation-based model, or with experimental data, was obtained.

5.2 Suggestions for Future Work

One limitation of the current model is the inapplicability to cases with low free-stream turbulence intensity ($Tu < 1\%$). Because of the nature of the model, it is mainly proposed to simulate bypass transition. The model is not suitable for cases with transition by linear instability waves, for instance the T3A- case. Durbin (2012) provided a measure to suppress the source term for case T3A- to delay its transition. However this does not work well in the proposed model for general CFD codes and the predicted transition would be too early. Some modification remains to be done to extend the scope of this model to low Tu cases.

The roughness model proposed cannot predict the prolonged transition lengths seen from the data. The long transition region is presumably due to the separated roughness elements in the experiments. Future efforts may be spent on this issue. In addition, Roughness effects on transition in separated flows are not in the scope of the current work; they remain to be explored in the future.

APPENDIX. FULL MODEL FORMULATION

1 Model for Smooth Walls

The intermittency transport equation is as follows,

$$\frac{D\gamma}{Dt} = \partial_j \left[\left(\frac{\nu}{\sigma_l} + \frac{\nu_T}{\sigma_\gamma} \right) \partial_j \gamma \right] + P_\gamma - E_\gamma, \quad (1)$$

$$P_\gamma = F_\gamma |\Omega| (\gamma_{max} - \gamma) \sqrt{\gamma}, \quad (2)$$

$$E_\gamma = G_\gamma F_{turb} |\Omega| \gamma^{1.5}, \quad (3)$$

where $\sigma_l = 5.0$, $\sigma_\gamma = 0.2$ and $\gamma_{max} = 1.1$. The model depends on the parameters

$$\begin{cases} R_t \equiv \frac{\nu_T}{\nu}, \\ T_\omega \equiv R_t \frac{|\Omega|}{\omega}, \\ R_\nu \equiv \frac{d^2 |\Omega|}{2.188 \nu}. \end{cases} \quad (4)$$

Here $|\Omega|$ is defined by $\sqrt{2\Omega_{ij}\Omega_{ij}}$. The source term contains

$$F_\gamma = 2 \max [0, \min (100 - 0.7R_\nu, 1)] \times \min [\max (R_\nu - R_{c1}, 0), 4]. \quad (5)$$

$$R_{c1} = 400 - 360 \min \left(\frac{T_\omega}{2}, 1 \right). \quad (6)$$

The sink term contains

$$G_\gamma = 7.5 \max [0, \min (100 - R_\nu, 1)] \times \min [\max (R_\nu - 18, 0), 1]. \quad (7)$$

$$F_{turb} = e^{-(R_\nu R_t)^{1.2}}. \quad (8)$$

The separation modification is applied via γ_{eff} . It depends on adverse pressure gradient detector,

$$R_s \equiv d \cdot \frac{\mathbf{n}_w \cdot \nabla |S| \omega}{\sqrt{2} |S|^2}. \quad (9)$$

Here $|S|$ is defined by $\sqrt{S_{ij} S_{ji}}$.

$$\gamma_{eff} = \max [\min (1, \gamma), \min (2, F_{R_t} F_{R_\nu} F_{R_s})]. \quad (10)$$

The limiter $\min (1, \gamma)$ clips off values greater than one for the γ field solved by the γ transport equation. The 3 functions are defined as follows,

$$F_{R_t} = e^{-(R_t/10)^3}, \quad (11)$$

$$F_{R_\nu} = \max (R_\nu - 200, 0), \quad (12)$$

$$\begin{aligned} F_{R_s} &= \min [1.0, \max (10 + 5R_s, 0)] \\ &\times \min [1.0, \max (10 - 5R_s, 0)]. \end{aligned} \quad (13)$$

The current formulation is applied to the $k - \omega$ RANS closure. The production term of the k equation is multiplied by γ_{eff} . This is the only appearance of γ within the turbulence model.

$$\frac{Dk}{Dt} = P_k - C_\mu k \omega + \partial_j \left[\left(\nu + \frac{\nu_T}{\sigma_k} \right) \partial_j k \right], \quad (14)$$

$$P_k = \min \left(2\nu_T |S|^2, k |S| / \sqrt{3} \right) \gamma_{eff}, \quad (15)$$

$$\frac{D\omega}{Dt} = 2C_{\omega 1} |S|^2 - C_{\omega 2} \omega^2 + \partial_j \left[\left(\nu + \frac{\nu_T}{\sigma_\omega} \right) \partial_j \omega \right], \quad (16)$$

where $C_\mu = 0.09$, $C_{\omega 1} = 5/9$, $C_{\omega 2} = 3/40$ and $\sigma_\omega = \sigma_k = 2$. The eddy viscosity ν_T is k/ω .

2 Model for Rough Walls

An effective origin for the wall distance is applied to the model for smooth walls.

$$R_\nu \equiv \frac{(d + 0.26r)^2 |\Omega|}{2.188\nu}. \quad (17)$$

$$R_s \equiv (d + 0.26r) \cdot \frac{\mathbf{n}_w \cdot \nabla |S| \omega}{\sqrt{2} |S|^2}. \quad (18)$$

Accordingly, the sink term has to be modified due to the change of R_ν .

$$G_\gamma = 7.5 \max [0, \min ((100 + R_{c3}) - R_\nu, 1)] \quad (19)$$

$$\times \min [\max (R_\nu - (18 + R_{c2}), 0), 1].$$

$$R_{c2} = 3.0 \left[\frac{(0.26r)^2 |\Omega|}{2.188\nu} \right]^{0.8}. \quad (20)$$

$$R_{c3} = 0.3 \frac{(d + 0.26r)^2 \sqrt{|Q|} \text{sign}(Q)}{\nu}, R_{c3} = \max [\min (R_{c3}, 100), -100], \quad (21)$$

where $Q = \Omega_{ij}\Omega_{ij} - S_{ij}S_{ij}$.

$$F_{turb} = e^{-(R_{\nu_{new}} R_t)^{1.2}}. \quad (22)$$

$$R_{\nu_{new}} = R_\nu e^{-F_Q^{1.5}/350}. \quad (23)$$

$$F_Q = \max \left[0, \frac{r^2 \sqrt{|Q|} \text{sign}(Q)}{\nu} \right]. \quad (24)$$

R_{c3} and $R_{\nu_{new}}$ are used for strong favorable pressure gradient cases, such as a region right after the leading edge on a suction surface of a turbine blade.

BIBLIOGRAPHY

- Abu-Ghannam, B. J. and Shaw, R. (1980). Natural transition of boundary layers—the effects of turbulence, pressure gradient, and flow history. *Journal of Mechanical Engineering Science*, 22(5):213–228.
- Arts, T. (1995). Thermal investigation of a highly loaded transonic turbine film cooled guide vane. *VDI BERICHTE*, 1186:273–273.
- Arts, T., Lamvert de Rouvroit, M., and Rutherford, A. W. (1990). Aero-thermal investigation of a highly loaded transonic linear turbine guide vane cascade. *VKI Technical Note*, 174.
- Boiko, A. V., Westin, K. J. A., Klingmann, B. G. B., Kozlov, V. V., and Alfredsson, P. H. (1994). Experiments in a boundary layer subjected to free stream turbulence. Part 2. the role of ts-waves in the transition process. *Journal of Fluid Mechanics*, 281:219–245.
- Bons, J. P. (2010). A review of surface roughness effects in gas turbines. *Journal of turbomachinery*, 132(2):021004.
- Boyle, R. J. and Senyitko, R. G. (2003). Measurements and predictions of surface roughness effects on turbine vane aerodynamics. *ASME Paper*, GT-2003-38580.
- Boyle, R. J. and Stripf, M. (2009). Simplified approach to predicting rough surface transition. *Journal of Turbomachinery*, 131:041020.
- Cossu, C. and Brandt, L. (2004). On Tollmien–Schlichting-like waves in streaky boundary layers. *European Journal of Mechanics-B/Fluids*, 23(6):815–833.
- Dassler, P., Kožulović, D., and Fiala, A. (2010). Modelling of roughness-induced transition using local variables. In *V European Conference on CFD, ECCOMAS CFD*.

- Dhawan, S. j. and Narasimha, R. (1958). Some properties of boundary layer during the transition from laminar to turbulent flow motion. *Journal of Fluid Mechanics*, 3:418–436.
- Durbin, P. A. (2009). Limiters and wall treatments in applied turbulence modeling. *Fluid Dynamics Research*, 41(1):012203 (18pp).
- Durbin, P. A. (2012). An intermittency model for bypass transition. *International Journal of Heat and Fluid Flow*, 36(0):1–6.
- Durbin, P. A., Jacobs, R. G., and Wu, X. (2002). DNS of bypass transition. *Closure Strategies for Turbulent and Transitional Flows*, pages 449–463.
- Durbin, P. A., Medic, G., Seo, J.-M., Eaton, J. K., and Song, S. (2001). Rough wall modification of two-layer $k - \varepsilon$. *Journal of Fluids Engineering*, 123:16–21.
- Durbin, P. A. and Reif, B. P. (2011). *Statistical Theory and Modeling for Turbulent Flows (Second Edition)*. John Wiley & Sons.
- Durbin, P. A. and Wu, X. (2007). Transition beneath vortical disturbances. *Annual Review of Fluid Mechanics*, 39(1):107–128.
- Elsner, W. and Warzecha, P. (2014). Numerical study of transitional rough wall boundary layer. *Journal of Turbomachinery*, 136:011010.
- Fransson, J. H., Brandt, L., Talamelli, A., and Cossu, C. (2005). Experimental study of the stabilization of Tollmien–Schlichting waves by finite amplitude streaks. *Physics of Fluids (1994-present)*, 17(5):054110.
- Ge, X., Arolla, S. K., and Durbin, P. A. (2014). A bypass transition model based on the intermittency function. *Flow, Turbulence and Combustion*, 93(1):37–61.
- Ge, X. and Durbin, P. A. (2015). An intermittency model for predicting roughness induced transition. *International Journal of Heat and Fluid Flow*, 54:55–64.

- Gostelow, J. P., Blunden, A. R., and Walker, G. J. (1994). Effects of free-stream turbulence and adverse pressure gradients on boundary layer transition. *Journal of turbomachinery*, 116(3):392–404.
- Herbert, T. (1983). Secondary instability of plane channel flow to subharmonic three-dimensional disturbances. *Physics of Fluids (1958-1988)*, 26(4):871–874.
- Jacobs, R. G. and Durbin, P. A. (2001). Simulations of bypass transition. *Journal of Fluid Mechanics*, 428:185–212.
- Kendall, J. M. (1985). Experimental study of disturbances produced in a pre-transitional laminar boundary layer by weak freestream turbulence. In *AIAA, 18th Fluid Dynamics and Plasmadynamics and Lasers Conference*, volume 1.
- Kendall, J. M. (1991). Studies on laminar boundary-layer receptivity to freestream turbulence near a leading edge. In *Boundary layer stability and transition to turbulence*, volume 1, pages 23–30.
- Klebanoff, P. S., Tidstrom, K. D., and Sargent, L. M. (1962). The three-dimensional nature of boundary-layer instability. *Journal of Fluid Mechanics*, 12(01):1–34.
- Kleiser, L. and Zang, T. A. (1991). Numerical simulation of transition in wall-bounded shear flows. *Annual Review of Fluid Mechanics*, 23(1):495–537.
- Knopp, T., Eisfeld, B., and Calvo, J. B. (2009). A new extension for $k - \omega$ turbulence models to account for wall roughness. *International Journal of Heat and Fluid Flow*, 30(1):54–65.
- Koch, C. C. and Smith, L. H. (1976). Loss sources and magnitudes in axial-flow compressors. *ASME J. Eng. Power*, 98:411–424.
- Langtry, R. B. (2006). *A Correlation-Based Transition Model using Local Variables for Unstructured Parallelized CFD Codes*. PhD thesis, Universitt Stuttgart, Holzgartenstr. 16, 70174 Stuttgart.
- Langtry, R. B. and Menter, F. R. (2009). Correlation-based transition modelling for unstructured parallelized computational fluid dynamics codes. *AIAA Journal*, 47(12):2894–2906.

- Lardeau, S., Fadai-Ghotbi, A., and Leschziner, M. (2009). Modelling bypass and separation-induced transition by reference to pre-transitional fluctuation energy. *ERCFTAC Bull. Transition Modelling*, 80:72–76.
- Lardeau, S., Leschziner, M., and Zaki, T. A. (2012). Large eddy simulation of transitional separated flow over a flat plate and a compressor blade. *Flow, Turbulence and Combustion*, 88(1-2):19–44.
- Lardeau, S., Leschziner, M. A., and Li, N. (2004). Modelling bypass transition with low-reynolds-number nonlinear eddy-viscosity closure. *Flow, Turbulence and Combustion*, 73(1):49–76.
- Licari, A. and Christensen, K. (2011). Modeling cumulative surface damage and assessing its impact on wall turbulence. *AIAA journal*, 49(10):2305–2320.
- Ligrani, P. M. and Moffat, R. J. (1986). Structure of transitionally rough and fully rough turbulent boundary layers. *Journal of Fluid Mechanics*, 162:69–98.
- Liu, X. and Rodi, W. (1991). Experiments on transitional boundary layers with wake-induced unsteadiness. *Journal of Fluid Mechanics*, 231:229–256.
- Liu, Y., Zaki, T. A., and Durbin, P. A. (2008). Boundary-layer transition by interaction of discrete and continuous modes. *Journal of Fluid Mechanics*, 604:199.
- Lorenz, M., Schulz, A., and Bauer, H.-J. (2013). Predicting rough wall heat transfer and skin friction in transitional boundary layers a new correlation for bypass transition onset. *Journal of Turbomachinery*, 135(4):041021.
- Lou, W. and Hourmouziadis, J. (2000). Separation bubbles under steady and periodic-unsteady main flow conditions. *Journal of Turbomachinery*, 122:634–643.
- Malkiel, E. and Mayle, R. E. (1996). Transition in a separation bubble. *Journal of turbomachinery*, 118(4):752–759.
- Mayle, R. E. (1991). The 1991 igt scholar lecture: The role of laminar-turbulent transition in gas turbine engines. *Journal of Turbomachinery*, 113(4):509–536.

- Mayle, R. E. and Schulz, A. (1997). Heat transfer committee and turbomachinery committee best paper of 1996 award: The path to predicting bypass transition. *Journal of Turbomachinery*, 119(3):405–411.
- Menter, F. R., Langtry, R. B., Likki, S. R., Suzen, Y. B., Huang, P. G., and Völker, S. (2006a). A correlation-based transition model using local variables – Part I: model formulation. *Journal of turbomachinery*, 128(3):413–422.
- Menter, F. R., Langtry, R. B., and Völker, S. (2006b). Transition modelling for general purpose CFD codes. *Flow, Turbulence and Combustion*, 77(1-4):277–303.
- Praisner, T. J. and Clark, J. P. (2007). Predicting transition in turbomachinery – Part I: A review and new model development. *Journal of Turbomachinery*, 129:1–13.
- Rao, V. N., Jefferson-Loveday, R., Tucker, P. G., and Lardeau, S. (2014). Large eddy simulations in turbines: influence of roughness and free-stream turbulence. *Flow, Turbulence and Combustion*, 92(1-2):543–561.
- Roach, P. E. and Brierley, D. H. (1992). The influence of a turbulent free-stream on zero pressure gradient transitional boundary layer development Part 1: Test cases T3A and T3B. In *Numerical Simulation of Unsteady Flows and Transition to Turbulence*, pages 319–347. ERCOFTAC.
- Schlichting, H. (1979). *Boundary Layer Theory*. McGraw-Hill, New York.
- Schubauer, G. B. and Skramstad, H. K. (1947). Laminar-boundary-layer oscillations and transition on a flat plate. *Journal of National Bureau of Standards*, 38:251–292.
- Seo, J.-M. (2004). *Closure Modeling and Numerical Simulation for Turbulent Flows: Wall Roughness Model, Realizability, and Turbine Blade Heat Transfer*. PhD thesis, Flow Physics and Computation Division, Dept. of Mechanical Engineering, Stanford University.
- Solomon, W. J., Walker, G. J., and Gostelow, J. P. (1996). Transition length prediction for flows with rapidly changing pressure gradients. *Journal of turbomachinery*, 118(4):744–751.

- Steelant, J. and Dick, E. (1996). Modelling of bypass transition with conditioned navierstokes equations coupled to an intermittency transport equation. *International Journal for Numerical Methods in Fluids*, 23(3):193–220.
- Stripf, M. (2007). Einfluss der oberflächenrauigkeit auf die transitionale grenzschicht an gasturbinenschaufeln. *Forschungsberichte aus dem Institut für Thermische Strömungsmaschinen*, 38.
- Stripf, M., Schulz, A., Bauer, H.-J., and Wittig, S. (2009a). Extended models for transitional rough wall boundary layers with heat transfer – Part I: Model formulations. *Journal of Turbomachinery*, 131:031016.
- Stripf, M., Schulz, A., Bauer, H.-J., and Wittig, S. (2009b). Extended models for transitional rough wall boundary layers with heat transfer – Part II: Model validation and benchmarking. *Journal of Turbomachinery*, 131:031017.
- Stripf, M., Schulz, A., and Wittig, S. (2005). Surface roughness effects on external heat transfer of a hp turbine vane. *Journal of Turbomachinery*, 127:200–208.
- Suluksna, K., Dechaumphai, P., and Juntasaro, E. (2009). Correlations for modeling transitional boundary layers under influences of freestream turbulence and pressure gradient. *International Journal of Heat and Fluid Flow*, 30(1):66–75.
- Suzen, Y. B. and Huang, P. G. (2000). Modeling of flow transition using an intermittency transport equation. *Journal of Fluids Engineering*, 122(2):273–284.
- Suzen, Y. B., Huang, P. G., Hultgren, L. S., and Ashpis, D. E. (2003). Predictions of separated and transitional boundary layers under low-pressure turbine airfoil conditions using an intermittency transport equation. *Journal of Turbomachinery*, 125(3):455–464.
- Suzen, Y. B., Xiong, G., and Huang, P. G. (2000). Predictions of transitional flows in low-pressure turbines using an intermittency transport equation. In *AIAA paper, Fluids 2000 Conference, Denver, Colorado, June 19-22*, volume AIAA-2000-2654.

- Volino, R. J. and Hultgren, L. S. (2001). Measurements in separated and transitional boundary layers under low-pressure turbine airfoil conditions. *Journal of Turbomachinery*, 123(2):189–197.
- Walters, D. K. and Cokljat, D. (2008). A three-equation eddy-viscosity model for reynolds-averaged navier–stokes simulations of transitional flow. *Journal of Fluids Engineering*, 130(12):121401.
- Wilcox, D. C. (1993). *Turbulence Modelling for CFD*. DCW industries.
- Wilcox, D. C. (1998). *Turbulence Modeling for CFD (Second Edition)*. DCW Industries.
- Wissink, J. G. and Rodi, W. (2006a). Direct numerical simulation of flow and heat transfer in a turbine cascade with incoming wakes. *Journal of Fluid Mechanics*, 569:209–247.
- Wissink, J. G. and Rodi, W. (2006b). Direct numerical simulations of transitional flow in turbomachinery. *Journal of Turbomachinery*, 128:668.
- Wissink, J. G., Zaki, T. A., Rodi, W., and Durbin, P. A. (2014). The effect of wake turbulence intensity on transition in a compressor cascade. *Flow, Turbulence and Combustion*, 93(4):555–576.
- Wu, X. and Durbin, P. A. (2000). Boundary layer transition induced by periodic wakes. *Journal of turbomachinery*, 122(3):442–449.
- Wu, X., Jacobs, R. G., Hunt, J. C., and Durbin, P. A. (1999). Simulation of boundary layer transition induced by periodically passing wakes. *Journal of Fluid Mechanics*, 398:109–153.
- Zaki, T. A. and Durbin, P. A. (2005). Mode interaction and the bypass route to transition. *Journal of Fluid Mechanics*, 531:85–111.
- Zaki, T. A. and Durbin, P. A. (2006). Continuous mode transition and the effects of pressure gradient. *Journal of Fluid Mechanics*, 563:357–388.

Zaki, T. A., Wissink, J. G., Durbin, P. A., and Rodi, W. (2009). Direct computations of boundary layers distorted by migrating wakes in a linear compressor cascade. *Flow, turbulence and combustion*, 83(3):307–322.

Zaki, T. A., Wissink, J. G., Rodi, W., and Durbin, P. A. (2010). Direct numerical simulations of transition in a compressor cascade: the influence of free-stream turbulence. *Journal of Fluid Mechanics*, 665:57–98.

Zhang, X. F. (2006). *Separation and transition control on ultra-high-lift low pressure turbine blades in unsteady flow*. PhD thesis, University of Cambridge.